

---

# High repetition rate laser driven proton source and a new method of enhancing acceleration

Ying Gao

---



München 2020



---

# High repetition rate laser driven proton source and a new method of enhancing acceleration

Ying Gao

---

Dissertation  
an der Fakultät für Physik  
der Ludwig-Maximilians-Universität  
München

vorgelegt von  
Ying Gao  
aus Shandong, China

München, den 6. Mai 2020

Erstgutachter: Prof. Dr. Jörg Schreiber  
Zweitgutachter: Prof. Dr. Matthias Kling  
Tag der mündlichen Prüfung: 02. Juli 2020

# Contents

<b>Abstract</b>	<b>xv</b>
<b>1 Introduction and motivation</b>	<b>1</b>
1.1 History of laser-driven ion acceleration . . . . .	1
1.2 Methods of high repetition rate experiment . . . . .	3
1.2.1 Gas target . . . . .	4
1.2.2 Liquid target . . . . .	4
1.2.3 Solid target . . . . .	5
1.3 Methods of enhancing laser ion acceleration . . . . .	6
1.3.1 Optical methods . . . . .	6
1.3.2 Target design and composition . . . . .	7
1.4 Motivation and outline . . . . .	7
<b>2 Theoretical background</b>	<b>9</b>
2.1 Ultrashort pulse fundamentals . . . . .	9
2.2 A numerical method for simulating focus . . . . .	12
2.2.1 Two-step coordinate expansion transformation method for calculating focus	13
2.2.2 Some example results using this method . . . . .	15
2.3 Laser plasma interaction . . . . .	17
2.3.1 Definition . . . . .	17

2.3.2	Particle motion in relativistic electromagnetic field . . . . .	20
2.3.3	Ponderomotive force in high frequency electromagnetic field . . . . .	21
2.3.4	Absorption Mechanisms . . . . .	23
2.3.5	Laser ion acceleration mechanisms . . . . .	26
2.4	Numerical simulation methods for laser-plasma interaction . . . . .	31
<b>3</b>	<b>Experimental background and Facilities</b>	<b>33</b>
3.1	High power laser facilities . . . . .	33
3.1.1	ATLAS 300 laser facility . . . . .	34
3.1.2	CLAPA 200 TW laser facility . . . . .	36
3.2	Ion detectors . . . . .	37
3.2.1	Offline diagnostics . . . . .	37
3.2.2	Online diagnostics . . . . .	38
3.3	Spectrometer . . . . .	39
3.3.1	Wide angle spectrometer . . . . .	39
3.3.2	Thomson parabola spectrometer . . . . .	40
<b>4</b>	<b>High-repetition-rate laser-driven proton source</b>	<b>43</b>
4.1	Nano-foil target positioning system (nFTPS) . . . . .	43
4.1.1	Composition of nFTPS and positioning routine . . . . .	43
4.1.2	Characterization of nFTPS . . . . .	45
4.1.3	Advantages and disadvantages of the nFTPS . . . . .	47
4.2	0.5 Hz laser-driven proton source based on nFTPS . . . . .	47
4.2.1	Experimental setup . . . . .	47
4.2.2	Data processing . . . . .	49
4.2.3	Experimental results . . . . .	54
<b>5</b>	<b>A new method of enhancing proton energy</b>	<b>63</b>

---

5.1	Laguerre-Gaussian beam . . . . .	64
5.1.1	Generation methods . . . . .	66
5.1.2	Characteristics and applications . . . . .	67
5.2	Proton energy enhancement based on LG prepulse . . . . .	68
5.2.1	Experimental setup . . . . .	68
5.2.2	Experimental result and discussion . . . . .	69
5.3	The interaction between LG prepulse and target . . . . .	72
5.3.1	Introduction of MULTI program . . . . .	72
5.3.2	1D simulation with MULTI-IFE . . . . .	73
5.3.3	2D simulation with MULTI-2D . . . . .	77
5.3.4	Comparison of 1D and 2D MULTI results . . . . .	79
5.4	The interaction between the main pulse and the target . . . . .	81
5.4.1	Modeling of the initial plasma density distribution . . . . .	81
5.4.2	PIC simulation results . . . . .	82
5.4.3	Physical explanation . . . . .	83
5.4.4	Predictions . . . . .	85
5.5	Conclusions . . . . .	87
<b>6</b>	<b>Summary and outlook</b>	<b>89</b>
6.1	Summary . . . . .	89
6.2	Outlook . . . . .	90
	<b>Publications and upcoming publications</b>	<b>107</b>
	<b>Acknowledgements</b>	<b>111</b>



# List of Figures

2.1	The electric field of a monochromatic plane wave . . . . .	10
2.2	Schematic time evolution of the electric field of a Gaussian pulse. . . . .	11
2.3	Schematic diagram of coordinate transformation to calculate focus . . . . .	13
2.4	Beam profile before focus with FGB intensity distribution . . . . .	15
2.5	Profile at focus of a FGB beam . . . . .	16
2.6	Phase modulation . . . . .	16
2.7	Focus pattern with a spiral phase modulation . . . . .	17
3.1	Concept of the chirped pulse amplification (CPA) scheme . . . . .	34
3.2	Schematic Layout of the ATLAS 300 at LEX Photonics . . . . .	35
3.3	Layout of the CLAPA facility at Peking University . . . . .	36
3.4	Schematic of CLAPA 200 TW laser system. . . . .	37
3.5	Schematic of the novel electron and ion WASP . . . . .	39
3.6	Raw data obtained with stepped Aluminum layers covered on the detector . . . . .	40
3.7	Schematic of a typical TPS . . . . .	41
4.1	Components of nFTPS . . . . .	43
4.2	Schematic of nFTPS . . . . .	44
4.3	Deviation distribution of all targets . . . . .	45
4.4	Temporal evolution of average deviations . . . . .	46
4.5	The measurement of system vibration. . . . .	47

4.6	Schematic of experimental setup . . . . .	48
4.7	Backscatter spectrum raw data . . . . .	50
4.8	Incoming spectrum raw data . . . . .	50
4.9	Transmission image raw data . . . . .	51
4.10	Backscatter image of the equivalent plane monitor . . . . .	51
4.11	Near field image . . . . .	52
4.12	Far field image . . . . .	52
4.13	Proton signal raw data . . . . .	53
4.14	Pictures of target holder . . . . .	53
4.15	Schematic of target thickness and defocusing displacement . . . . .	54
4.16	Histograms of shot to shot performance . . . . .	54
4.17	Signal trends over thickness variation. . . . .	55
4.18	Defocus displacement variation in three cases . . . . .	56
4.19	Variation of laser pulse duration in three cases . . . . .	57
4.20	Variation of trigger time for fast Pockels cell . . . . .	58
4.21	Proton number as a function of Maximum kinetic energy . . . . .	59
4.22	Transmission as a function of backscatter signal . . . . .	59
4.23	Absorption rate $\eta$ . . . . .	60
4.24	Absorption and Transmission . . . . .	60
5.1	Hermite-Gaussian modes and Laguerre-Gaussian modes . . . . .	65
5.2	Schematic of the experimental setup . . . . .	69
5.3	Focal patterns of pre-pulses . . . . .	70
5.4	The size $r_i$ and $r_o$ . . . . .	70
5.5	Experimentally measured proton spectra . . . . .	71
5.6	The evolution of plasma density . . . . .	75
5.7	The scaling laws of density peak velocity . . . . .	76

---

5.8	The scaling law of expansion velocity . . . . .	76
5.9	The real Laguerre-Gaussian mode . . . . .	77
5.10	The evolution of plasma density . . . . .	78
5.11	The evolution of average plasma density . . . . .	79
5.12	Mass density distribution of the donut plasma . . . . .	80
5.13	The comparison of mass density distribution for 1D and 2D . . . . .	81
5.14	The electron density distribution model . . . . .	81
5.15	PIC simulation results using our model . . . . .	83
5.16	Physical explanation . . . . .	84
5.17	The proton spectra and maximum proton energy . . . . .	86
5.18	Maximum proton energy as a function of the radius $r_i$ of QIMT . . . . .	86
6.1	The simulation algorithm of time and space focusing . . . . .	91
6.2	Temporal contrast curves . . . . .	91



# List of Tables

5.1	The intensities of LG pre-pulses for scanning . . . . .	74
-----	---	----



# Zusammenfassung

In den letzten Jahrzehnten und mit der zunehmenden Verfügbarkeit hochintensiver Lasersysteme hat sich die Laserionenbeschleunigung zu einer ausgereiften und vielversprechenden Quelle für Experimente mit energetischen Ionen entwickelt. Insbesondere wurden in jüngster Vergangenheit Protonenenergien von fast 100 MeV erreicht. Die meisten Anwendungen erfordern eine stabile Ionenquelle mit hoher Wiederholungsrate. Die Verfahren und Strategien zur Realisierung solcher Laserionenquellen hoher Repetitionsrate variieren dramatisch, besonders in Bezug auf die verwendeten Targets.

Angesichts des Interesses unserer Forschungsgruppe an dünnen Festkörper-Targets lag der erste Schwerpunkt dieser Doktorarbeit auf einem automatisierten Targetpositionierungssystem, das zur Untersuchung verschiedener Forschungsthemen eingesetzt wird. Eine Pilotstudie mit Eintausend Targets wurde mit dem Nanofolientargetpositionierungssystem am ATLAS 300 im Laboratory for Extreme Photonics (LEX Photonics) durchgeführt, wo Laserpulse mit einer Pulsenergie von bis zu 6 J und einer Pulsdauer von 25 fs zur Verfügung standen. Durch Echtzeitüberwachung verschiedener Parameter der Laserpulse und Targets konnte die Stabilität der Protonenquelle bei einer Wiederholungsrate von 0,5 Hz bewertet werden. Im Rahmen dieser Studie wurden kontrollierbare Parameter künstlich variiert und deren Einfluss auf die Protonenausbeute untersucht. Die Ergebnisse waren zwar wissenschaftlich interessant, wiesen jedoch nicht eindeutig auf die Grundlage für die Stabilisierung der Protonenquelle hin. Es ist wahrscheinlich, dass räumlich-zeitliche Kontrastschwankungen einen wesentlichen Beitrag leisten. Diese können aber noch nicht für jeden individuellen Laserpuls überwacht werden.

Die Optimierung von Targets, die komplizierter sind als einfache Folien, hin zu hohen Wiederholungsraten stellt eine besondere Herausforderung dar. Zu den derzeit bevorzugten komplexeren Targets, die in dieser Arbeit besprochen werden, gehören Massen-limitierte targets (MLT). Ihre transversale Größe ist vergleichbar mit dem Laserfokusbereich. Daher bleiben die energetischen Elektronen auf ein mikroskopisch kleines Volumen gebunden, sodass die Beschleunigungsfelder ebenso wie die Ionenenergie erhöht werden. Die schnelle Positionierung von MLTs ist jedoch experimentell schwierig. Um Alternativen zu finden, haben wir die Erzeugung transientser Mikrotargets getestet, indem wir eine anfänglich ebene Folie mit einem Laguerre-Gauss (LG)-Vorpuls manipuliert haben. Dieser Vorpuls wurde im Frontend des CLAPA 200 TW-Lasers an der Peking-Universität eingeführt und durch eine Spiralphasenplatte (SPP) geleitet, bevor er mit einem zeitlichen Vorsprung von 1,7 ns zum Hauptlaserpuls wieder in die Laserkette geleitet wurde. Im Fernfeld, d.h. im Fokus auf der Target, führt der LG-Vorpuls zu einer donutförmigen Intensitätsverteilung und verursacht dadurch ein ringförmiges Plasma. Der Hauptlaserpuls fokussiert 1,7 ns später auf die Mitte dieses Rings. Die experimentellen Ergebnisse zeigten eine

Verdoppelung der Protonenenergie über einen relativ breiten Parameterbereich der Vorpulsintensität. Die zeitliche Entwicklung der Ring Vorplasma Expansion wird mathematisch modelliert und die Wechselwirkung zwischen dem Hauptpuls und dem transienten Mikroplasma durch Partikel-in-Cell Simulationen untersucht. Die Simulationsergebnisse können die experimentelle Beobachtung, insbesondere den Anstieg der Protonenenergie im relevanten Parameterbereich, reproduzieren. Das Ergebnis entspricht den Erwartungen, dass energetische Elektronen um den zentralen Teil des quasi-isolierten Mikrotargets konzentriert bleiben, obwohl das Target zum Zeitpunkt der Laser-Plasma-Wechselwirkung bei Spitzenintensität nicht vollständig isoliert, sondern von einem Plasma niedriger Dichte umgeben ist.

# Abstract

In the past few decades and with the increasing availability of high-intensity laser systems, laser ion acceleration has evolved into a mature and promising source for experiments with energetic ions. In particular, the latest laser-driven proton energy has reached nearly 100 MeV. Most applications require a stable ion source with high repetition frequency. The methods and strategies for realizing such repetitive laser-ion sources vary dramatically, in particular with respect to the employed target technology.

In view of the interest of our research group on solid thin targets, the first focus of this PhD work was on an automated target positioning system that is employed in various research topics. A pilot study with one thousand targets was conducted with the nano-Foil Target Positioning System at the ATLAS 300 at Laboratory for Extreme Photonics (LEX Photonics), which was able to deliver laser pulses with a pulse energy of up to 6J and a pulse duration 25fs. Through real-time monitoring of various parameters of the laser pulses and targets, we have evaluated the stability of the proton source at a repetition rate of 0.5 Hz. During this study, we artificially varied parameters that were controllable and studied their impact on the proton yield. While scientifically interesting, the results did not clearly reveal the basis that would allow for stabilizing the proton source. It is likely that spatial-temporal contrast fluctuations contribute, which cannot yet be monitored on shot-to-shot.

The request for repetition rate poses challenges to optimization strategies that rely on targets more complicated than plain foils. Among currently favored methods, which are reviewed in this thesis, are mass-limited-targets (MLT). Their lateral size is comparable to the laser focus diameter and therefore the energized electrons remain confined to a microscopically small volume such that acceleration fields are increased, as is the ion energy. However, the rapid positioning of MLTs is experimentally challenging. In order to find alternatives, we tested the generation of transient micro-targets by manipulating an initially plain foil with a Laguerre-Gaussian (LG) pre-pulse. This pre-pulse was introduced in the frontend of the CLAPA 200 TW laser at Peking University and passed through a spiral phase plate (SPP) before sending it back with a 1.7 ns advance to the main laser pulse into the laser chain. In the far-field, i.e. in the focus on the target, the LG pre-pulse results in a donut-shaped intensity distribution and initiates a ring-shaped plasma that is left to expand. The main laser pulse focuses on the center of this ring. The experimental results revealed a doubling of proton energy under the right pre-pulse intensity conditions. The evolution of the ring-pre-plasma expansion is modeled and the interaction between the main pulse with the transiently micro-plasma is studied by particle-in-cell simulations. The simulation results can recover the experimental observation, in particular, the proton energy increase in the relevant parameter range. Our understanding is in line with

expectations that energetic electrons remain concentrated around the central part of the quasi-isolated micro-target, even though the target is not fully isolated but surrounded by a low-density plasma by the time of laser-plasma interaction at peak intensity.

# Chapter 1

## Introduction and motivation

For inventing Chirped Pulse Amplification (CPA) technology [1] in 1985, Strickland and Mourou were awarded the Nobel Prize in Physics in 2018. Many related applications based on ultrashort laser pulse have been rapidly developed during the last three decades. CPA technology has enabled powerful pulses up to the terawatt or petawatt level. Laser-driven ion source development is one of the most interesting fields because 1, the effective ion source size is very small, typically a few microns; 2, the pulse duration of the ion source is very short, usually in the picosecond range. Such ion sources have proven potential in radiographic density diagnosis with  $\mu m$  resolution [2], in the isochoric heating of matter [3], in probing highly transient electric and magnetic fields [4], and may offer new approaches in medicine (for example, ion therapy [5]), in fusion energy (for example, fast ignition [6]), and so on.

### 1.1 History of laser-driven ion acceleration

Historically, the initial study of laser-matter interactions was driven by the idea of nuclear fusion through laser-compress ion of materials in the 1970s [7]. Crow et al. used the plasma isothermal expansion model to calculate the charge separation field that arises at the boundary of a plasma where it accelerate ions [8]. F. Mako and T. Tajima derived an ion energy distribution (a spectrum) in the framework of the reflexing beam model that was consistent with early experimental results [9]. During this time, the primary motivation of related research was laser-induced nuclear fusion.

In the 1990s, with the birth of CPA technology [1] and passive mode-locking technology [10], titanium: sapphire (Ti: sapphire) laser with high peak intensity became available. When the laser intensity exceeds  $> 10^{18} W/cm^2$ , the electrons quiver with relativistic velocity in a plasma can be accelerated over several light periods. The intensity regime is therefore called relativistic laser-plasma physics. The characteristics of relativistic plasma are: 1, little binary (hard) collisions [11]; 2, the direction of electron acceleration is predominantly along the direction of laser propagation due to the  $v \times B$  force becomes stronger than the E-field related force. In the case where the electrons are pushed forward, the inert ions react relatively slow. This results in an

electric field due to charge separation between the energized electrons and the plasma ions. The moving electrons also represent a current which in turn leads to varying magnetic field, which in turn result in electric fields and so on. The acceleration of ions by a laser (-driven plasma) is hence a result of the complex interplay between the laser pulse and the motion of electrons. It is worth noting that on the surface of a solid target, the impurities such as hydrocarbons and water are present and the protons are preferably accelerated because they obey the highest charge-to-mass ratio amongst all atomic nuclei. Because ion kinetic energies crossed the MeV range when the laser intensity approached  $10^{18} \text{ W/cm}^2$ , laser ion acceleration (in relativistic plasma) gradually became a dedicated research topic with promising research topic with promising applications.

In 1994, Fews et al. experimentally utilized a  $2 \times 10^{18} \text{ W/cm}^2$  picosecond laser pulse to interact with a solid target and obtained ion output above 1 MeV [12]. In 2000, Maksimchuk et al. inferred that the accelerated electric field gradient produced by the sub-picosecond pulse was as high as 10 GeV/cm, and explained the maximum energy of the protons via the charge separation field generated by the vacuum heating mechanism [13]. In the same year, Clark et al. obtained a proton beam with a maximum energy of 18 MeV via a picosecond pulsed laser ( $5 \times 10^{19} \text{ W/cm}^2$ ) interacting with a  $125 \mu\text{m}$  solid target [14]. Then, an energy spectrum exhibiting a sharp high-energy cutoff as high as 58 MeV was observed when a  $\approx 100\mu\text{m}$  thick solid target was irradiated by a 1 PW laser pulse [15]. Many experimental studies showed similar angular distributions and energy spectra of protons under similar laser and target parameters. However, there was an interesting controversy about whether the observed protons originated from the front or from the back (non-irradiated) surface of the target, and there was no uniform conclusion as to which acceleration mechanism dominated. Maksimchuk et al. found that when deuterium was attached to the front surface of the target, the boron sample on the back surface was activated, supporting that ions can be accelerated from the front surface of the target [13]. On the other hand, many groups found that the proton beam tends to follow the normal direction of the target rear surface. Snavely et al., for example, used a wedge-shaped target and observed two beams of protons perpendicular to the back of the wedge target. This observation can be interpreted as evidence for the important Target Normal Sheath Acceleration mechanism [15].

The ponderomotive force generated by the laser field leads to charge separation over a very short distance around the critical density layer on the front irradiated surface of the target. This will accelerate the ions to orders of the ponderomotive potential of the laser field ( $\sim 4 \text{ MeV}$  for  $10^{20} \text{ W/cm}^2$ ) and result in the drilling or hole-boring effect inducing the propagation of electrostatic shocks. According to this theory, some protons are subjected to a certain speed by the initial thrust transmitted via the radiation pressure of the laser pulse, and then are accelerated more effectively in the following electrostatic field, thereby higher proton energy can be achieved [16]. Therefore, a hybrid acceleration mechanism (Target Normal Sheath Acceleration and Radiation Pressure Acceleration [17]) can exist. In practice, it is hard to distinguish the contributions of the two acceleration mechanisms because it is not easy to independently measure various acceleration mechanisms [18]. This is because, on one hand, hydrogen elements are present as impurities on the surface of all target materials unless actively removed. On the other hand, the hydrogen elements in the lattice potential well of the target material can also be ionized and accelerated. It is worth mentioning that when the radiation pressure acceleration mechanism is dominant, the emitted ions can have the characteristic of a mono-energetic peak. We will come back to this chapter 2.

Over the years, the effects of target conditions (thickness, conductivity, shape, target artificially generated plasma) on ion output (yield, shape, composition, uniformity, maximum energy, etc.) [19, 20, 21]; the effects of laser parameters (intensity, pulse duration) on the highest energy of ions and the laser-ion conversion efficiency [22, 23] have been studied in numerous experiments and computer simulations. Interestingly, by special treatment of the target, a quasi-monoenergetic ion beam was obtained [24, 25]. Brambrink et al., studied the lateral characteristics of ion output demonstrating that the divergence angle of the ions is affected by the charge-to-mass ratio of the accelerated ions, and the law followed by the ion divergence and the evolution of the ion source size over time was derived [26].

Along the experimental studies the theoretical understanding matures. The ion energy can be predicted for current or future laser parameters. Predictions are supported through specific experiments [14, 22, 23, 27, 28], numerical simulations [27, 28, 29], and a number of theoretical models [30, 31, 32] exist. To predict ion energy and yield on the parameters of the laser pulse (intensity, pulse width, etc.). It has been found that the electron areal density of the target is an important parameter for a given laser intensity [29]. If the target electron areal density is less than the optimum value, the laser pulse is more transmitted than absorbed. Otherwise, the laser pulse is more reflected. There exists an optimum electron density at which the laser-ion conversion efficiency reaches a maximum.

With the maturity of the theory, the breakthrough of the target technology, and the continuous enhancement of the laser energy, researchers have increased the proton energy. Starting from the results in 2000, with the long standing record of 58 MeV maximum proton energy [15], it took until 2011 to increase this value to 67 MeV [33]. After another five years, the proton's cutoff energy reached 85 MeV [34]. Last year in 2018, Higginson et al., observed a proton beam of nearly 100 MeV in the RPA and TNSA hybrid acceleration mechanism [35]. Although there is still a gap to the deep penetration as it would be required for example for human tumor treatment (greater than 200 MeV) [5], it was speculated that the current proton energy might allow first approaches that do not require as high energy, such as eye cancer (greater than 62 MeV) [36].

## 1.2 Methods of high repetition rate experiment

In addition to appropriate laser technology, diagnostic equipment, theoretical and numerical simulation tools, target preparation and target control systems are vitally important for research of laser-matter interaction. Because under the existing laser conditions, the optimal thickness of the target is at the micrometer or even nanometer scale, target production, transportation and positioning is challenging. The repetition rate of most laser facilities is 1 – 10 Hz. In order to exploit this repetition in experiments, the targets need to be refreshed rapidly and the detection equipment should be run in real-time. In short, high-repetition experiments are technically much more challenging than the single-shot experiments. This chapter classifies according to the physical state of the target and summarizes the efforts of various research groups to potentially achieve high repetitive experiments.

### 1.2.1 Gas target

Homogeneous plasma with independently adjustable length and density can be generated using a pre-ionized gas jet [37]. In addition, the gas target is reasonably priced and does not require beam alignment and/or mechanical target movement between two consecutive shots, making it the preferred choice for many research groups as a highly repetitive target system. When a laser pulse propagates in a low-density plasma, the ponderomotive force of the laser pulse generates a large amplitude plasma wave. This plasma wave will then rupture and may capture some electrons and accelerate them, which is typically exploited for the laser wakefield acceleration mechanism that is widely used in the field of laser-driven electron acceleration [38]. The longitudinal acceleration of the electron is accompanied by a lateral betatron oscillation, which radiates strong X-rays, so the electron acceleration is also used for X-ray generation [39]. The low-density plasma described above is usually generated by the interaction of a laser pulse and the gas target, because the electron density in the gas target (between  $10^{18}$  and  $10^{19} \text{ cm}^{-3}$ ) is normally much smaller than the critical density  $n_c$ , so that the laser can propagate.

Generally, when the electron density is equal to or greater than the critical electron density, fast ion emission can be observed through the gas target. MeV ions have also been generated in underdense plasmas ( $n_e < 0.05n_c$ ), in which case the generation mechanism can be understood as a result of (transverse) Coulomb explosion processes [40]. In 2012, gas nozzles with adjustable density as high as  $10^{21} \text{ atoms/cm}^3$  and an operating frequency of 10 Hz based on a pressure pneumatic device became available [41]. Such gaseous thin targets are particularly suitable for laser-plasma interaction studies in the unexplored near-critical regime but are currently limited to thickness or lengths of greater than a few 10s of micrometers.

One main technical problem of such kind of target is that nozzle damage is not avoidable. For example, after  $10^4$  shots, the gas flux starts to show turbulence because the plasma plume produced in the laser-gas interaction accumulates to damage the nozzle. Another challenge is to enable the durability of magnetic valves in case of operation at 1kHz. Last but not least, 3D shaping and the formation of sharp gradients in the flow from the nozzle for low-density gas jets must be conquered to enable very thin near critical targets.

### 1.2.2 Liquid target

In comparison to gas, the high density of the liquid can be shaped as spherical or planar targets, which can be shaped into droplets, sprays or liquid crystal planar targets etc.

20 years ago, Liquid jet target (droplets) was developed for laser-plasma sources, such as EUV or X-ray [42]. Compared to conventional solid-target, this liquid target can be positioned close to the source without risking contamination or damages. More importantly, The liquid-target is regenerative, which can provide a fresh target at very high rates. The droplets can be produced by a several  $\mu\text{m}$  glass capillary nozzle, working with a certain backing pressure. The capillary is modulated by a piezo crystal to ensure a reproducible formation of a chain of tens of  $\mu\text{m}$  droplets [43]. Consisting of well defined 20  $\mu\text{m}$  diameter  $D_2O$  produced by the above piezoelectrically modulated nozzle, the liquid droplets were irradiated by the relativistic laser pulse and ion acceleration was observed [44]. Although some effort has been devoted to making sub- $\mu\text{m}$  droplet

sprays with high number density [45], the dispersed nature of the droplet cloud decreases the effective interaction region with the laser. Additionally, due to the spherical droplet expansion reducing the ion energy and yield, such droplet targets are as of now not ideal for ion acceleration.

Variable thickness liquid crystal film facilitates laser ion acceleration and can be used in high power laser optics such as plasma mirrors and wave plates due to its high planar quality [46]. This kind of target consists of a liquid crystal film freely suspended within a metal frame, which can be formed on-demand with thicknesses ranging from  $nm$  to  $\mu m$ . However, having a vapor pressure below  $10^{-6}$  Torr in the chamber, it has to be made at atmospheric pressure to maintain its initial thickness [47], which means it is only suitable for studying single-shot ion acceleration. A fast operation in-vacuum film formation was designed to be installed in-situ [46], the repetition rate of the device (0.1Hz) still needs to increase. Additionally, the thickness of the film depends strongly on the controlled delivery of very small volumes of fluid which is difficult to implement. The thickness will also change in time because of fluid flow after film formation, which leads to a big challenge of thickness control and stabilization. A possible drawback is a difficulty in incorporating high atomic number elements in liquid crystal targets [48]. The cryogenic hydrogen jet target is another promising, debris-free and renewable target that can provide continuous sheet-like jets through a rectangular aperture [49].

In summary, with regard to laser ion acceleration, droplets and droplet sprays can easily achieve high repetition rates, but are not ideal due to poor ion emission quality. Liquid crystal planar targets have potential, but film formation conditions in vacuum hinder the repetition rate and versatility.

### 1.2.3 Solid target

Solid targets are the most common targets used for laser ion acceleration, as they offer more variety in thickness and elemental composition. Due to their fixed physical state, the different combinations of multilayers [50, 51], special shape (concave shape on the back side) [52], various thicknesses [15] are accomplished and studied. As mentioned in reference [35], an efficient proton acceleration to energies exceeding 94 MeV via a double-peaked electrostatic field structure was demonstrated, which showed a great potential to achieve high quality and high energetic proton source via solid targets. However, the mature TNSA and RPA mechanisms tell us that the optimal thicknesses under different laser conditions (intensity, contrast ratio, etc.) are in the range of several  $nm$  to tens of  $\mu m$  [53, 54, 55, 56]. Commercial foils with a thickness smaller than  $1 \mu m$  are normally produced by physical vapor deposition (PVD) or chemical vapor deposition (CVD), while foils with a thickness of several  $\mu m$  are normally rolled from thicker foils. Spin coating or droplet method is used to produce ultra-thin targets. Regarding the process of the droplet method, the solvent-dissolved polymer is first dropped on the surface of pure water, and then the solvent is evaporated in a few seconds. After a thin polymer film is formed, it can be transferred to the target holder by floating [57].

During the laser-matter interaction, the damage in neighboring targets is a severe problem for refreshing the solid targets. Target material can be ionized at intensity  $I \geq 10^{13} W/cm^2$ . When dealing with intensity of  $10^{21} W/cm^2$ , the targets that are a few mm away may survive and don't need protection [58]. Therefore, high repetition rate experiments using solid targets involve

more target localization and alignment, which means that a target positioning system should be designed to account for these issues. A crucial requirement for such a system with a high repetition rate is that the sample must be positioned with  $\mu m$  precision in longitudinal and lateral directions at the right time (for 1 Hz, 1 second including the motion time and vibration release time). The user-friendly system should be flexible enough to accommodate different kinds of targets and possibly characterize targets.

Regarding the high-repetition target positioning system, Prencipe et al., gave very detailed comments about different concepts [48]. For example, the High Repetitive Rate Sample Delivery (HIREP) work package of the European Cluster of Advanced Laser Light Sources (EUCALL) is developing an integrated concept for dispersing sample characterization and rapid sample replacement. The system consists of a flat carrier frame (specific to each partner facility) and an internal target framework shared by all partner facilities (including ELI pillars, European XFEL, HZDR, Max IV, DESY) [59]. The concept model of a ladder positioning system and target fielding system concept (cinema film projector mechanism) are also interesting and efficient solutions for high repetition rate experiments [48]. In Chapter 3, I will describe the target positioning system we have developed for the LION chamber in LEX and CALA, its relevant characteristics and the challenge performing a 1000 shots study at a 0.5 Hz repetition rate.

### 1.3 Methods of enhancing laser ion acceleration

As mentioned in references [23, 27], the scaling law of ion acceleration driven by ultra short laser pulses has been studied. It is easy to understand that with the same energy conversion efficiency, the higher laser energy leads to the higher ion energy. However, this is not the subject of this section. For example, with a fixed laser intensity of  $10^{18} W/cm^2$ , the maximum proton energy was improved more than twice by extending the pulse duration from 1.5 to 6 ps [60] meaning the laser energy was increased by a factor of 4. In this section, methods involving increasing the ion acceleration are those that can improve the efficiency of laser to ion conversion. In the current stage of laser intensity ( $< 10^{24} W/cm^2$ ), first the electromagnetic (EM) field of the laser pulse drives the electrons which then set up the charge separation field that accelerates the ions. This means the laser does not interact with the ions directly. Therefore, one possibility for improving the laser-ion conversion efficiency is to increase the number and/or temperature of the electrons that participate in the formation of the accelerating field.

#### 1.3.1 Optical methods

One method is to suppress the prepulse and ASE while reducing the target thickness to an optimum value. For a given laser contrast, pulse duration and intensity, the optimal thickness is proven to exist [53, 61]. To suppress prepulse and ASE, one can introduce a fast Pockels cell [23, 24, 62, 63] which allows the pulse to start passing at a certain time (normally hundreds ps before the arrival of the main pulse) and it can reduce the ASE level by more than two orders of magnitude. Plasma mirror configurations are very common as self-inductive plasma shutters, which can also achieve two orders of magnitude improvement in temporal contrast for each plasma mirror [56, 64]. Importantly, a fast Pockels cell and a plasma mirror can be used in

combination.

But also adding an artificial prepulse before the main pulse could be used such that the laser-energy deposition onto targets can be controlled [65]. Significant enhancement in the maximum proton energy and laser-proton energy conversion efficiency was observed at optimum preplasma density gradients, due to self-focusing of the incident laser pulse [66] or to the existence of a two-stage acceleration process [67]. Interestingly, the introduction of a high-contrast short prepulse tens of ps prior to the main pulse can control the spectral shape of the ion beams and even can achieve quasi-monoenergetic ions [68].

### 1.3.2 Target design and composition

Except for manipulating the laser, target design and composition enables control over ion acceleration. For example, a flap-top cone target can produce a proton beam with maximum energy that exceeds the flat foil target, up to 2.4 times, which is attributed to the cone targets special geometry that guides the hot electrons to the flat top of the cone [69]. Reducing the target thickness is an option to enhance the laser ion acceleration owing to the hot electron recirculation within the target increasing the static electrical field at the rear surface [53] or to self-induced transparency leading to strong volumetric heating in the target [56]. Attached in front of nm thin Diamond-Like-Carbon (DLC), Carbon-Nanotube-Foam (CNF) can be used to realize relativistic self-focusing and pulse front steepening at the same time, which results in an enhanced laser ion acceleration [51]. Reducing the target transverse size can limit the lateral diffusion of hot electrons at the target edge, and then a hotter, denser and more uniform electron sheath around the target will increase the maximum proton energy [70, 71]. In particular, when the foil diameter is smaller than the laser focal spot size, the effect of Coulomb expansion can lead to significant ion energy enhancement. [72].

In summary, enhancement can be achieved either by suppressing the pre-pulse and ASE, or by multi-pulse coupling, or by target design or combination. However, considering the high repetition rate experiments, the all-optical approach seems most promising.

## 1.4 Motivation and outline

The road to a stable ion source with a high repetition rate is still long and arduous. One of the purposes of this thesis is to establish a nano-foil target positioning system to achieve a 1 Hz proton source and explore the effects of laser parameters, target parameters and positioning system accuracy on the stability of the proton source. Another purpose is to propose an enhancement method that is compatible with high repetition rate experiments. Therefore, the outline of this thesis is as follows. Some theoretical background is introduced in Chapter 2. Experimental methods and facilities are described in Chapter 3. The target positioning system concept and its implementation to perform a 1000 shots experiment at 0.5 Hz in Chapter 4. Finally, an all-optical method for enhancing ion acceleration is proposed and first results are presented in Chapter 5. Chapter 6 summarises the results, presents and outlook.



## Chapter 2

# Theoretical background

This chapter will focus on ultrashort pulse fundamentals, absorption of the laser in the over-dense plasma and different laser ion acceleration mechanisms to cover the background involved in this work. The laser pulse used in the experiments is a few optical cycle pulse with a broadband spectral (750 nm to 850 nm) and the pulse duration is tens of femtoseconds. The targets used in the experiments are plastic foils which form an over-dense plasma after ionization and are typically not transparent for the ultra high intensity pulses.

The first section will introduce the basic concepts of the mathematical description of ultra-short pulses in the time and frequency domain and their propagation, including the focusing by the off-axis parabolic mirror. This part sheds some new light onto the temporal contrast at focus. The second section will introduce absorption mechanisms. Of particular importance is ablation by fs laser pulse that is relevant to Chapter 5. The third section will present laser ion acceleration mechanisms and in this thesis, TNSA is the most relevant mechanism. About the background of interaction with a single atom, a single electron or under-dense plasma, one can refer to the books [73, 74].

### 2.1 Ultrashort pulse fundamentals

Because the energy of a laser pulse can be concentrated in a time interval as short as tens of  $10^{-15}$  seconds, which corresponds to only a few optical cycles in the visible range, the pulse peak power can be extremely large even at moderate pulse energy. For instance, a 25 fs pulse with an energy of 1 J exhibits an average power of 40 Terawatt. Focusing this pulse to a  $100\mu\text{m}^2$  spot yields an intensity of  $4 \times 10^{19} \text{ W/cm}^2$ . The intensity is related to the magnitude of the time-averaged Poynting vector. Note that the Poynting vector  $\vec{S} = \vec{E} \times \vec{H}$ , and  $|\vec{H}| = \sqrt{\epsilon_0/\mu_0}|\vec{E}|$  for an electromagnetic wave in vacuum, where  $\epsilon_0$  and  $\mu_0$  represent the permittivity and the permeability of vacuum, respectively. Thus, the intensity can be described as

$$I = |\langle \vec{S} \rangle| = |\langle \vec{E} \times \vec{H} \rangle| = \sqrt{\epsilon_0/\mu_0} |\langle \vec{E} \rangle|^2 \quad (2.1)$$

which, in particular, can be written as  $I = E_0^2/2Z_0$ . Here,  $E_0$  is the magnitude of the electric field  $\vec{E}$  and  $Z_0$  is the impedance of free space, with a value of about 376.7 ohms. Therefore, we

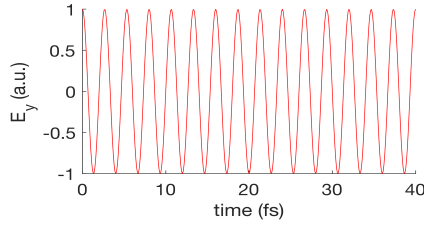


**Figure 2.1:** Schematic time evolution of the electric field of a monochromatic plane wave.  $\lambda = 800nm$

can calculate the electric field from the intensity. For example, the mentioned intensity  $4 \times 10^{19} W/cm^2$  represents an electric field strength of about 173 GV/cm, which is far stronger than a typical inner-atomic field of 1 GV/cm. Actually, the laser pulse with intensities of  $10^{13} W/cm^2$  (corresponding to  $E_0 \approx 87 MV/cm$ ) and above directed onto solid targets is sufficient to strip electrons from their nuclei, resulting in a laser-generated plasma. This section will focus on how to mathematically describe the electric field of a laser pulse.

We start with Maxwells equations as,

$$\nabla \cdot \vec{D} = \rho \quad (2.2)$$

$$\nabla \cdot \vec{B} = 0 \quad (2.3)$$

$$\nabla \times \vec{E} = -\frac{\partial \vec{B}}{\partial t} \quad (2.4)$$

$$\nabla \times \vec{H} = \vec{J} + \frac{\partial \vec{D}}{\partial t} \quad (2.5)$$

Here,  $\vec{E}$ ,  $\vec{D}$ ,  $\vec{H}$  and  $\vec{B}$  denote the electric field, electric flux density, magnetic field and magnetic flux density, respectively.  $\rho$  is the charge density and  $\vec{J}$  is the current density. The wave equation in vacuum can be derived from the Maxwell's equation [75] as

$$\nabla^2 \vec{E} = \epsilon_0 \mu_0 \frac{\partial^2 \vec{E}}{\partial t^2} \quad (2.6)$$

The wave equation 2.6 is a second-order differential equation, whose simplest propagating solution is the retarded plane wave,

$$E_y = Re(E_0 e^{i\omega(t-x/c)}). \quad (2.7)$$

The solution 2.7 describes the propagation of a transverse electric field along the positive  $x$  axis, in which  $c$  is speed of light in vacuum and  $c^2 = 1/(\epsilon_0 \mu_0)$ . In order to introduce the wave vector  $k$  of the light, we can rewrite the solution 2.7 as,

$$E_y = Re(E_0 e^{i(\omega t - k \cdot r)}), |k| = \omega/c = 2\pi/\lambda \quad (2.8)$$

where  $r$  represents the distance from the origin point. From 2.7 and 2.8, we can see that a plane wave is periodical with infinite duration and specific frequency  $\omega$ .

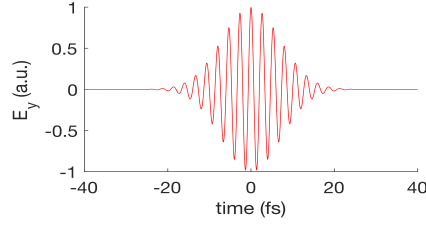


**Figure 2.2:** Schematic time evolution of the electric field of a Gaussian pulse.

Notice that due to the finite width, Figure 2.1 represents a continuous wave with a rectangular envelop. Based on this wave, we multiply it by a Gaussian function, then we can get a Gaussian pulse as shown in the Figure 2.2.

In Fig 2.2, the pulse is built up by multiplying the plane wave function by a Gaussian envelope function  $e^{-\tau t^2}$ , where  $\tau$  is the shape factor of the Gaussian envelope and is proportional to the inverse of the squared duration  $t_0$ , i.e.  $\tau \propto t_0^{-2}$ . As known, the Fourier transform of a Gaussian pulse is also a Gaussian function while the Fourier transform of a plane wave with the unique angular frequency  $\omega_0$  is a Dirac distribution  $\delta(\omega_0)$ . In other words, the frequency content of a pulse is much larger than in case of a monochromatic wave.

The mathematical descriptions of the Fourier transform in time and frequency domain are:

$$E(\omega) = \int_{-\infty}^{+\infty} E(t)e^{-i\omega t} dt, \quad (2.9)$$

$$E(t) = 1/2\pi \int_{-\infty}^{+\infty} E(\omega)e^{i\omega t} d\omega. \quad (2.10)$$

In time domain, the electric field is a real quantity but it is convenient to describe it as a complex analytical signal [76],

$$E^+(t) = E(t) + i\mathcal{H}[E(t)], \quad (2.11)$$

where  $\mathcal{H}$  represents the Hilbert transform. Therefore, we can rewrite the electric field in the following way,

$$E^+(t) = |E^+(t)|e^{i\tau(t)} = |E^+(t)|e^{i(\omega_0 t + \phi(t) + \phi_0)}, \quad (2.12)$$

where  $e^{i\tau(t)}$  is a similar envelope function, as we discussed above. The phase  $\tau(t)$  is a function of the laser frequency  $\omega_0$ , a time-dependent phase  $\phi(t)$ , and carrier envelope phase  $\phi_0$ .

Now, we assume a practical situation that a pulse propagates through a cross section  $A$ , and with a relevant component of the electric field  $E(t)$ , as mentioned. The pulse power in a material without any dispersion effect can be calculated from the Poynting theorem of electrodynamics [77] and is given by,

$$\mathcal{P}(t) = \epsilon_0 c n \int_A dS (1/T) \int_{t-T/2}^{t+T/2} E^2(t') dt' \quad (2.13)$$

where  $n$  stands for the refractive index of the material and  $\int_A dS$  denotes integration over the beam cross section. The corresponding quantity per unit area is the intensity ( $W/cm^2$ ):

$$I(t) = \epsilon_0 cn(1/T) \int_{t-T/2}^{t+T/2} E^2(t') dt' = 2\epsilon_0 cn |E^+(t)|^2, \quad (2.14)$$

$$I(\omega) = (\epsilon_0 cn/\pi) |E^+(\omega)|^2, \quad (2.15)$$

where  $T = 2\pi/\omega$  is the oscillation period and

$$E^+(\omega) = \mathcal{F}[E^+(t)] = \begin{cases} E(\omega) & \text{for } \omega \geq 0 \\ 0 & \text{for } \omega < 0 \end{cases} \quad (2.16)$$

The important characteristics of a laser pulse temporal duration  $\tau_p$  and spectral width  $\Delta\omega_p$  can be obtained by the full width at half maximum (*FWHM*) of the intensity profile in time domain and frequency domain, respectively.

$$\tau_L = FWHM[I(t)], \quad (2.17)$$

$$\Delta\omega = FWHM[I(\omega)]. \quad (2.18)$$

The product of the two parameters has a lower limit [76],

$$\Delta\omega\tau_L \geq c_B, \quad (2.19)$$

where the constant  $c_B$  depends on the shape of the pulse. For Gaussian pulses,  $c_B = 4\ln 2$ .

## 2.2 A numerical method for simulating focus

In light propagation, a quadratic phase modulation plays an important role. This is because a spherical wavefront can be approximated by a quadratic phase ( $\phi(y) \propto y^2$ , where  $y$  is the transverse dimension) near any propagation axis. Imparting a quadratic spatial phase modulation will result in focusing or defocusing of a beam while in temporal domain, a quadratic phase modulation  $\phi(t) \propto t^2$  will lead to pulse compression or broadening after propagating through a dispersive medium. The problems relating to pulse propagation, such as chirped pulse, the reduced wave equation, dispersion in a transparent medium have been discussed in the books [76] [77]. Here, we consider the description of focusing of a laser. Due to the typical large aperture of the beam, it is often insufficient to approximate the focal intensity distribution by a 2D Fourier transform. In particular, a regular grid is not efficient to simulate a strongly converging or diverging beam.

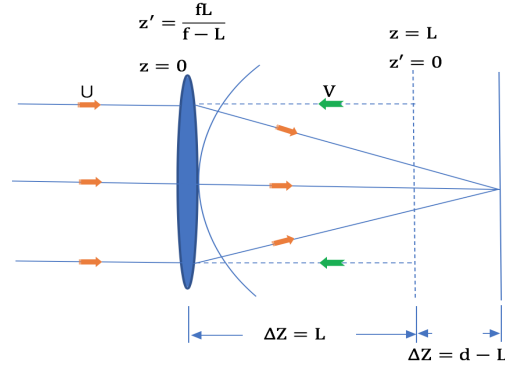


**Figure 2.3:** Schematic diagram of coordinate transformation to calculate focus

### 2.2.1 Two-step coordinate expansion transformation method for calculating focus

We describe the complex amplitude distribution function  $U(x, y, z)$  of the optical field propagating in free space by the paraxial equation

$$\frac{\partial^2 U}{\partial x^2} + \frac{\partial^2 U}{\partial y^2} - 2jk \frac{\partial U}{\partial z} = 0. \quad (2.20)$$

This equation can be expanded by a Fourier transform to convert the optical field propagation in the spatial domain into a frequency domain calculation. It is usually solved numerically using two FFTs. Now we consider that a laser propagates through an ideal thin lens focusing system. The complex amplitude distribution of the laser before the lens is  $U_0(x, y)$ , and the complex amplitude distribution function after the lens having the focal length  $f$  is

$$U_1(x, y) = U_0(x, y) \mathcal{T}(x, y) = U_0(x, y) \exp\left(-jk \frac{x^2 + y^2}{2f}\right) \quad (2.21)$$

Calculating the focused beam is to divide the complex amplitude distribution function  $U_1(x, y)$  on the back surface of the lens into the light field distribution after calculating the propagation distance  $d$ . Since the focused beam is much smaller than the lateral dimension of the incident beam, the direct FFT calculation will be inefficient. Therefore, we use the coordinate transformation two-step calculation method. Fig.2.3 shows a schematic diagram of the two-step coordinate transformation FFT method for calculating the focusing, where solid lines denote the light propagation in real space  $(x, y, z)$  and virtual lines represent that in virtual space  $(x', y', z')$  through coordinate transformation.

**The first step:** the condensed spot  $U_L(x, y)$  at the distance  $L$  is calculated using the FFT method of coordinate expansion transformation. The main purpose is to reduce the spatial scale of the calculation. Because of the same number of sampling grids, the small-scale space can describe the light field distribution of the same feature in more detail. The lens is located at  $z = 0$ , the vertical virtual line is at  $z = L$ , and the focal spot is at  $z = d$ . So we can do the following transformation,

$$U(x, y, z) = (f - z)^{-1} e^{j[\pi/(f-z)\lambda](x^2+y^2)} V(x', y', z'), \quad (2.22)$$

where  $(x', y', z')$  is the coordinate in the new coordinate system having a relationship with the original coordinate as below,

$$\begin{aligned} x'(x, z) &= fx/(f - z), \\ y'(x, z) &= fy/(f - z), \\ z'(x, z) &= f^2[L - z]/[(f - z)(f - L)]. \end{aligned} \quad (2.23)$$

$L$  is the distance that propagated by the wave function  $U(x, y, z)$  in the real space. Now, we substitute the formula 2.22 and 2.23 into the paraxial equation 2.20. Setting  $\beta = f - L$ , the corresponding items of equation 2.20 are,

$$\begin{aligned} \frac{\partial^2 U}{\partial x^2} &= \frac{1}{\beta} \exp \left[ \frac{jk(x^2 + y^2)}{2\beta} \right] \left( \frac{-k^2 x^2}{\beta} V + \frac{jk}{\beta} V + \frac{2jkfx}{\beta^2} \frac{\partial V}{\partial x'} + \frac{f^2}{\beta^2} \frac{\partial^2 V}{\partial x'^2} \right), \\ \frac{\partial^2 U}{\partial y^2} &= \frac{1}{\beta} \exp \left[ \frac{jk(x^2 + y^2)}{2\beta} \right] \left( \frac{-k^2 y^2}{\beta} V + \frac{jk}{\beta} V + \frac{2jkyf}{\beta^2} \frac{\partial V}{\partial y'} + \frac{f^2}{\beta^2} \frac{\partial^2 V}{\partial y'^2} \right), \\ \frac{\partial U}{\partial z} &= \frac{1}{\beta} \exp \left[ \frac{jk(x^2 + y^2)}{2\beta} \right] \left[ \frac{V}{\beta} + \frac{jk(x^2 + y^2)}{2\beta^2} V + \frac{fx}{\beta^2} \frac{\partial V}{\partial x'} + \frac{fy}{\beta^2} \frac{\partial V}{\partial y'} + \frac{fz}{\beta^2} \frac{\partial V}{\partial z'} \right]. \end{aligned} \quad (2.24)$$

After derivation, the transformed wave function  $V(x', y', z')$  is the same as  $U(x, y, z)$  and also satisfies the paraxial equation as below,

$$\frac{\partial^2 V}{\partial x'^2} + \frac{\partial^2 V}{\partial y'^2} - 2jk \frac{\partial V}{\partial z'} = 0. \quad (2.25)$$

Then,  $V(x', y', z')$  can also be solved by Fourier transform, which needs to be done in a new coordinate space. Corresponding to the axial propagation distance  $L$  of the wave function  $U$  in real space, the axial propagation distance of  $V$  in the new coordinate space of the transformation is  $L'$ , which is a negative value and can be realized by diffraction inverse operation. At different positions of the optical axis,  $(x', y')$  in the new coordinate system corresponds to the actual  $(x, y)$  space, and the scale factor of the expansion is different. That is, the scale factor is the value of the change associated with  $z$ . Therefore, the problem of converging the propagating beam  $U$  along the  $z$ -axis is transformed into the propagation problem of the equivalent collimated parallel beam  $V$  in the new coordinate system.

**The second step:** Using  $U_L$  as the input wave function, directly apply the FFT method of non-expanded coordinates to calculate the distribution of the light field near the focus after the propagation distance  $d - L$ . In the calculation, the angular spectrum diffraction formula is used as a frequency domain transfer function.

The steps in detail are below.

1) substitute  $z = 0$  into equations 2.22 and 2.23 to obtain the surface wave function  $U_1$  as,

$$U_1(x, y, 0) = f^{-1} \exp[j(\pi/f\lambda)(x^2 + y^2)] \times V_1(x', y', fL/\beta). \quad (2.26)$$

Comparing equation 2.26 to equation 2.22, we get  $z = 0$ . So at position  $z' = fL/\beta$ , we have

$$V_1(x', y', fL/\beta) = U_0(x, y, 0)f, \quad (2.27)$$

where  $U_0$  is the output wave function.

2) In the new coordinate system  $(x', y', z')$ ,  $V_1$  is the input wave function and using the diffraction inverse FFT method to calculate  $V_L(x', y', 0)$  in which the propagation distance is  $-fL/\beta$ .

3) Substitute  $V_L(x', y', 0)$  into equation 2.22 to get the field distribution  $U_L(x, y, L)$  in  $(x, y, z)$  space.

4) In  $(x, y, z)$  space,  $U_L(x, y, L)$  as the input function, applying FFT to obtain the field distribution at focus after diffraction propagation distance  $d - L$ .

The essence of the coordinate transformation is the geometric scaling of the spatial scale, and the scale varies along the z-axis. The lateral spatial scale at the focus is 0, which obviously does not take into account the actual diffraction limit. According to the Fourier transform characteristics of thin lenses, the light field distribution at the focal plane can be directly calculated using FFT. The light field distribution of the focal plane is proportional to the Fourier transform of the incident light wave. For the distribution of the light field near the focal plane, the two-step calculation method not only takes advantage of the coordinate transformation, but also avoids the contradiction between the geometric scaling of the coordinate space and the diffraction limit. This allows us to simulate the focused light field distribution for a large laser beam [78].

### 2.2.2 Some example results using this method

**1) near-field intensity modulation** For high power laser systems with large aperture, it is very common to shape the light beams into flattened Gaussian beams (FGBs) in order to achieve higher energy extraction efficiency and suppress the growth of nonlinearities. In reference [79], the normalized field distribution for a FGB with order  $N$  and spot size  $W_0$  is described as below,

$$I_N(r) = \exp\left[-\frac{(N+1)r^2}{W_0^2}\right] \sum_{n=0}^N \frac{1}{n!} \left(\frac{\sqrt{N+1}r}{W_0}\right)^{2n}, \quad (2.28)$$

where  $r$  is the radial coordinate, the order  $N$  controls the steepness of the edge. An example of a beam profile with order  $N = 9$  and  $W_0 = 100\text{mm}$  is shown in Fig.2.4.

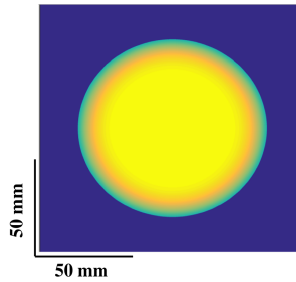


**Figure 2.4:** Beam profile before focus with FGB intensity distribution

The profile of the beam in the focus plane is shown in Fig.2.5. The focus is magnified to a ten micron window and the number of grid points is the same as defined for the non-focused beam.

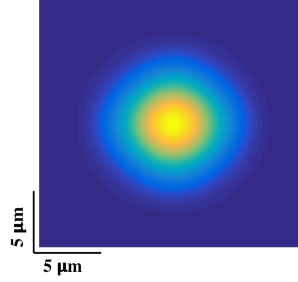


**Figure 2.5:** Profile at focus of a FGB beam

**2) spiral phase modulation** Applying a spiral phase plate (SPP) to a coherent beam in the near field results in an optical vortex beam in the far field, where it exhibits a characteristic donut-shaped transverse profile. An integer number of  $2\pi$  phase accumulation around one turn of the spiral wavefront corresponds to the azimuthal index  $m$  of the Laguerre-Gaussian mode ( $LG_{p,l}$ ), which is referred to the topological charge of the SPP. With the radial mode index  $p=0$ ,  $LG_{p=0,l}$  mode is azimuthally symmetric in magnitude and the intensity vanishes at the center due to the phase singularity. In cylindrical coordinates, the spatial laser field in focal plane can be simply described by [80]

$$I_{LG}(r) \propto \left(\frac{\sqrt{2}r}{\omega_0}\right)^{2l} (L_0^l(2\frac{r^2}{\omega_0^2})) \exp(-2\frac{l^2}{\omega_0^2}), \quad (2.29)$$

where  $r$  is the radial distance,  $L_0^l$  is the associated Laguerre polynomial and  $\omega_0$  is the beam waist at position  $z = 0$ . The radius of the maximum intensity,  $r_{max}$  of such mode is then given by

$$r_{max} = \sqrt{\frac{z_R l}{k}} = \omega_0 \sqrt{\frac{l}{2}}, \quad (2.30)$$

where  $z_R$  is the Rayleigh range and  $k$  is the wave number.

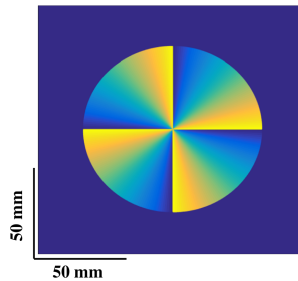


**Figure 2.6:** Phase modulation with topological charge  $m = 4$ , the color represents the phase.

Therefore, one can estimate the ring size of the pre-pulse based on the topological charge of SPP and the beam waist. As shown in Fig. 2.6, a spiral phase modulation with topological charge of 4 is plotted and the focus pattern is shown in Fig.2.7. The theory and the numerical simulation method of this section are the basis for the simulation of time contrast at the focus. By changing the phase mode, we can control the light field distribution after focusing. Specifically, the Gaussian pre-pulse can be modulated into a Laguerre Gaussian beam, i.e., a ring-shaped focal intensity distribution. It will be demonstrated later how this modification can be used to

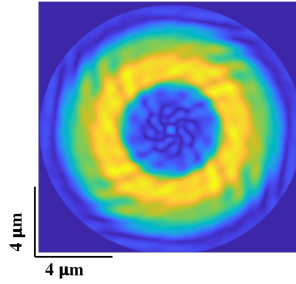


**Figure 2.7:** Focus pattern with a spiral phase modulation

pre-process the target. Due to the unique nature of femtosecond laser pulses, the precision of this machining can reach nanometer levels. The size of the ring can be adjusted to a few microns, which is the basis for the formation of the transiently isolated micro-plasma in Chapter 5.

## 2.3 Laser plasma interaction

### 2.3.1 Definition

Plasma is defined as an unbound state macroscopic system composed of a large number of charged particles. The plasma consists of free particles with positive and negative charges. The particles interact via long-range electromagnetic forces. Its most important feature in the context of relativistic laser interaction is the collective motion behavior of the particles.

In the first chapter, we reviewed the use of targets of different material states, i.e. solid, liquid, and gaseous. The plasma is often considered as the fourth state of matter, which can be obtained by the phase change of the first three states by heating. Specifically, the solid is first liquefied after heating and will be vaporized after further heating. As the temperature continues to rise, the thermal kinetic energy between the atoms is comparable to the ionization energy, and the neutral gas becomes a partial (or complete) ionized gas. At this time, the long-range electromagnetic force between the ions and the electrons starts to function, and the system exhibits a new motion characteristic. The higher the degree of ionization, the more pronounced the plasma properties become.

### Plasma description method

In most cases, plasma is a classic, non-relativistic system. Quantum effects are only important when the spacing between the ions is comparable to the De Broglie wavelength of the particles which is largely irrelevant for the matters discussed here. Because the temperature of the plasma rises sharply in the focus of the high-power laser and the electrons reach relativistic velocity in a short time, making the relativistic description necessary. For such high velocities, the collision frequency between particles is small. Therefore, a simplified model, the collision-free plasma model, was proposed by Vlasov. In the framework of statistical mechanics, the particle

distribution function is used to describe the state of plasma macroscopically. This model is widely used in high-temperature plasma theory and numerical simulation. The Particle-In-Cell (PIC) simulation related to this theory will be introduced in the following chapters.

In the framework of fluid mechanics, a plasma can be regarded as a fluid dominated by electromagnetic interaction. The described method is commonly referred to as magneto-hydro-dynamic (MHD) or electromagnetic MHD (EMHD). Specific kinetic variables are density, temperature, and mean velocity. The whole process of fluid motion can be obtained by the momentum equation, the continuity equation, and the state equation. The numerical simulation method based on this fluid mechanics approach will also be introduced in the following chapters.

### Debye shielding

As the plasma consists of free charged particles, it prevents establishment of electric fields. This is the Debye shielding effect of the plasma. The length scale over which fields are shielded is called the Debye length. For low temperature plasmas, we can assume that the Debye shielding process is a static process in which the electrostatic field satisfies the Poisson equation,

$$\nabla^2\psi = -\frac{e}{\epsilon_0}(n_i - n_e), \quad (2.31)$$

where  $n_i$  and  $n_e$  refer to the number density of ions and electrons, respectively. In the thermal equilibrium and for non-relativistic velocities, they satisfy the Boltzmann distribution,

$$n_i = n_0 \exp(-e\psi/k_B T_i), \quad n_e = n_0 \exp(e\psi/k_B T_e), \quad (2.32)$$

where  $k_B$  is Boltzmann constant,  $T_i$  and  $T_e$  are ion and electron temperatures, and  $n_0$  is a plasma density at zero potential. Based on equations 2.32 and assuming a same temperature for ions and electrons, we can get

$$n_e/n_i = \exp(2e\psi/k_B T_e). \quad (2.33)$$

In case of  $e\psi/k_B T_e \gg 1$ , it has  $n_e \gg n_i$ , which means that the electrons are trapped in large quantities, the ions are emptied, and the electric field generated by the electrons shields most of the potential. If we only study the space where the potential satisfies  $e\psi/k_B T_e \ll 1$ , then substituting the equation 2.32 into the Poisson equation 2.31 and doing Taylor expansion, taking one term, we can get the following formula,

$$\nabla^2\psi = \left(\frac{n_0 e^2}{\epsilon_0 k_B T_i} + \frac{n_0 e^2}{\epsilon_0 k_B T_e}\right)\psi \triangleq \frac{1}{\lambda_D^2}\psi \quad (2.34)$$

Here, and  $\lambda_D$  is the Debye length of the plasma. The Debye lengths of ions and electrons are  $\lambda_{De}$  and  $\lambda_{Di}$ , respectively.

$$\lambda_{Di,e} \triangleq \left(\frac{\epsilon_0 k_B T_{i,e}}{n_0 e^2}\right)^{1/2}, \quad \lambda_D \triangleq (\lambda_{Di}^{-2} + \lambda_{De}^{-2})^{-1/2}. \quad (2.35)$$

In the one-dimensional case, the solution of the equation 2.34 is,

$$\psi(x) = \psi_0 \exp(-|x|/\lambda_D). \quad (2.36)$$

That means the potential will penetrate into the plasma in the form of exponential decay. The spatial scale of the external electric field of the plasma shield is the Debye length defined by equation 2.35.

### Plasma characteristic response time

The Debye length is the basic length unit of the plasma system, and the characteristic response time is its basic time unit. The plasma is able to limit any spatial interference to the shell of the Debye length, and it takes time to establish such a shield. This time is the characteristic response time of the plasma to the external disturbance, which can be defined by the time required for the electron to cross the shell space at the average thermal velocity  $\nu_{Te} = \sqrt{k_B T_e / \gamma m_e}$ ,

$$\tau_{pe} \triangleq \frac{\lambda_{De}}{\nu_{Te}} = \left( \frac{\epsilon_0 \gamma m_e}{n_0 e^2} \right)^{1/2}, \quad (2.37)$$

where  $\gamma$  is the time-averaged Lorentz factor in the plasma. The reciprocal of the characteristic response time is called the (electron) plasma frequency  $\omega_{pe}$  and is also the oscillation frequency of the Langmuir oscillation,

$$\omega_{pe} \triangleq \left( \frac{n_0 e^2}{\epsilon_0 \gamma m_e} \right)^{1/2}. \quad (2.38)$$

### Self-focusing effect

The dispersion relation of the laser in the collisionless plasma can be expressed as,

$$\omega_L^2 = \omega_{pe}^2 + c^2 k^2, \quad (2.39)$$

where  $\omega_L$  is the frequency of the laser. Thus, we can calculate the refractive index expression of the plasma as the laser propagates through it,

$$\eta = \sqrt{1 - \frac{\omega_{pe}^2}{\omega_L^2}} = \sqrt{1 - \frac{\omega_{pe}^2}{\omega_{pe}^2 + c^2 k^2}}. \quad (2.40)$$

When  $\omega_L < \omega_{pe}$ , then the wave is an evanescent wave. It means that the laser pulse cannot propagate through the plasma and  $k$  is an imaginary number. The refractive index is also an imaginary number. The laser pulse can propagate through the plasma, when  $\omega_L > \omega_{pe}$ ,  $k$  is a real number. For relativistic intensity, we noticed that  $\omega_{pe}$  is related to laser intensity because it depends on the relativistic  $\gamma$  factor. In the focal plane, the laser intensity distribution exhibits a distribution (in time and space), that is, for a transverse Gaussian distribution the light intensity at the center is stronger than that of the edge. Such a setting then acts like a lens because the refractive index of center is higher than that of edge for relativistically intense pulse. This is the so-called relativistic self-focusing effect which can be exploited to shape the laser pulse.

For  $\omega_L = \omega_{pe}$ ,  $\eta = 0$ , the density of the plasma then equals the critical density,

$$n_{cr} = \frac{m_e \omega_L^2}{4\pi e^2} = 1.1 \times 10^{21} \gamma / \lambda^2 \text{ cm}^{-3}, \quad (2.41)$$

where  $\lambda$  is the wavelength of the laser in unit of  $\mu\text{m}$ . Based on the critical density, the plasma can be classified into a under-dense plasma and over-dense plasma. They play an important role in laser electron acceleration and laser ion acceleration, respectively.

### 2.3.2 Particle motion in relativistic electromagnetic field

In a low-intensity light field, electrons can scatter light without changing the radiation frequency, and the magnetic field component of the light plays a minor role. However, if the light intensity is very high ( $\geq 10^{18} \text{ W/cm}^2$ ), the electrons will oscillate with velocities close to the speed of light. In this relativistic regime, the effects of magnetic and electric fields on electron motion should be comparable and the effective electron mass will increase. The electrons in such a high field move in a figure-eight pattern [81].

The full Lorentz force can be used to describe the motion of particles in a relativistic electromagnetic field,

$$\frac{d}{dt}(\gamma m \vec{V}) = e(\vec{E} + \vec{v} \times \vec{B}) \quad (2.42)$$

where  $\gamma = (1 - v^2/c^2)^{1/2}$  is the Lorentz factor and  $m$  refers to the rest electron mass.  $\vec{E}$  and  $\vec{B}$  are given by the following equations,

$$\vec{E} = -\frac{\partial \vec{A}}{\partial t} \quad \vec{B} = \nabla \times \vec{A}. \quad (2.43)$$

Assume that a monochromatic plane-polarized electromagnetic wave propagates in the x direction, then we obtain  $\vec{E} = (0, E, 0)$  and  $\vec{B} = (0, 0, B)$ . For linear polarisation the vector potential can be described as  $\vec{A} = (0, a(\tau)\cos\omega\tau, 0)$ , where  $a$  is the amplitude of the wave,  $\omega$  is the frequency, and  $\tau = t - x/c$ .

The relativistic Lorentz equations then can be written as [82],

$$\begin{aligned} \frac{d}{dt}(\gamma \dot{x}) &= \frac{eB}{m} \dot{y} = -\frac{e}{mc} \dot{y} \frac{dA}{d\tau} \\ \frac{d}{dt}(\gamma \dot{y}) &= \frac{e}{m}(E - B\dot{x}) = -\frac{e}{mc}(c - \dot{x}) \frac{dA}{d\tau} \\ \frac{d}{dt}(\gamma \dot{z}) &= 0 \\ \frac{d}{dt}(\gamma c) &= \frac{eE}{mc} \dot{y} = -\frac{e}{mc} \dot{y} \frac{dA}{d\tau} \end{aligned} \quad (2.44)$$

Solving the equations above,

$$\begin{aligned} \dot{x} &= \frac{c}{2} a_0^2 \frac{d\tau}{dt} \cos^2 \omega\tau \\ \dot{y} &= -c a_0^2 \frac{d\tau}{dt} \cos^2 \omega\tau \\ \dot{z} &= 0 \end{aligned} \quad (2.45)$$

where  $a_0 = (ea/mc\omega)$ . Averaging  $\dot{x}$  over one period ( $T = 2\pi/\omega$ ) results in,

$$\begin{aligned} \langle \dot{x} \rangle &= \frac{a_0^2}{a_0^2 + 4} c \\ \langle \dot{y} \rangle &= 0 \end{aligned} \quad (2.46)$$

From the solutions 2.45 to 2.46, we can see that the motion of electrons is quiver motion in the plane of the electric field in case of  $a_0 \ll 1$ . When  $a_0 \gg 1$ , the equation 2.46 can be described as  $\dot{x} \rightarrow c$ , which means that electrons reach relativistic velocities through the interaction with the laser pulse.  $a_0 = 1$  defines the relativistic threshold. The corresponding amplitudes of the electric field and magnetic field are given by,

$$E_0 = \frac{3.2 \times 10^{12} a_0}{\lambda[\mu m]} V/m \quad (2.47)$$

$$B_0 = \frac{1.07 \times 10^4 a_0}{\lambda[\mu m]} T \quad (2.48)$$

Then the relativistic intensity can be derived based on the equation 2.1,

$$I_0 = \zeta \frac{1.37 \times 10^{18} a_0^2}{\lambda^2[\mu m^2]} W/cm^2 \quad (2.49)$$

where  $\zeta = 1$  for linear polarization and  $\zeta = 2$  for circular polarization.

In case of circular polarization, the vector potential is,

$$\vec{A} = \left( \frac{1}{\sqrt{2}} a_0 \cos(\phi), \pm \frac{1}{\sqrt{2}} a_0 \sin(\phi), 0 \right) \quad (2.50)$$

Then, the trajectory of the electron becomes,

$$x(\phi) = \frac{1}{\sqrt{2}} a_0 \sin(\phi) \quad (2.51)$$

$$y(\phi) = \mp \frac{1}{\sqrt{2}} a_0 \cos(\phi) \quad (2.52)$$

$$z(\phi) = \frac{a_0^2}{2} \phi \quad (2.53)$$

which is helical.

### 2.3.3 Ponderomotive force in high frequency electromagnetic field

In Section 2.3.2, we talked about the trajectory of electrons in the relativistic electromagnetic field. The force of the particles in the high-frequency electromagnetic field plays an important role in the case of high intensity of the laser pulse. Below, we use the guidance center approximation to derive the expression of the force on the particles by the high-frequency electromagnetic field.

Under the action of an electromagnetic wave, the equation of motion of a particle can be written as,

$$\frac{d^2 \vec{r}}{dt^2} = \frac{q}{m} \vec{E} e^{-i\omega t}, \quad (2.54)$$

where  $\vec{r}$  denotes displacement of a particle,  $q$  signifies the particle charge,  $m$  represents the particle mass,  $\omega$  is the frequency of the electromagnetic wave. The solution of equation 2.54 is,

$$\vec{r}_0 = -\frac{q}{m\omega^2} \vec{E} e^{-i\omega t} \quad (2.55)$$

At this time, we consider the particle motion under the action of spatially inhomogeneous electromagnetic fields,

$$\frac{d^2\vec{r}}{dt^2} = \frac{q}{m}(\vec{E}(\vec{r}) + \frac{d\vec{r}}{dt} \times \vec{B}(\vec{r}))e^{-i\omega t}, \quad (2.56)$$

The motion of the particles can be divided into the sum of the high-speed oscillatory motion and the relatively slow motion at the center of the oscillation,  $\vec{r} = \vec{r}_0 + \vec{r}_1$ . At the same time, the electromagnetic field is expanded at the center of the oscillation, the equation 2.56 can be separated according to the expansion level, and the zero-order term provides the oscillation solution 2.55. The equation of the first term is,

$$\ddot{\vec{r}}_1 = \frac{q}{m} \left[ (\vec{r}_0 \cdot \nabla) \vec{E}|_0 + (\dot{\vec{r}}_1 + \dot{\vec{r}}_0) \times \vec{B} \right] \quad (2.57)$$

Among them, the subscript 0 indicates that the value is taken at the center of the oscillation, and for the sake of brevity, the harmonic factor of time is merged into  $\vec{E}$  and  $\vec{B}$ . Averaging over the oscillatory motion, and due to  $\langle \dot{\vec{r}}_1 \times \vec{B} \rangle = \dot{\vec{r}}_1 \times \langle \vec{B} \rangle$ , yields

$$\ddot{\vec{r}}_1 = \frac{q}{m} \left[ \langle (\vec{r}_0 \cdot \nabla) \vec{E}|_0 \rangle + \langle \dot{\vec{r}}_0 \times \vec{B} \rangle \right] \quad (2.58)$$

Substituting equation 2.55 into equation 2.58,

$$\begin{aligned} \ddot{\vec{r}}_1 &= -\frac{q^2}{m^2\omega^2} \left[ \langle (\vec{E} \cdot \nabla) \vec{E} \rangle + \langle \dot{\vec{E}} \times \vec{B} \rangle \right] \\ &= -\frac{q^2}{m^2\omega^2} \left[ \left\langle \nabla \frac{\vec{E}^2}{2} \right\rangle - \langle \vec{E} \times (\nabla \times \vec{E}) \rangle + \langle \dot{\vec{E}} \times \vec{B} \rangle \right] \\ &= -\frac{q^2}{m^2\omega^2} \left[ \left\langle \nabla \frac{\vec{E}^2}{2} \right\rangle + \left\langle \frac{\partial}{\partial t} (\vec{E} \times \vec{B}) \right\rangle \right] \\ &= -\frac{q^2}{m^2\omega^2} \nabla \frac{\langle \vec{E}^2 \rangle}{2} \triangleq \frac{\vec{f}_p}{m} \end{aligned} \quad (2.59)$$

By definition, we can get the expression of Ponderomotive force on a single particle,

$$\vec{f}_p = -\frac{q^2}{m\omega^2} \nabla \frac{\langle \vec{E}^2 \rangle}{2}. \quad (2.60)$$

Note that since all of the above electric field values are taken at the center of the oscillation, the subscripts are ignored.

The Ponderomotive force is the equivalent force of the non-uniform high-frequency electromagnetic field on the charged particles, and the force of the electromagnetic field pressure (i.e., the gradient of the energy density of the electromagnetic field). Due to the coupling of charged particles to the electromagnetic field, the electromagnetic field pressure can be applied to the charged particles, which is the source of the Ponderomotive force. At high laser intensity and temporal contrast, the Ponderomotive force plays an important role in the interaction of a laser pulse with a plasma.

The so-called Ponderomotive potential  $\Phi_p$  is the cycle-averaged oscillation energy, which is assumed to be a function of the oscillation center position,

$$\Phi_p = \Phi_p(\langle \vec{r} \rangle) = \frac{m}{2} \langle \dot{\vec{r}}_0^2 \rangle = \frac{q^2}{2m\omega^2} \langle \vec{E}^2 \rangle. \quad (2.61)$$

### 2.3.4 Absorption Mechanisms

As mentioned earlier, the plasma can be divided into under-dense plasma and over-dense plasma. The relativistic laser pulse can penetrate through the under-dense plasma and produce a high-speed forward-moving wake-wave during the penetration process due to its ponderomotive force exerted onto the plasma electrons. This charge imbalance imposed by the laser can be exploited for electron acceleration and was originally studied by Tajima and Dawson [83].

For an over-dense plasma, ultra-short relativistic laser pulse can only penetrate into the plasma in the skin layer of thickness  $l_s$  defined by  $l_s = c(\omega_p^2 - \omega_L^2)^{-1/2}$ , where  $\omega_p$  is the plasma frequency and  $\omega_L$  is the laser frequency. The laser interacts with the steep plasma and deposits the energy into a high-density plasma. Of course, a portion of the laser will be reflected by the dense plasma layer. The process of depositing this energy into a high-density plasma is the process by which the plasma absorbs energy and converts it to kinetic energy of (hot) electrons. For different situations, the absorption mechanism can be divided into collision absorption, resonance absorption, vacuum heating and  $J \times B$  heating.

#### Collision absorption

The collision absorption is also called inverse bremsstrahlung, in which the electrons that oscillate in the laser electric field collide and scatter randomly. When electrons collide with ions, they absorb photons, causing an increase in electron energy, which is the opposite of the bremsstrahlung process. The energy increases rapidly after multiple collisions and eventually causes the plasma temperature to rise. The laser field firstly makes the electrons oscillate and then the photons are absorbed by the collisions of the electrons and ions, resulting in the increase of plasma temperature. Therefore, the important parameter is the electron-ion collision frequency [84],

$$\nu_{ei} = 3 \times 10^{-6} \frac{n_e Z}{T_e^{3/2}} \ln \Lambda, \quad (2.62)$$

where  $n_e$  is the electron density in unit of  $cm^{-3}$ ,  $Z$  is the charge of ions,  $\Lambda$  is the ratio of the maximum and minimum impact parameters,  $T_e$  is the electron temperature in unit of eV. It can be seen that when the laser intensity is weaker and the electron temperature is lower, the collision frequency of electrons and ions will rise sharply, resulting in an increase of inverse bremsstrahlung. Typically, when the laser intensity is less than  $10^{14} W/cm^2$ , the collision absorption mechanism plays a leading role. Otherwise, other collision-free absorption mechanisms dominate.

#### Resonance absorption

As mentioned above, the collisions between electrons driven by the laser fields and ions can cause some absorption and may be quite important in allowing a weak precursor of a pulse to ionize the target, but as the intensity increases, the fraction of the light energy absorbed by collisions becomes smaller. The resonance absorption is one of the collisionless absorption mechanisms, by which an inhomogeneous target plasma can absorb a significant fraction ( $\sim 50\%$ ) of obliquely incident laser light with P polarization (electric vector parallel to the plane of incidence). And

based on the length of the resonance zone, the resonance absorption can be divided into linear or nonlinear resonance absorption [85].

Since the experimental observation of absorption occurring at a specific angle, Godwin constructed a simple optical model to explain this phenomenon [86]. Starting from basic optics principles, he derived the absorption coefficient of the obliquely incident light wave after passing through an under-dense plasma layer and then returned to the vacuum after being reflected on the surface of the over-dense plasma. Through maximizing the expression of the absorption coefficient, the best case needs to satisfy the equation  $2\pi d/\lambda = \epsilon_2/\sin\theta \tan\theta$ . The equation shows that the optimal thickness of the under-dense plasma layer  $d$  is determined by the laser wavelength  $\lambda$ , the angle of incidence  $\theta$ , and the imaginary part of the dielectric constant  $\epsilon_2$ .

Subsequently, to describe resonant absorption in a hot plasma, Forslund et al. [87]. combined the linearized electron-momentum equation with Maxwell's equations and found an accurate conversion rate as a function of density scale length  $L$  (from zero to critical density) and angle of incidence  $\theta$  numerically. Highest absorption occurs at  $(k_0 L)^{2/3} \sin^2\theta \approx 0.5$ , where  $k_0$  denotes the incident free-space wave number.

Resonance absorption is a very effective electron heating mechanism when the plasma density gradient is not too large. In a non-uniform plasma, an obliquely incident P polarized laser near the critical surface of the plasma, through the tunneling effect, will resonate with a strong electron plasma wave in the direction of the plasma density gradient. Waves are converted into electron energy, producing superheated electrons with high kinetic energy. This mechanism can cause large amounts of laser energy to be absorbed in large-scale plasmas. However, it is also important in the case where the plasma scale is smaller than the laser wavelength [85].

Other explanations such as the so-called capacitor model, can be found in references [88] and [89]. For nonlinear resonance absorption, one can refer to the textbook [85].

### Vacuum heating

In 1983, Bach et al. measured the intensity dependence of the absorption coefficient of a  $10\ \mu\text{m}$  laser obliquely incident on gold sphere targets [90]. They found that when the light intensity is  $10^{14}\ \text{W}/\text{cm}^2$ , the absorption coefficient is 25% – 30%, and when the light intensity is increased to  $10^{16}\ \text{W}/\text{cm}^2$ , the absorption coefficient increases to 50% – 60%. The absorption theory at that time was mainly Inverse Bremsstrahlung Absorption or Resonance Absorption. After discussion, they attributed this phenomenon to an enhanced resonance absorption mechanism. The reason for the enhancement is that the surface roughness of the critical surface is greater under higher light intensity. Numerical simulation results showed that the roughness of the critical surface is about 4 microns at  $2 \times 10^{15}\ \text{W}/\text{cm}^2$ . This result inspired Brunel to develop a completely new theory: the vacuum heating mechanism [91].

In short, the vacuum heating mechanism means that when a strong laser is obliquely incident on a metal surface or a steep over-dense plasma, electrons are pulled into the vacuum by the laser electric field and pushed back as the electric field is reversed. During this process, the electrons acquire the velocity  $v \approx v_{osc} = eE_0/m_e\omega$  and transfer energy to the plasma by collision

afterwards, while the roughness of the critical surface changes which echoes the results of previous numerical simulations. Here,  $v_{osc}$  is quiver velocity due to the electric field  $E_0$  normal to the interface,  $e$  is charge of electron and  $m_e$  is electron mass.

In order to describe the energy absorption mechanism, Brunel used a 1D capacitor model [91] to calculate the absorbed energy per cycle as,

$$W_{abs} = \frac{1}{2}\eta N m_e v_{osc}^2, \quad (2.63)$$

where  $N = E_0/4\pi e$  is the maximum number of electrons drawn into the vacuum per cycle, and  $\eta = 1.75(1 + 2v_T/v_{osc})$ . Here,  $v_T$  is the the electron thermal velocity. Since the incident power is given by  $I_{in} = c(E_L^2/8\pi)\cos\theta$ ,  $E_L$  being the laser field, the ratio  $f$  of the absorbed power can be given,

$$f = (\eta/2\pi)(v_{osc}^3/cv_L^2\cos\theta). \quad (2.64)$$

Here,  $v_L = eE_L/m_e\omega$ . Due to the imperfect reflection and relativistic corrections, the absorption ratio is finally given by,

$$f^* = (\eta/\pi)cv_{osc}[(1 + v_{osc}^2)^{1/2} - 1]/(v_L^2c\cos\theta). \quad (2.65)$$

Compared to the experimental result in reference [90], the vacuum heating mechanism can successfully explain the intensity dependence of the energy absorption for  $I \geq 4 \times 10^{14} \text{ W/cm}^2$ . In summary, when the density gradient length is greater than the excursion of the electron, i.e., an under-dense corona is present the resonance absorption dominates. In the absence of corona, the vacuum heating mechanism dominates, under which the absorption coefficient increases with laser intensity.

### **$\mathbf{J} \times \mathbf{B}$ heating**

Both the resonance absorption and the vacuum heating discussed above are based on the electric field component perpendicular to the plasma surface, which requires the laser to have p-polarization and oblique incidence. In addition, when the light intensity is sufficiently strong ( $I\lambda^2 \geq 10^{18} \text{ W}\mu\text{m}^2/\text{cm}^2$ ), the longitudinal Lorentz force received by the transversely oscillating electrons can also directly heat the hot electrons, so the heating mechanism is not limited by polarization and can act under normal incidence. This is called  $\mathbf{J} \times \mathbf{B}$  (or  $\mathbf{v} \times \mathbf{B}$ ) heating [92], proposed by Kruer and Estabrook.

Considering a linearly polarized laser with electric field amplitude  $E = E_L(x)(\sin\omega t)\hat{y}$ ,  $E_L$  being laser field and  $\omega$  is laser frequency. Using the ponderomotive force expression 2.60, and neglecting thermal and relativistic effects, we can obtain,

$$\begin{aligned} f_p &= -\frac{e^2}{m\omega^2} \nabla \cdot \frac{\langle E^2 \rangle}{2} \\ &= -\frac{m}{4} \frac{\partial}{\partial x} v_L^2(x)(1 - \cos 2\omega t)\hat{x} \\ &= -\frac{m}{4} \frac{\partial}{\partial x} v_L^2(x)\hat{x} + \frac{m}{4} \frac{\partial}{\partial x} v_L^2(x)\cos 2\omega t\hat{x} \end{aligned} \quad (2.66)$$

where  $v_L = eE_L/m\omega$ . In the equation 2.66, the first part is the usual DC ponderomotive force and accelerates electrons and steepens the density profile, which may lead to a hole several wavelengths deep through moderately overdense plasma [93]. The second part corresponds to an electrostatic field  $E^*$  heating the electrons as,

$$eE^*/m = \frac{1}{4} \frac{\partial}{\partial x} v_L^2(x) \cos 2\omega t. \quad (2.67)$$

According to the source, we know that ponderomotive force is derived from Lorentz force, so we can think that  $\mathbf{J} \times \mathbf{B}$  heating is caused by the magnetic effect. This heating mechanism changes the laser electric field driving force to the electrostatic field driving force of the oscillating component of the ponderomotive force compared to the resonance absorption and the vacuum heating. One can expect that the main difference is that the driving force has a different frequency of  $2\omega$  instead of  $\omega$ . And due to the scale of  $v_L^2 \propto E_L^2$ ,  $\mathbf{J} \times \mathbf{B}$  heating scales as  $a_0^2$ , where  $a_0 = eE_L/cm_e\omega$ .

### 2.3.5 Laser ion acceleration mechanisms

In order to explore effective improvements of laser ion acceleration in plasmas established acceleration mechanisms must be reviewed. Those are Target Normal Sheath Acceleration (TNSA), Radiation Pressure Acceleration (RPA), Coulomb Explosion (CE), and volumetric acceleration in the relativistically induced transparency regime (such as the break out afterburner, BOA). It should be noted that at currently accessible laser intensities the laser pulse does not directly accelerate the ions. Instead, the acceleration happens via fields that are mediated via the laser-driven electrons. We will concentrate on TNSA and RPA, as those are most relevant for the experimental studies presented in this thesis.

#### Target Normal Sheath Acceleration

A relativistic laser pulse is normally or obliquely incident on a over-dense solid target. Based on the absorption mechanisms 2.3.4 previously described, the absorbed laser energy is transferred to the electrons, which partly pass through the target and form a high-temperature, high-density electron leaks out at the rear surface of the target. When passing the target-vacuum boundary, a sheath electric field is formed whose strength can reach the order of  $TV/m$ . This sheath electric field can ionize the atoms and accelerate the ions on the surface of the target over distances of micrometer to kinetic energy of (multi-)  $MeV$ . Since the electrons spread transversely over a circular area, the electrons that slant through the target will travel more distances and reach the back of the target later than electrons that pass directly (on the shortest path) through the target [32]. That will cause the electron layer expanding into the vacuum to have a certain curvature. The sheath electric field is predominantly normal to the target surface but has a certain transverse component such that the accelerated ions are also accelerated into target normal direction while having a certain angular divergence. [52].

In 1975, Crow et al. found that the ion front can be accelerated to velocities comparable to the thermal velocity of the electrons by establishing a model of collision-free expansion of a semi-

infinite plasma into a vacuum [8]. Under the ad-hoc assumption of Boltzmann equilibrium of electrons, a linear electrostatic potential with self-consistent modification can lead to half the electron density depletion in logarithmic units [94]. In order to obtain accurate solutions for the structure of the ion front, the resultant ion energy spectrum, and the maximum ion energy, Mora developed this model further [30]. The initial condition of the model is that the plasma occupies half of the space ( $x < 0$ ) and has a steep plasma-vacuum interface at the junction. The ions in the plasma are evenly distributed ( $n_i = n_{i0}$ ), unheated and in a stationary state; the electron density satisfies the Boltzmann distribution,

$$n_e = n_{e0} \exp(q_e \Phi / T_e), \quad (2.68)$$

where  $q_e$  is the electron charge,  $n_i$  and  $n_e$  are the electron density and ion density, subscript 0 denotes at time 0, and  $T_e$  is the electron temperature, respectively. The electrostatic potential  $\Phi$  follows Poisson equation,

$$\frac{\partial^2 \Phi}{\partial x^2} = \frac{q_e}{\epsilon_0} (n_e - Z_i n_i), \quad (2.69)$$

where  $Z_i$  is ion charge and  $\epsilon_0$  is permittivity of vacuum. The ions start to expand into the vacuum at  $t > 0$ , which can be described with continuity and force equations,

$$\frac{\partial Z_i q_e n_i}{\partial t} + \nabla \cdot (Z_i q_e n_i v_i) = 0, \quad (2.70)$$

$$\left( \frac{\partial}{\partial t} + v_i \frac{\partial}{\partial x} \right) v_i + (Z_i q_e / m_i) \frac{\partial \Phi}{\partial x} = 0, \quad (2.71)$$

where  $v_i$  is the ion velocity. The boundary condition at the ion front can be obtained by integrating the Poisson equation from  $x = x_{front}$  to  $x = \infty$ , yielding the accelerating field

$$E_{acc} = \sqrt{2} k_B T_e / q_e \lambda_D, \quad (2.72)$$

where  $k_B$  is Boltzmann constant,  $\lambda_D = \lambda_{D0} \exp[(1 + x/c_s t)/2]$  is the local Debye length,  $\lambda_{D0} = (\epsilon_0 k_B T_e / n_{e0} q_e^2)$  being the initial Debye length and  $c_s = (Z_i k_B T_e / m_i)^{1/2}$  being the ion sound velocity. Then the evolution of the electric field at the ion front can be solved as a function of time,

$$E_{acc} \simeq 2E_0 / (2e_N + \omega_{pi}^2 t^2)^{1/2}, \quad (2.73)$$

where  $e_N = 2.71$  denotes the numerical constant,  $\omega_{pi} = (n_{e0} Z_i q_e^2 / m_i \epsilon_0)$  is the ion plasma frequency and  $E_0 = (n_{e0} k_B T_e / \epsilon_0)^{1/2}$ . And the ion front velocity and position can be obtained by integrating  $dv_{front}/dt = Z_i q_e E_{front} / m_i$  and  $dx_{front}/dt = v_{front}$ ,

$$v_{front} = 2c_s \ln(\tau + \sqrt{\tau^2 + 1}), \quad (2.74)$$

$$x_{front} = 2\sqrt{2e_N} \lambda_{D0} [\tau \ln(\tau + \sqrt{\tau^2 + 1}) - \sqrt{\tau^2 + 1} + 1], \quad (2.75)$$

where  $\tau = \omega_{pi} t / \sqrt{2e_N}$ . The analytical results of electron density at ion front can be derived in the asymptotic limit ( $\omega_{pi} \gg 1$ ), and then the solution of ion density at ion front can also be obtained. The spatial derivatives of the electron and ion densities at the ion front can be used

to deduce the energy spectrum of the electrons and ions. Here, based on the spatial derivative of electron density, the acceleration field at the ion front can be rewritten as,

$$E_{acc} \simeq \frac{2k_B T_e}{q_e c_s t} \quad (2.76)$$

The number of ions per unit energy and unit surface based on this model is given by,

$$dN/d\mathcal{E} = (n_{i0} c_s t / \sqrt{2\mathcal{E}\mathcal{E}_0}) \exp(-\sqrt{2\mathcal{E}/\mathcal{E}_0}), \quad (2.77)$$

where  $\mathcal{E}_0 = Z_i k_B T_e$ . The cutoff energy  $\mathcal{E}_{max}$  can be deduced from equation 2.74 in case of asymptotic limit,

$$\mathcal{E}_{max} \simeq 2\mathcal{E}_0 [\ln(2\tau)]^2. \quad (2.78)$$

This model describes the TNSA mechanism in a way of plasma expansion. However, the model is based on a uniform distribution of the plasma in the half space, and the actual target has a certain thickness, so Mora also pushed the model to the regime of thin-foil expansion into a vacuum [95]. From equations 2.72 and 2.76, we see that the acceleration field  $E_{acc}$  varies with electron temperature and decreases with time or scale length. From equation 2.77 and 2.78, the cutoff energy increases with time, while the number of ions decays exponentially towards higher energies. For a given laser intensity, the temperature of the electrons can be estimated to be equal to the ponderomotive potential,

$$k_B T_e = \Phi_p = m_e c^2 (\sqrt{1 + a_0^2} - 1), \quad (2.79)$$

where  $a_0$  is the normalized amplitude of the laser field. If the pulse length is sufficient to sustain this field to the end of the acceleration, the ion velocity coming from the sweeping potential can be given by [96],

$$v_i = c \sqrt{\frac{2m_e}{m_i} \left(1 + \frac{I\lambda^2}{1.37 \times 10^{18}}\right)^{1/2} - 1}. \quad (2.80)$$

Otherwise, when the pulse length is shorter than the maximum acceleration time, the ion energy cannot reach the maximum velocity. Here, the maximum acceleration time can be calculated by ion motion equation based on the sweeping length closed to the local plasma Debye length. The problem with this model is that it suggests that the acceleration of ions continues indefinitely. Fuchs et al. [23] have therefore truncated the acceleration by fixing the acceleration time to the laser pulse duration times 1.3.

A developed quasi-static theoretical model [97] for TNSA mechanism was proposed to circumvent this problem. Hot electrons create a non-neutral region on the back surface of the target. The target consists of heavier ions, while the light ions in the impurities form a thin layer behind the non-neutral region. During the characteristic acceleration time of light ions, the hot electrons are almost isothermal, and the heavier ions are almost immobile. Until the amount of accelerated light ions is much lower than the amount of hot electrons, the field is not strongly affected. Under this assumption, an analytical solution was also obtained, and the pulse energy and intensity plane can be used to predict the maximum ion energy under satisfactory conditions of the laser system. For example, a possible path to reach 250 MeV protons and 10 nA current with TNSA mechanism as follows, laser energy  $E_L = 50 J$ ; wavelength  $\lambda = 800 nm$ ; intensity  $I = 1 \times 10^{22} W/cm^2$ .

Regardless of the actual model and laser parameters, target thickness is one most important parameter to optimize in TNSA for maximizing the ion energy [53, 98, 99]. The interpretation of the effect of target thickness on acceleration is manifold, but one interesting interpretation is that the recirculation of hot electrons within the target can cause higher hot electron densities or higher energies of the hot electrons that induce the accelerating field for the ions. This is important to keep in mind when discussing the enhancement effect.

### Radiation Pressure Acceleration

Radiation Pressure Acceleration (RPA) ion (or rather plasma) bunches with small energy spread, large bunch density enables high energy conversion efficiency. In particular, the generation of hot electrons, i.e. electrons with a large energy spread, should be avoided such that plasma expansion (or more specific TNSA) is actually suppressed. This can be enforced by using circularly polarized pulses at normal incidence [100, 101]. In addition, RPA requires high temporal contrast pulses so that ultra-thin (several nm) targets can be used. First hints that RPA is indeed effective have been confirmed by experiment [56].

The physical image of the RPA mechanism is as follows. A super-intense laser is incident on the ultra-thin target. The radiation pressure of the laser, i.e. the  $\mathbf{v} \times \mathbf{B}$  force pushes electrons on the front surface of the target to form a high-density electronic compression layer and a depletion layer. Under the action of the strong electrostatic field, ions are dragged along and catch up with the electrons [102]. Next, the electrons and ions form a sort of a microscopic mirror that is pushed further by the radiation pressure [103]. A strikingly different feature of this physical image from TNSA is that ion acceleration starts on the front surface of the target, and laser light pressure dominates throughout the process. As a result, the ion spectrum manifests peak rather than a monotonic decay. An ideal RPA mechanism at constant laser intensity could produce a mono-energetic ion beam. In reality, since the foil is unevenly illuminated in the lateral dimension and dynamically evolves during the interaction with the pulse, it rapidly deforms and eventually becomes transparent, resulting in lateral heating of the electrons. Therefore, in today's experiments this ideal RPA has not been achieved yet and limitations due to lateral Rayleigh-Taylor-like or Weibel instabilities were observed [104, 105].

Based on the physical image, one can derive the ion maximum energy using the model of a flat foil driven by the radiation pressure [106], which is the flow of delivered momentum per unit surface and depends on the reflectance of the foil. Assume a plane, monochromatic wave of intensity  $I$  and frequency  $\omega_L$  normally incident on a foil target,  $R$  and  $T$  being the reflection and transmission coefficients of the foil, respectively. Then, the frequency of reflecting light can be represented as  $\omega_R = \frac{1-\beta}{1+\beta}\omega_L$  due to the Doppler effect, where  $\beta = v/c$  is the normalized velocity of the electrons [107]. It can be seen that as the target speed increases, the energy of the reflected photons decreases, and the laser transfers almost all of the energy to the target once it moves with velocities close to  $c$ . At the same time, due to the overall acceleration of the target, the moving speed of ions and electrons is equal, and the ion mass is much larger than the electron mass. Therefore, the main energy of the laser is transferred to ion kinetic energy, and the corresponding energy conversion efficiency will be greatly improved. The radiation pressure

on a foil with relativistic velocity  $\beta$  can be given by,

$$P_{rad} = \frac{1 - \beta}{1 + \beta}(1 + R - T)I/c = 2R(I/c)\frac{1 - \beta}{1 + \beta} \quad (2.81)$$

in case of negligible absorption. At the intensity beyond  $10^{23} \text{ W/cm}^2$ , RPA mechanism is expected to exceed TNSA. Assuming that the foil target remains perfectly intact during acceleration, the one-dimensional equation of motion of the target is [106],

$$\frac{dp}{dt} = R^2 \frac{[E_L(t)]^2}{2\pi n_i d} \frac{\sqrt{m_i^2 c^2 + p^2} - p}{\sqrt{m_i^2 c^2 + p^2} + p}, \quad (2.82)$$

where  $p$  is the momentum of ions,  $E_L(t) = E_0(t - x(t)/c)$  is the laser electric field at location  $x(t)$ ,  $n_i$  is the ion density,  $m_i$  is the ion mass and  $d$  is the target thickness. In case of constant electric field and  $R = 1$ , the maximum ion kinetic energy can be given as [106],

$$E_{max} \approx m_i c^2 \left[ \left( \frac{3E_0^2 t}{8\pi n_e d m_i c} \right)^{1/3} \right]. \quad (2.83)$$

If the laser energy is  $W$  within a finite acceleration time, such as within a finite pulse width, the final energy of the ion is,

$$E_{max} = 2m_i c^2 \frac{(\mu S N)^2}{1 + 2\mu S N}, \quad (2.84)$$

where  $\mu = \frac{m_e Z}{m_i}$ ,  $S = \frac{a_0^2}{\sigma}$ ,  $a_0$  being the normalized amplitude of the laser field,  $\sigma = \frac{n_e d}{n_c r \lambda}$  being the normalized area density.

In hole boring RPA regime, as soon as the laser is turned on, the ions are accelerated continuously by repeating the hole boring process until all adjacent ions are reflected by the hole boring front at the same velocity, or in other words, until the compression layer reaches the initial back surface of the target. In non-relativistic regime, the maximum ion kinetic energy can be given as [102],

$$E_{max} \approx m_i c^2 \frac{2I}{m_i n_i c^3} = 2m_i c^2 \frac{Z n_c m_e a_0^2}{A n_e m_i}. \quad (2.85)$$

After the entire target begins to move, the acceleration becomes another phase called the light sail (LS) acceleration [103]. It can be viewed as a multi-level acceleration of the entire target, as a plasma plate, reaching almost the same maximum speed as through radiating pressure. The maximum ion kinetic energy in this case can be given as [108],

$$E_{max} = m_i c^2 \left( \frac{2RE_L}{Mc^2} \right)^2, \quad (2.86)$$

where  $M$  is target mass. Using  $M = \sigma S d$ , one can see that 2.84 is the same as 2.86

We note that in the literature, the RPA mechanism has been named in various ways. The hole boring scheme is generally discussed in the context of electrostatic shock acceleration. The term laser piston can be used for RPA of both thin foil [106] and thick targets [109]. The specific conditions or characteristics of the Light Sail scheme are described as phase stable acceleration [17]. It can be seen that regardless of the model, the maximum energy of the ions is proportional

to the light intensity, which is different from the 1/2 power in the TNSA mechanism. It is concluded that the laser energy conversion rate of the RPA mechanism is greatly improved. In essence, RPA means that a laser pulse with sufficient intensity can interact directly with ions (protons), which requires laser intensity beyond  $I = 4.6 \times 10^{24} \text{ W/cm}^2 \times (1 \mu\text{m}/\lambda)^2$ , corresponding to the dimensionless amplitude  $a_0 = m_p/m_e = 1836$ ,  $m_p$  being the proton mass. However, due to the collective effects in a plasma, protons can also gain relativistic energies at significantly smaller intensity.

In experiments, it is very difficult to achieve stable RPA ion acceleration. On the one hand, it requires a suitable target thickness, usually a few nanometers to micrometers depending on target density and laser intensity. On the other hand, one must minimize or better avoid heating of the electrons. Because the circularly polarized laser (without the oscillation term) can suppress electron heating, the harsh conditions of the RPA mechanism can be reduced. However, the inherent prepulse platform of the laser pulse can trigger a pre-plasma that pre-expands the target before the main laser arrives. Today, RPA studies usually require plasma mirrors [56]. As ideal RPA will require even higher (by a factor of 100) intensities, this contrast challenge will likely continue to determine the exploitability of RPA on the midterm.

## 2.4 Numerical simulation methods for laser-plasma interaction

Because the factors affecting the results of experimental investigations are manifold, it is very difficult to interpret data and identify the optimal experimental conditions. Therefore, the construction of theoretical physics models can help to understand the various effects of laser-material interaction and provide clear physical images and rationals. Prime examples for complicated physics are the various heating and acceleration mechanisms discussed in the previous sections ( see 2.3.4 and 2.3.5). The laser absorption mechanism affects the ion acceleration mechanism significantly the complexity of the physical process leads to the inability to establish a unified model to explain all experimental phenomena in a single model.

Numerical simulation studies are very important and complementary to experimental studies, and parameter settings and result output are stable and repeatable. Even though they rely mostly on perfect laser pulses and target parameters, they can shed light onto the processes involved, allow for separating individual effects and thus can give prediction and guidance. In particular, numerical simulation can offer insights into fast processes that are hard or impossible to visualize in experiments. However, numerical simulation are only as good as the physics model that is incorporated and will ultimately need to be verified experimentally.

Modeling of plasmas is based on the numerical solution of the Vlasov (or more complicated versions of it) equation along with models for electromagnetic radiation (in particular the Maxwell equations). Typically there are three classes of approaches, the static, the fluid or hydrodynamic and the kinetic models.

The first method treats the plasma as a passive medium, which is produced by ionization or as the laser propagates through it. This description is particularly applicable to very low density systems where the plasma period is longer compared to the interaction time. The feedback of the low-density plasma to the laser is mainly manifested by changing its refractive index, such

as a self-focusing effect. Numerical methods based on static plasma models include molecular dynamics simulation methods and Monte Carlo methods.

The second method (fluid or hydrodynamic model) assumes that the plasma is at least partially in thermal equilibrium, i.e. its particle distribution function is Maxwellian with well-defined electron temperature and ion temperature. Under these conditions, the plasma state can be described by its macroscopic physical quantities: density, pressure, average fluid velocity field, etc. Popular fluid model numerical simulation methods are Hydrodynamics, MHD and steady state.

The third method (kinetic model) attempts to self-determine the particle distribution without assuming that all distributions are Maxwellian (e.g. they allow for wave-breaking or particle-trapping). The kinetic simulation is divided into two categories, one considering binary collisions, that is, based on the solving the Fokker-Planck equations. The other type ignores collisions between particles, i.e. based on solving the Vlasov equations [110]. The plasma particle simulation method, i.e. Particle-in-Cell (PIC) simulation, which often ignores particle collisions, is gradually adopted by more and more researchers due to its advantage of computational effort and the mature numerical method (solving simple particle motion equation). In its most basic form, dynamics simulation involves solving the N-body problem of a large number of electrons and ions that represent small volumes in the phase space. For example, a solid density plasma has about  $10^{23}$  electrons  $/cm^3$ . To describe laser interactions with a focal spot diameter of  $10\mu m$  and a penetration depth of  $2\mu m$ , we would need to simulate more than  $150\mu m^3$  of volume or  $10^{19}$  particles at this density. Instead, typically  $1 \times 10^8$  macro particles are simulated, each of them represents a certain volume element (that may contain a large number of particles).

This way, the PIC simulation method sheds light onto the collective characteristics of large scale ( $> \lambda_D$ ), that is, in a small scale ( $< \lambda_D$ ) around a point in the phase space, the contribution of each charged particle to the electromagnetic field and the effect of the electromagnetic field on adjacent particles out of this small scale are considered to be the same. On this basis, it is feasible to select a macro-particle to represent all charged particles in a small volume (such as,  $(\frac{\lambda_D}{10})^3$ ) of the phase space. For a plasma with  $\lambda_D = 100 nm$  and number density of particles of  $10^{23}/cm^3$ , a macro-particle can represent the collective behavior of  $10^5$  real particles, which greatly reduces the number of particles of the simulation. It must be noted though, that this representation has severe limits when considering, for example, generated radiation (which per definition is emitted by many perfectly coherently moving individual particles). For the details about the algorithm of PIC simulation, one can refer to the book [74].

## Chapter 3

# Experimental background and Facilities

This chapter focuses on the laser infrastructures and ion detection instruments involved in the following experiments. The high-repetition experiment in Chapter 4 was based on ATLAS (Advanced Ti: sapphire LASer) 300 at Laboratory for Extreme Photonics (LEX Photonics) of the Ludwig-Maximilians-Universitt (LMU) and the ion detector used was a compact wide-angle spectrometer (WASP). The optical thin film target manipulation experiment was carried out at Peking University, using the CLAPA (Compact LASer Plasma Accelerator) 200 TW laser facility, and the Thomson parabola spectrometer was used for detecting ions.

### 3.1 High power laser facilities

Periodic trains of ultrashort light pulses, with duration less than 1 ps, can be generated using mode-locking techniques in laser cavities employing active [111] or passive [112] mode locking. In some types of lasers (i.e. Ti: sapphire laser), the modes may lock spontaneously without any need for an external modulation (active) or through a saturable absorbing medium (passive). Kerr lens effect is often employed to modelock Ti:Sa laser oscillators. The self-modulation of the phase broadens the spectrum of the wave and therefore shortens its duration. Further improvements of the above mode-locking can generate even shorter pulses in tens or sub-10-fs range using chirped mirrors [113] or semiconductor saturable absorber mirrors [114]. In the field of competition to shorten the pulse width, recent developments in the generation of tabletop X-ray lasers have paved a way to dynamical studies in attosecond regime [115]. From this point of view, the technology for compressing the pulse width of laser pulses is mature.

However, direct amplification of ultrashort pulse is limited to the damage threshold of the gain medium and all of the reflective and transmissive optics in the beam path. On the other hand, the propagation of high-intensity pulses in a medium will cause a series of nonlinear effects which include the spatial and temporal phase distortions by self-phase modulation, self-focusing (like Kerr lens) or filamentation [116]. Therefore, before the invention of CPA technology [1], the

intensity of ultrashort pulses was limited to below  $10^{16} \text{ W/cm}^2$ . With the development of CPA technology, the above problems were overcome and the peak power of the state of art ultrashort pulse rapidly reached several Petawatt [117].

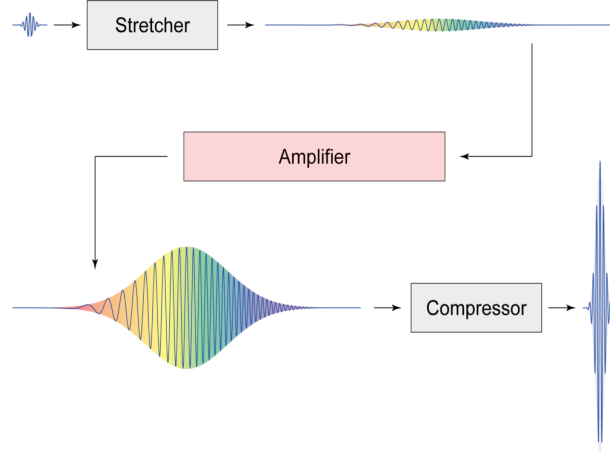


**Figure 3.1:** Concept of the chirped pulse amplification (CPA) scheme. First, the initial pulse is stretched in time and then amplified to high power. During amplification, the beam diameter is increased. After the last amplification stage, the laser pulse is re-compressed to generate a high peak power pulse.

Specifically, The idea of CPA technology is to artificially stretch the pulse in the time domain, then amplify the pulse and recompress it back to the smallest possible pulse duration (Figure 3.1). Before the main amplifier, the seed laser pulse is stretched by a device introducing Group-Delay Dispersion (GDD) and the different wavelength components are shifted in time so that chirped pulse is obtained. The GDD device is called stretcher and typically composed of a pair of diffraction gratings, prisms or the combination of both. Typically, the pulse duration can be stretched by a factor of  $10^5$  and thus much higher energy can be stored in the long pulse after the amplifier. In the end, the pulse of wavelength components is recompressed in time by another GDD device (basically inverting the effect of the stretcher), which is called compression. Thus, the whole procedure minimizes the aforementioned non-linear effects and damage of the optics in the beam path during amplification.

### 3.1.1 ATLAS 300 laser facility

ATLAS 300 delivered 300 TW peak power with 5 Hz repetition rate and was operated in LEX photonics from 2014 to 2016 as a test phase for the Center for Advanced Laser Application (CALA). The laser device is named as ATLAS 300 due to the Ti: sapphire technology and laser power of nearly 300 TW, whose main parameters are as follows, laser energy 6 J, pulse width 25 fs, center wavelength 800 nm.

Figure 3.2 shows the layout of the ATLAS 300 laser system is plotted in the manner of water flow. It utilizes Ti: Sapphire crystals as gain media and is based on the CPA technology. In the front end, A Femtolaser Synergy oscillator is used to produce ultrashort pulses with an average energy of 5 nJ and a FWHM bandwidth of 100 nm at 70 MHz repetition rate, which is based on Kerr lens mode locking [118]. After the oscillator, a pockels cell is placed to select pulses at a rate

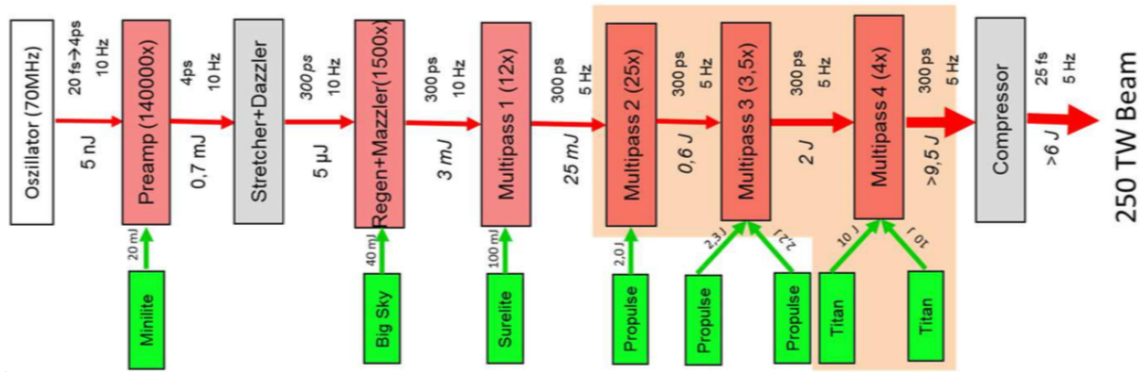


**Figure 3.2:** Schematic Layout of the ATLAS 300 at LEX Photonics. Courtesy of B. Günther and H. Ding.

of 10Hz for further amplification and to suppress the residual pulses before they are amplified. Additionally, the temporal contrast is increased by chopping the pulse pedestal at an ns-time scale. Then, the pulses are stretched from 20 fs to 4 ps by a SF-14 glass block. A nine-pass pre-amplifier (Minilite) with a plane folding mirror and two concave mirrors is designed for focusing the pulse onto the Ti: Sa crystal and collimating it to achieve 0.7 mJ with a gain factor of about 140000. The gain in the preamplifier is positively correlated to intensity, so the temporal contrast will be also enhanced after that. In the next step, in order to minimize spectral clipping, high order dispersion and spectral phase distortion, a compact solution of an all-reflective telescope (so-called Öffner-triplet) is used in the stretcher. The stretcher module consists of a grating and two concentric spherical mirrors (one is concave and the other is convex), which only allows astigmatism and spherical aberration to emerge due to the complete symmetry. However, there is no ideal solution to avoid high-order dispersion and spectral phase distortion completely, which reduces the temporal contrast. Therefore, the Dazzler, an commercial accusto-optical programmable dispersive filter (AOPDF) [119] from Fastlite is introduced to correct higher order dispersion and phase distortion for optimum pulse compression. In addition, it can also shape pulses by modulating the amplitude of the applied signal [120]. Afterwards, the stretched pulses are sent to a regenerative amplifier consisting of three parts, a Z-shaped resonator compensating coma, a Mazzler (accusto-optical programmable gain control filter), a pulse cleaning unit. The Mazzler can compensate for gain narrowing [121] and also pre-compensate for spectral red-shift in the following amplifier stages. In the Regen-cavity, the amplified spontaneous emission significantly reduces the temporal contrast, and then a pulse cleaner Pockels cell is installed to remove it. Polarization can also be cleaned by combining stacked thin film polarizers. The output pulse has good spatial and polarization characteristics, but at 300  $\mu\text{J}$  lacks sufficient energy due to the loss in the Mazzler. After a four pass amplifier, the energy of the pulse is pushed to about 3 mJ at the exit of the regenerative amplifier unit. The last part of the front end are another four pass amplifier and two pockels cells. The repetition rate is reduced to 5 Hz by a pockels cell and the final energy of the pulse after the front end is about 25 mJ. And additional pockels cell installed subsequently with 200 ps rise time enhances the temporal contrast by chopping the ASE at this time scale.

After the front-end spectral and spatial beam shaping, the pulses are passed to the back end for step-by-step amplification. In the amplifier chain, a Faraday rotator in combination with a polarizer and a quarter wave plate are set up to prevent the front end from severe damage

in case of pulse back-reflection. After each amplifier, a spatial filter is built into the beam line to clean the beam profile from spatial wavefront distortions. Since the pump profile in a gain-saturated amplifier will be imprinted on the amplified seed profile, an integrating mirror is used for shaping the pump beam to obtain a homogeneous pump beam profile. In the crystals, a large amount of heat is stored and the multipass amplifier design will increase the thermal lens effect after multiple travels. Accordingly, the incoming beam can be divergent to compensate for this effect. In addition, the thermal conductivity of Ti: sapphire crystals increases with increasing temperature, so efficient water cooling helps to reduce the thermal effects of the crystal. The spontaneous emission from the Ti:Sa crystal results in a transverse lasing which is overcome by coating with an absorber on the edges. All in all at the exit of the final amplifier, saturated energy of 9.5 J with a bandwidth large enough for <30 fs pulses is delivered. Directly after the telescope, the beam is sent into a vacuum chamber, where the compressor realized with four parallel gratings enables the right path difference to reverse the dispersion accumulated in the stretcher and other materials. Additionally, a Dazzler-Wizzler-loop is used to obtain the minimum pulse duration, where Wizzler uses self-referential spectral interferometry to analyze the compression pulse and calculate the modified input signal of Dazzler. Considering a transmission of about 70% for the compressor, an energy of > 6 J can be expected after compression, and the peak intensity of 250 TW for the pulse duration of 25 fs is feasible.

### 3.1.2 CLAPA 200 TW laser facility

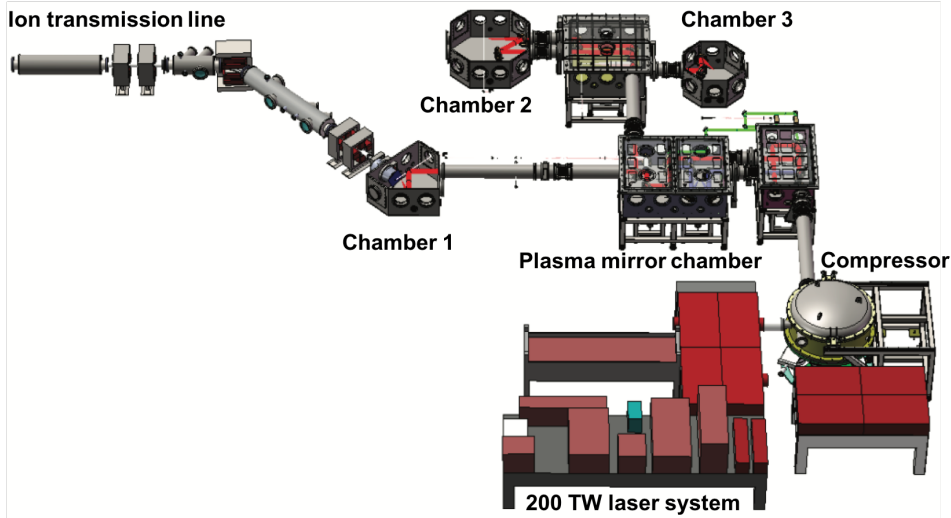


**Figure 3.3:** Layout of the CLAPA facility at Peking University. [122]

The layout of Compact LAsEr Plasma Accelerator (CLAPA) of Peking University [122] is shown in Figure 3.3, which includes the following subsystems: 200 TW laser system, laser beamline, target chambers, ion beam transmission line, experimental terminal, and control system. Among them, the 200 TW laser is a commercial laser produced by THALES with high contrast ( $10^{-10}$  at -100 ps and  $10^{-6}$  at -5 ps), maximum output energy 5 J and pulse width 25 fs. The laser beamline and the target chambers (1, solid target chamber; 2, gas target chamber; 3, cluster target chamber) are used for laser experiments of various kinds. The ion beam transmission line realizes focusing, energy selection and refocusing of the laser-driven ion beam. The experimental

terminal part mainly performs ion irradiation experiments. The control system is responsible for the overall timing logic control and parameter measurement and data acquisition of the system.

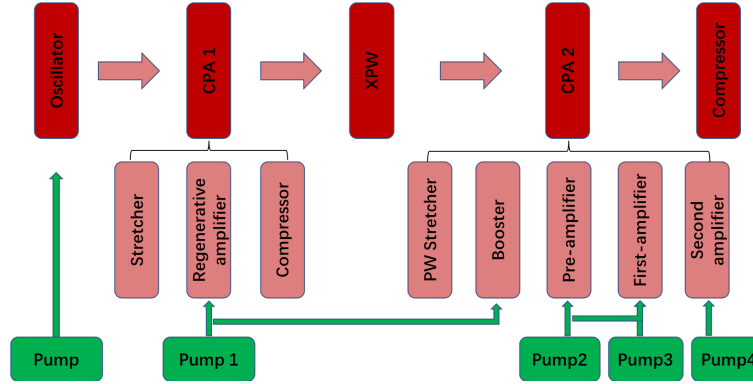


Figure 3.4: Schematic of CLAPA 200 TW laser system.

From the view of the structure, the 200 TW laser of the Peking University CLAPA system is a commercial laser based on double-chirped pulse amplification technology, which is different from the ATLAS 300 TW laser mentioned in the Section 3.1.1. As shown in Figure 3.4, the seed laser with the energy of nJ is generated by the oscillator, and then is transferred to the pre-stage CPA system, which is a regenerative amplification system based on Ti: Sapphire crystal, including an Offner-type stretcher, an amplifier, and a compressor. The stretcher uses two concentric spherical mirrors to eliminate aberrations and reduce high-order dispersion. The pulse after amplification is about  $500 \mu\text{J}$ , and after a double-grating compressor, the laser pulse energy is about  $150 \mu\text{J}$  with pulse duration about 35 fs. In order to improve the temporal contrast of the pulse, the CLAPA 200 laser system uses XPW (crossed polarized wave) technology to filter the waves after the pre-stage CPA. The filtering efficiency is over 15% and the temporal contrast is increased by 4 orders of magnitude (at -100 ps). After XPW (polarizer-BaF<sub>2</sub>-BaF<sub>2</sub>-polarizer), the laser pulse of about  $40 \mu\text{J}$  reaches the second-stage CPA, which consists of five parts: a PW stretcher, a Booster amplifier, a preamplifier, first-stage amplifier, and second-stage amplifier. The PW stretcher spreads the pulse to 400 ps, a DAZZLER is used to modulate the spectrum, and then the pulse enters a two-pass Booster amplifier. The pulse energy is amplified to  $200 \mu\text{J}$  and the frequency is 1KHz. After a Fast Pockels Cell, the frequency becomes 5 Hz. Afterward, the laser pulse passes through the pre-amplifier (30 mJ), the first-stage amplifier (1.4 J) and the second-stage amplifier (7 J), and then passes through a deformable mirror for wavefront adjustment and finally enters the vacuum compression chamber. After compression, single pulse energy can be up to 5 J, the pulse width is 25 fs, and the maximum power can reach 200 TW.

## 3.2 Ion detectors

### 3.2.1 Offline diagnostics

Different kinds of off-line ion detectors use nuclear track detectors (e.g. CR39, with chemical formula  $C_{12}H_{18}O_7$ ), Radiochromic Film (RCF), Image Plate (IP) and so on. From a principle point of view, CR39 is insensitive to photons or electrons, and when ions pass through CR39,

the deposited energy can cause the chemical bonds to break and traces which can be revealed by etching in a hot NaOH solution [123]. By counting these traces through a microscope, one can obtain the energy spectrum and profile information of the ion beam. As the name suggests, RCF is based on the effect of radiation discoloration, and after irradiation, the changed color will remain stable. As a sensitive component, micro-crystalline diacetylene becomes blue when exposed to ionizing radiation, and the degree of discoloration is related to the radiation dose. In a stack configuration, it is possible for RCFs to obtain spatial and spectral information of the ion bunch. Because the ions with energy beyond a certain threshold can penetrate one RCF and get to the next, a certain layer corresponds to a certain energy range [124]. IPs are based on a photo-stimulated luminescence (PSL) effect. They consist of a flexible plastic plate and an Eu-doped phosphor crystal coated on it. Firstly, by exposing IP to radiation (e.g. X-rays, UV light or ions),  $Eu^{2+}$  ions are excited to metastable states, producing a large amount of  $Eu^{3+}$  ions and releasing free electrons, in which the phosphor is capable of storing a fraction of incident energy and electrons in  $F^+$  centers. After the experiment, the used IP is stimulated with visible or infrared light (e.g. He-Ne laser beam), and the electrons captured by  $F$  centers are released and recombine with  $Eu^{3+}$  ions to form  $Eu^{2+}$ , while 390 nm light is emitted, whose intensity is proportional to the absorbed radiation energy [125]. In comparison, CR39 only responds to energetic ions, so it is highly resistant to the interference of photon or electron radiation. RCF is sensitive to all radiation, but has the advantage of simpler handling and evaluation. IP is also sensitive to all radiation, but it is a common detector for ions due to its high resolution and high dynamic range. More importantly, IPs can be reused after being erased by white light source.

### 3.2.2 Online diagnostics

Approaches for online detection has focused on optical techniques, i.e. monitoring the output of a scintillator screen [126] or multi-channel plate [127]. The scintillator converts incident radiation into visible light by luminescence, which can be detected by CCD cameras, Complementary Metal-Oxide Semiconductor (CMOS) imagers or photodiodes. The MCP is an array of millions of miniature electron multipliers oriented parallel to each other, usually made of lead glass. The channel axis is generally perpendicular or biased at a small angle to the end face coated with a conductive material as the input and output electrodes. The electric field along the channel will be established after the voltage is applied, with the result that the electrons generated by the radiation impinging on the channel walls are accelerated by the field and more electrons can be generated after they hit the wall again. This process will be repeated over and over again until the electrons reach the back surface of the MCP where they will be detected along with the CCD camera through the screen. The voltage is usually several thousand volts, which requires operating conditions under high vacuum conditions.

Pixelated semiconductor detectors are also usable for online detection. The interaction between radiation and matter will lead to ionization and new electron-hole pairs will be generated from the depletion layer whose number depends on the the deposited energy of the incident radiation. Therefore, such semiconductor detectors can be used to detect ion or other radiation. A commercial system from Teledyne Rad-Icon Imaging Corporation based on a CMOS silicon photodiode array (RadEye1<sup>TM</sup> sensor) is widely used in our group because of its high dynamic range and resolution. This detector is originally developed to detect visible light or x-rays with a scintillator attached on the surface. However, with the help of passive layer  $SiO_2$  placed on

the surface of an active layer of Si, one can extract ion signals whose response scale linearly with energy deposited by ions within the active layer [128].

### 3.3 Spectrometer

In order to determine the energy spectrum of an ion bunch, an electric and/or a magnetic field in front of the detector is required. The deflection amplitude is a measure of Charge to mass ratio and kinetic energy of the ion. From the spatial distribution on the two-dimensional screen one can then reconstruct the energy and  $q/m$  distribution of the ion bunch (Thomson parabola). In case of a single and known ion species (for example protons), one can deduce the angular-energy (Wide-angle magnetic spectrometer, WASP, case).

#### 3.3.1 Wide angle spectrometer

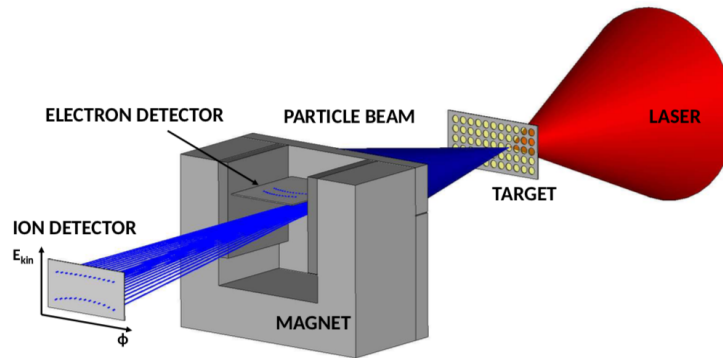


**Figure 3.5:** Schematic of the novel electron and ion WASP, taken from F. H. Linder's thesis [129]

An automatic online, compact WASP was designed and developed to measure the angularly resolved energy spectra of both laser-driven ions and electrons [129]. It consists of a slit that truncates the ion bunch into a fan-beam which is then passing a magnet with a wide gap. RadEye1 detectors register the ions on an area of 5 cm by 10 cm.

The dipole magnet has a 10.5 cm gap and 10 cm by 10 cm permanent magnets with a magnetisation of 1-1.4 Tesla. They are fixed to both sides of the steel yoke (Figure 3.5). The entrance of the steel yoke has a flat plate with a  $5 \times 1 \text{ cm}^2$  wide slot in the middle of the plate for passing the ion beam. The initial broad slot gives the opportunity of scintillation to attach an additional narrow slit for an appropriate selection and the narrower the slit the higher the energy resolution. When the ion beam passes through the slit to the inside of the steel yoke, the magnetic field generated by the strong magnets on both sides of the steel yoke causes the ion beam to be deflected by the Lorentz force. Due to the non-uniformity of the dipole magnetic field, it is necessary to measure and calibrate the magnetic field strength at each point with a spacing of 2 mm using three-axis hall magnetometer manufactured by Metrolab Technology SA [130].

As shown in the schematic 3.5, the plasma bunch from the laser irradiated foil target diverges

and is blocked by the entrance plate of the WASP, except for a small line segment defined by the slit (not visible in Figure 3.5). The particles with a negative charge (electrons) will bend upwards and those with a positive charge (protons or positively charged ions) will bend downwards in the magnetic field. Both detection planes for electrons and ions are equipped with RadEye1 detectors and a scintillator is attached to that for enhancing the electron detection efficiency. In order to suppress the effect of electromagnetic pulses on RadEye electronics, an aluminum detector housing with at least 5 mm thickness was designed in this setup, which functions as a Faraday cage. Since the 5 mm thick aluminum is capable of stopping all the electrons below 2 MeV and the ions below 30 MeV, a window of the same size as the detectors has been cut out and been replaced by a 15  $\mu\text{m}$  thick aluminum foil to shield light and low energetic particles or X-rays. In addition, four RadEye1 detectors are assembled together to have a large sensitive angle.

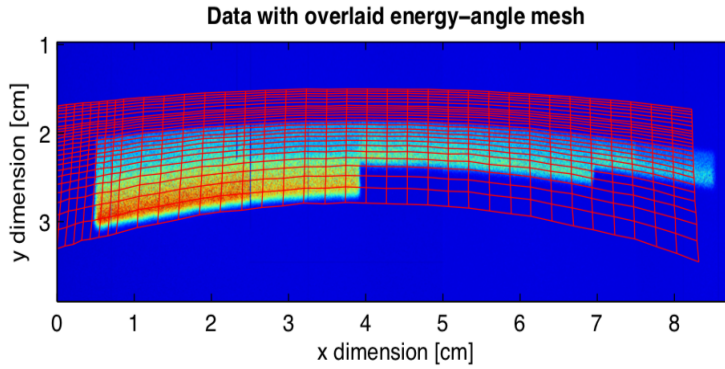


**Figure 3.6:** Raw data obtained with stepped Aluminum layers covered on the detector. The energy-angle mesh on the top is in red color. [129]

Figure 3.6 shows a typical image of a 10  $\text{cm} \times 5 \text{ cm}$  Radeye1-output. The color represents the deposited energy at a certain position which is related to the number of ions. The horizontal position encodes the angle of the respective ions, the vertical dimension corresponds to the deflection in the magnetic field, the lower the proton energy the stronger is the (downward) deflection. The visible edges (3 steps) correspond to distinct proton energies that were sufficient to penetrate additional foils that were placed just in front of the Radeye-sensor to obtain an energy calibration. The edges are curved because the magnetic field in the center is smaller than at the poles. Therefore, we typically track ions through the inhomogeneous magnetic field and generate an angular-energy-mesh (red grid in Figure 3.6). This way, we can associate different detector positions to pairs of energy and angle. The distribution function in  $x$  and  $y$  can then be transformed into the required distribution function in energy and angle. Predominantly we use only the energy distribution in a certain angle (or an energy distribution averaged over a certain angular region). The WASP was employed in experiments that will be presented in Chapter 4.

### 3.3.2 Thomson parabola spectrometer

The Thomson Parabola Spectrometer (TPS) is one of most used ion detectors in laser-plasma experiments due to its unique capability of simultaneously characterizing the energy spectrum while separating ion species with different charge ( $q$ )-to-mass ( $m$ ) ratios. The reason is that TPS

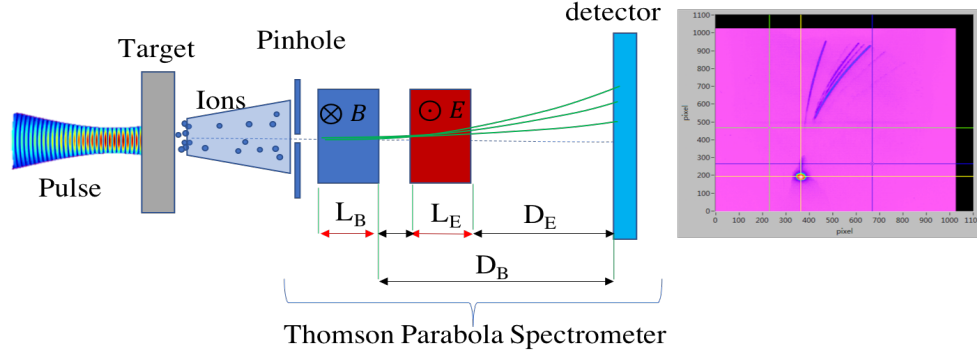


**Figure 3.7:** Schematic of a typical TPS with regions of static magnetic and electric fields. The trajectories of positively-charged ions and a neutral particle are depicted by green lines and a dashed blue line, respectively.

combines electric and magnetic fields. In a typical TPS (see Figure 3.7), an ion beam selected by a pinhole at its entrance passes through a parallel magnetic field and electric field region applied transversely to the beam axis. Referring to Figure 3.7, the magnetic fields determine the y-coordinates of the ions on the detector and  $q/m$ , while the electric fields deflect the ions along the x-axis. The ion signal observed in the detector consists of parabolic curves, the leftmost one with smallest curvature due to proton. The other curves are due to carbon ions and oxygen ions. Assuming that the electric and magnetic fields are uniform, the ion coordinates along the y (due to the magnetic field) and x (due to the electric field) axes on the detector plane can be analyzed as described below,

$$x = \frac{\gamma}{\gamma^2 - 1} \frac{qEL_E}{m_0c^2} (D_E + L_E/2), \quad (3.1)$$

$$y = \frac{1}{\sqrt{\gamma^2 - 1}} \frac{qBL_B}{m_0c^2} (D_B + L_B/2), \quad (3.2)$$

where  $m_0$  and  $q$  are the rest mass and charge of the ions,  $c$  is the speed of light,  $E$  and  $B$  are the electric and magnetic fields,  $\gamma$  is the relativistic Lorentz factor and  $L_E$ ,  $D_E$ ,  $L_B$ ,  $D_B$  are the relative lengths or distances labelled in Figure 3.7.

For non-relativistic velocities ( $v_z \ll c$ ), after a first-order Taylor expansion around  $\gamma = 1$ , the resulting particle trajectory equation satisfies that  $x$  is proportional to the square of  $y$ , which is also the reason for the name of the parabola spectrometer. The advantage of TPS is that multiple  $q/m$  ion signals can be observed simultaneously. The drawback is that the Pinhole selects only a small portion of the beam and hence no spatial information of the ion beam is obtained. Also, due to the overlap of different ion signals overlap each other at the high energy end, it is not easy to separate contributions of ions with similar  $Z/M$  values.

The TPS is used in experiments described in Chapter 5.



# Chapter 4

## High-repetition-rate laser-driven proton source

### 4.1 Nano-foil target positioning system (nFTPS)

#### 4.1.1 Composition of nFTPS and positioning routine

From the perspective of composition, nFTPS consists of four parts, namely the mounting component, measurement and observation equipment, delivery component and operation interface. The mounting component is primarily a target wheel with target holders. The measurement and observation equipment consists of a linear motor, a confocal chromatic sensor and a microscope that allows viewing the target with two different magnifications simultaneously. The delivering components include a rotary motor and a Hexapod. The operation interface is written in Labview (Figure 4.1).

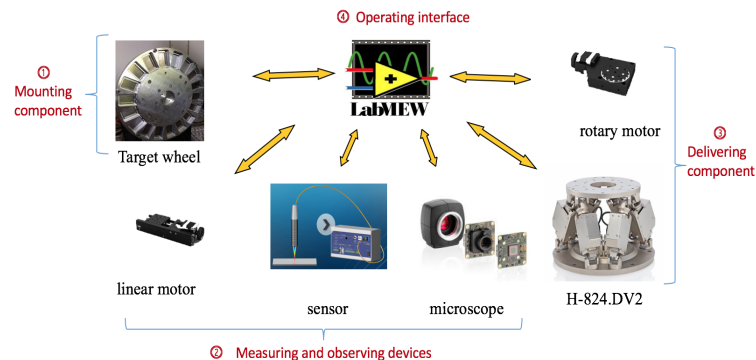


**Figure 4.1:** Components of nFTPS. 1. Mounting component: a target wheel. 2. Measuring and observing devices: a linear motor, a confocal chromatic sensor and a microscope with two simultaneous magnifications. 3. Delivering component: a rotary motor and a Hexapod. 4. Operating interface: codes written with Labview

The nFTPS can be defined as a semi-automatic searching and positioning target system. The

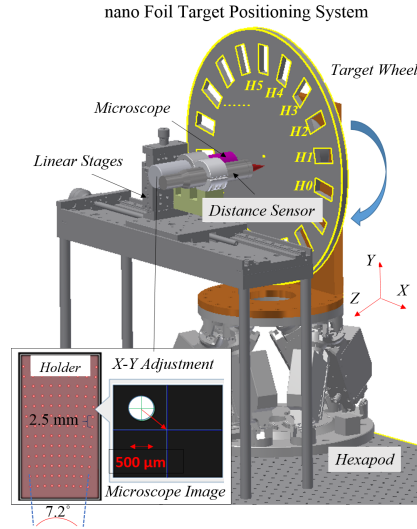


**Figure 4.2:** Schematic of nFTPS. Plastic film targets with thicknesses between 50 nm and 1  $\mu\text{m}$  cover the holes on the target holders (bottom left), which are then mounted in the target wheel. The diameter of the target holes is 500  $\mu\text{m}$  and the distance between two holes along the same radial line is 2.5 mm, the angle between two adjacent radial lines is 0.903°. An adjustable microscope can be moved independently to observe and position individual targets in transverse direction ( $xy$ ). The chromatic distance sensor is used to adjust the longitudinal target position ( $z$ ).

assembly is shown in Figure 4.2. The target wheel can accommodate 17 target plates. Each plate has 99 holes over which the targets are mounted. One frame is typically kept free for alignment purposes such as optimization of the parabolic mirror. The space is sufficient so that we do not need to move the large wheel out of the laser beam path for regular checks. Given that 17 holders (H1-H17) are all loaded with targets, there can be a total of 1683 targets. Importantly, these 17 holders can separately accommodate different thicknesses of foils and even different materials, which is the advantageous for explorative studies and motivated the realization of this nFTPS in comparison to, for example, tape-drive targets [131]. The motion of the target wheel is controlled by a hexapod with six degrees of freedom (three translation and three angular rotation). In addition, the rotation of the target wheel around its geometrical center is provided by a motorized stage.

The target plane is imaged via two different magnifications (5-fold and 20-fold) onto a camera. The lower magnification arm gives an overview picture of a given target and the center of the circular target imaging plane should coincide with the target chamber center (TCC), which is determined by the laser focus point position. Accurate positioning within 5  $\mu\text{m}$  precision is supported by the arm with higher magnification. The chromatic distance sensor points at TCC as well and is used to measure target positioning deviations to TCC in the laser direction with 100 nm accuracy. The signal is fed back to the hexapod (4  $\mu\text{m}$  precision) for automatic pre-alignment.

Prior to the experiment, the coordinate of each target is first assigned coarsely based on the geometry of the target wheel. The targets will then be moved to the individual assigned positions with real time measurement performed with the microscope and the distance sensor. Deviations of the measured target position from the pre-assigned coordinate system are measured in  $x$  and

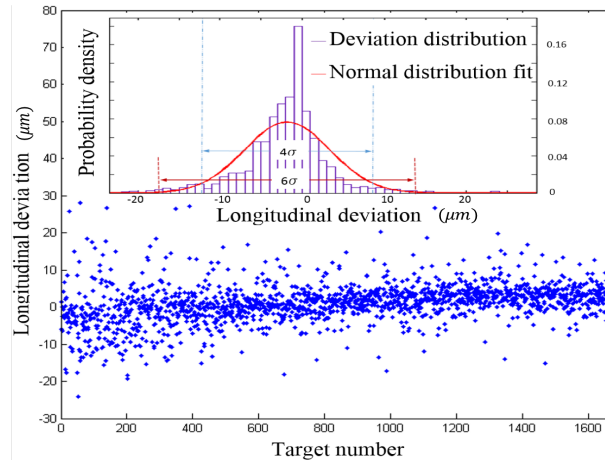


**Figure 4.3:** Deviation (in z-axis) distribution of 1683 targets (17 holders) and corresponding normal distribution fit. After positioning all targets via the microscope and distance sensor, the displacements after repositioning are shown blue. The measurements are performed in vacuum condition.  $\sigma$  is the standard deviation.

y dimensions using a 5-fold microscope, as shown in the bottom left corner of Figure 4.2. The values in z axis (laser direction) are measured by the distance sensor. Based on the recorded data, the hexapod corrects measured deviations that arise from inaccuracies of the wheel and the target geometries. The pre-alignment procedure results in a set of coordinates for each target, which is stored in a list.

A complete experiment requires the six following steps,

1. Trigger connection for all devices.
2. With the distance sensor, the target wheel is aligned perpendicular to the laser beam axis.
3. Lateral position correction with microscope.
4. Longitudinal depth compensation with distance sensor.
5. Select shot mode and perform shooting.
6. Stop program and disconnect devices.

It should be noted that in addition to the initial two target coordinates that need to be manually selected, the remaining steps are automatically performed by an algorithm. The operator only needs to follow the instructions step by step. For detailed operation steps and instructions, please refer to my master's thesis [132].

#### 4.1.2 Characterization of nFTPS

As the first step, we evaluated the repeatability of positioning the targets. For this procedure, instead of shooting the laser pulse onto the targets, the longitudinal position of the target was re-measured by the distance sensor at 1 Hz. As shown in Figure 4.3, only small deviations are observed with a mean value of  $1.8 \mu m$  and the standard deviation of  $5.2 \mu m$  among the entire target wheel. This precision of the complete nFTPS in operation almost reaches the entire journey precision of the hexapod which is specified as  $4 \mu m$ . The largest deviations do not exceed

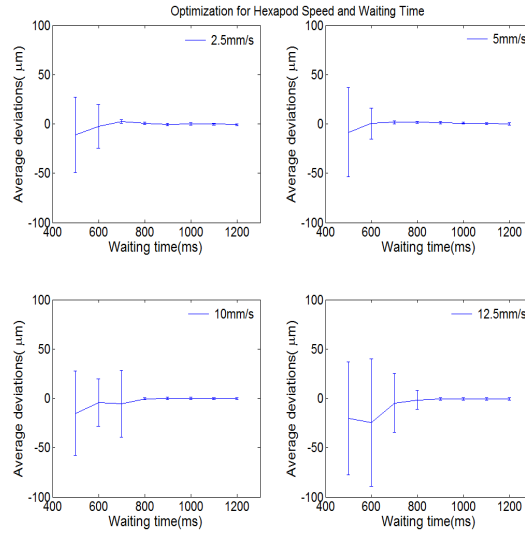


**Figure 4.4:** The trend of average deviations after movement for different hexapod velocities. Each point represents the average deviation for 99 targets of one holder, which were measured via the same procedure as described for Figure 4.3. The error bars represent the standard deviation of 99 data points.

$30 \mu\text{m}$  and are probably caused by faulty target foils which are inevitable in the floating process which we employed for producing the targets.

The motion speed of the hexapod when switching between different targets has a strong impact on the positioning accuracy of the nFTPS. As shown in Figure 4.4, we examined the positioning accuracy for various speeds of the hexapod from 2.5 to 12.5 mm/s. The deviation from the targeted position is represented by the average value of the longitudinal deviation to TCC extracted from consecutive measurements of 99 targets. Those values were measured after a given waiting time where timing started from the end of the hexapod movement, which takes 200 ms. For a given speed, the system will relax to a constant value. The deviation of the foil position was measured related to the time after the nFTPS started moving to a new target. Considering a movement time of 450, 250, 170 and 150 ms for switching targets with a motion speed of 2.5, 5, 10 and 12.5 mm/s, respectively, we derived the stabilization time defined as the total time to reach the positioning accuracy below  $5 \mu\text{m}$ , as 1150, 900, 1020 and 1100 ms, respectively. Thus, for the desired operation of 1 Hz repetition rate, we operated the nFTPS system at the motion speed of 5 mm/s to have a minimum relaxation time. Note that the results shown in Figure 4.3 were measured at this speed.

Further on, the details of the stabilization process are shown in Figure 4.5, where the longitudinal deviations in real-time to TCC were recorded over 1 s after the hexapod movement had just stopped. In addition to the decay of the vibration amplitude, a beating-wave-like behavior was observed in Figure 4.5(a). Figure 4.5(b) shows the result of the Fast Fourier Transformation (FFT) of the signal in Figure 4.5(a), where two adjacent frequency peaks are clearly visible around  $50 \text{ Hz}$ . Those two frequencies  $f_1 \approx 47.6 \text{ Hz}$  and  $f_2 \approx 49.8 \text{ Hz}$  give rise to the special beating wave structure. We obtain a fitting function  $D = 20e^{-3t}[\cos(2\pi f_1 t) - \cos(2\pi f_2 t)]$  based on the two frequencies with a fitting damping ratio of 3 per second and initial amplitude of  $20 \mu\text{m}$ , shown in Figure 4.5 (c), well agreeing with the measurement in Figure 4.5(a). The origin of the vibration is not yet clear but understanding it will enable us increase the damping

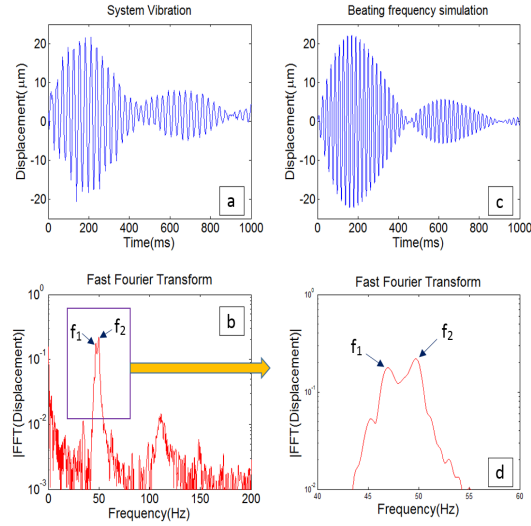


**Figure 4.5:** (a) System vibration induced by ceasing hexapod with speed of 12.5 mm/s, (b) the corresponding Fast Fourier Transform and (c) beating frequency simulation. The real time displacements are measured on one film target with the distance sensor after hexapod movement with speed of 12.5 mm/s in vacuum condition.

rate. One experiment where a plane mirror was used instead of the target wheel showed that a similar beating frequency phenomenon appeared as well. Therefore, we can conclude that the beating frequency behavior originates from the hexapod; the target wheel amplifies the vibration amplitude due to its larger size. In fact, this two-frequency beating behavior simulation is just one simplified model. As the hexapod has six motors working together to drive the platform, six frequencies should be taken into consideration and in that way one could hope to identify the motors that have strongest impact.

### 4.1.3 Advantages and disadvantages of the nFTPS

The advantages of this system are simple operation process and the ability to choose different materials and thickness targets. However, this prototype is not yet space-efficient. The main design considerations were: (a) to ensure stability by a rigid construction and mediate remaining imperfections by searching targets and pre-defining their position prior to shooting the laser; (b) to mediate damage of neighboring target by allowing for sufficient distance between targets. For PW-lasers, it is expected that the distance between targets may have to be even larger.

## 4.2 0.5 Hz laser-driven proton source based on nFTPS

### 4.2.1 Experimental setup

The schematic of the experimental setup and the employed instruments is shown in Figure 4.6. Capital letters indicate the extracted observables. A 30 fs laser pulse centered at 800 nm was focused by a 90° off-axis-parabola (OAP) onto the target. The full-width at half-maximum

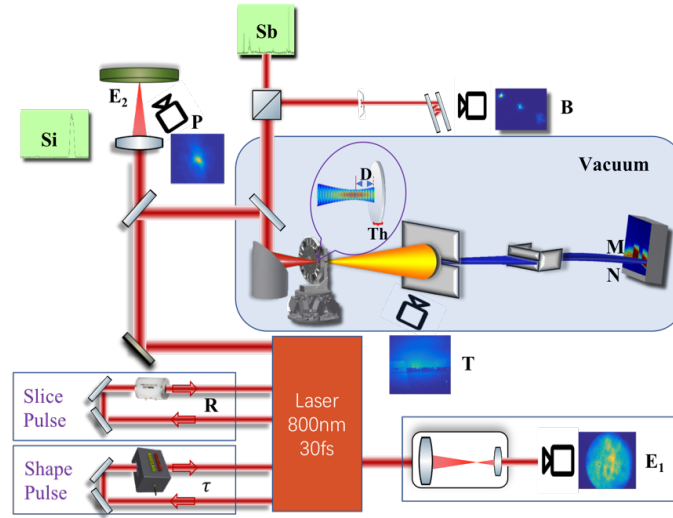


**Figure 4.6:** Schematic of experimental setup. Different uppercase letters indicate different instruments and extracted observables as described below.  $B$ -Backscatter image-pixel integral of multiplexed focal spot image - (backscatter/reflection at mainly  $2\omega$ ).  $D$ -Defocus controlled via nFTPS.  $E_1$ -Incident laser energy via near-field pixel integrated image.  $E_2$ -Incident laser energy via far-field pixel integrated image.  $M$ -Maximum kinetic energy and  $N$ -Ion number per msr in energy band 2.5-10 MeV, both measured by a wide-angle spectrometer.  $P$ -Pointing position from far-field image.  $R$ - Trigger time for fast Pockels cell prior to the intensity peak of the laser pulse.  $Si$ -Incident laser pulse spectrum between 750 and 850 nm.  $Sb$ -Backscatter spectrum integral ( $Sb_{2\omega}$ : 350-450 nm;  $Sb_{\omega}$ : 800-1000 nm).  $T$ -Transmission image.  $Th$ -Target thickness (measured prior to irradiation).  $\tau$ - Pulse duration controlled by Dazzler.

(FWHM) diameter of the focal spot was  $3.3 \mu m$ . Considering a laser energy 4.8 J before the compressor, a transmission efficiency to target 50% , the peak intensity was estimated to be  $3.4 \times 10^{20} W/cm^2$  on target based on high-dynamic-range (HDR) focal spot imaging [133]. All laser energy measurements were cross-calibrated using an energy meter to reflect the value before the compressor entrance. The actual Rayleigh length was about  $25 \mu m$ .

Behind the last telescope in the laser system, a charge-coupled device (CCD) is used to capture a near-field image of the laser pulse. Incident laser energy  $E_1$  was obtained by integrating the near-field image. Similarly, the incident energy  $E_2$  of the laser could also be obtained by integrating the far-field image, which was recorded by another CCD camera that imaged a scatter screen on which a lens focused light leaking through a turning mirror before the laser entered the experimental chamber. The center of mass of the far-field image represented the pointing position  $P$  for monitoring the shot-to-shot fluctuation of the laser focus position. The correlation of this measure to the on-target focus position was validated prior to experiments at reduced laser power by comparison to the focus image provided by the high magnification microscope. A spectrometer recorded the spectrum  $Si$  of the incident laser pulse from the same scatter screen. The integration of  $Si$  in the range of 750-850 nm could be used as a third incident energy reference. In addition, the real-time measurement of the incident spectrum could reveal problems of the laser system on a shot-to-shot basis, thereby enabling identification of bad shots. The transmission image  $T$  was detected by a CCD camera that imaged a screen located behind the target in the laser propagation direction.

The protons emitted from the target were analyzed by a wide-angle spectrometer that was

equipped with RadEye1 CMOS sensors [134, 135]. The two-dimensional image allowed for retrieving the energy spectrum (and the angular distribution) of a fraction of the beam [134, 136], from which the maximum kinetic energy  $M$  and the particle number per milliradian (msr)  $N$  at different angles between  $-2^\circ$  and  $2^\circ$  at target normal were measured. The backscattered light was collected by the same OAP mirror that also focused the main pulse, guided out of the vacuum chamber through a specially designed partially transmissive mirror, and refocused onto a camera. Two nearly parallel silver mirrors were inserted between lens and camera and served to replicate the backscatter image [137]. The replicas of the backscattered light hence represent laser intensity distributions at different focal planes, we call this setup therefore equivalent plane monitor. Typically, five spots were fit onto the chip and the setup was adjusted to minimize the size of the central replica when a target was in best focus. A displacement of the smallest replica from this original position for a certain laser shot indicates that the target was not in the anticipated longitudinal position, i.e. it could yield the defocusing condition of the laser focus on the target and should be related to the active displacement that we measured via  $D$ . We found the quantitative evaluation of this measure rather complicated and restricted the use of this tool to estimate the strength of the backscatter signal. Amongst the five replicas, at least one was not saturated and could be integrated to yield a (not absolutely calibrated) measure that is proportional to backscattered light energy (B). The spectrum  $S_b$  of this backscattered light was also simultaneously detected in the second arm of this diagnostic.  $S_{b_{2\omega}}$  and  $S_{b_\omega}$  represent the intensity integral of the second harmonic generation (SHG) spectrum (350-450 nm,  $2\omega$  light) and the original spectrum including a region for potential red-shift (800-1000nm,  $\omega$  light), respectively.

An acousto-optic programmable dispersive filter (DAZZLER [138]), which is an integral part of the laser system, was used to modify the pulse duration  $\tau$ . A fast Pockels cell located behind the regenerative amplifier was triggered at time  $R$  prior to the peak of the main pulse to change the duration of the ASE pedestal, similar to the studies in the reference [61]. This variation may also discriminate short pre-pulses, that arrive before the trigger time.

Prior to the experiment, more than 1000 plastic foil targets were mounted on the nFTPS. The thickness of each target (variable  $Th$ ) was measured via an optical confocal microscope prior to mounting them into the target wheel of the nFTPS. Before the actual laser experiment, we performed one run in which we checked the repositioning procedure and found that the longitudinal accuracy was  $8 \mu m$ , similar to our previous results [139]. The parameter  $D$  denotes the active displacement that we chose for each shot and that was varied in steps of  $25 \mu m$ .

In addition, the temporal intensity curve was measured before the experiment by third-order autocorrelation, in which the temporal contrasts of the pre-pulses (their ratio with respect to the main peak) at around -660 ps and -500 ps were just above  $10^{-6}$ , while the ASE pedestal level was about  $10^{-9}$  [140].

### 4.2.2 Data processing

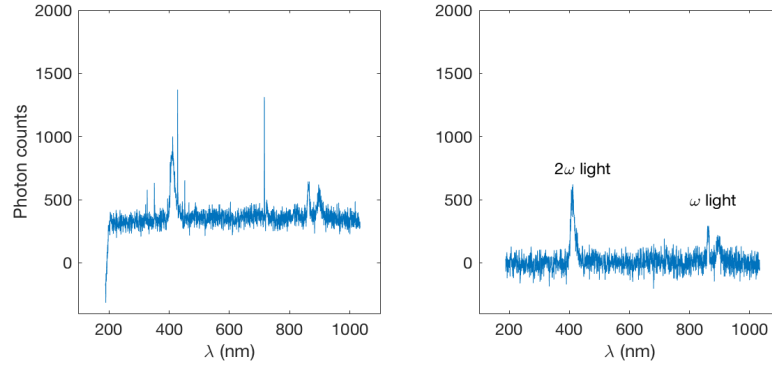


**Figure 4.7:** Backscatter spectrum raw data(left) and after subtracting background (right).

**Processing of backscatter spectrum** After removing the background, the integral  $Sb_{\omega}$  from 800 nm to 1000 nm is used to represent  $\omega$  light with red-shift and the integral  $Sb_{2\omega}$  from 350 nm to 450 nm denotes the second harmonic generation. Figure 4.7 shows the backscatter spectrum raw data (left), the background spectrum (BG) of the spectrometer (inset) and the spectrum after subtracting the background spectrum and the sharp noise signals (right).

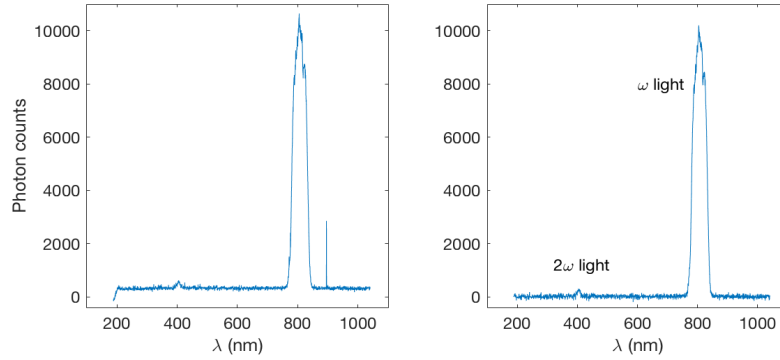


**Figure 4.8:** Incoming spectrum raw data (left) and that after subtracting the background (right).

**Processing of incoming spectrum** The incoming spectrum was processed in the same way as the backscatter spectrum. The background spectrum was first subtracted, and then the  $\omega$  light from 750 to 850 nm was integrated and recorded as  $S_i$  (Figure 4.8). The weak  $2\omega$  optical signal in the incoming spectrum is unexpected. It likely originates from scattering of the light reflected from the target, that contains a large portion of  $2\omega$  light.

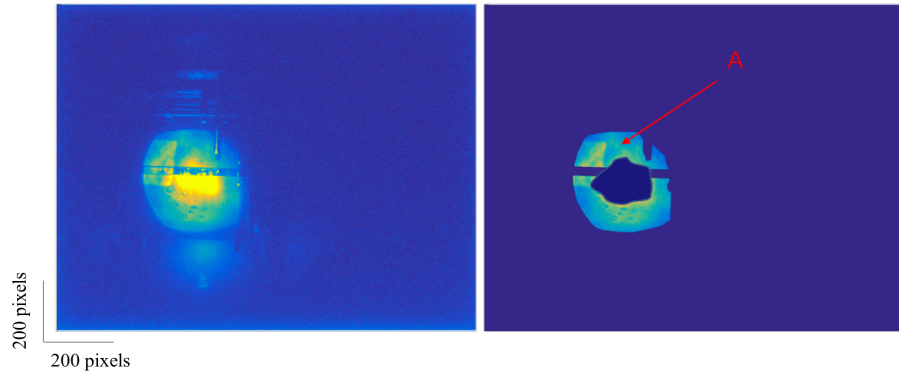


**Figure 4.9:** Transmission image raw data (left) and that multiplied by mask A (right) for an empty shot to ensure that the selected area is not saturated.

**Processing of transmission spectrum** Figure 4.9 shows an empty shot (without target) of the transmitted image raw data (left) and multiplied by the mask A (right), the pixel integral of which was set to  $T_0$ . The mask A is used to maximize the selection of unsaturated effective regions. The transmission image pixel integral in the same area of A for a normal shot was set to  $T$ . Then the transmittance is represented by  $T/T_0$ .

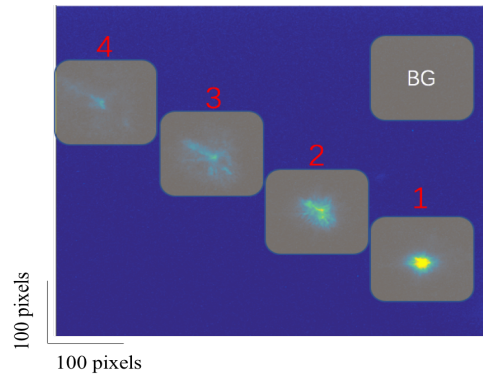


**Figure 4.10:** Backscatter image of the equivalent plane monitor. 1, 2, 3, 4 are the spots that appeared on the CCD camera through different paths. BG represents a background area having the same size.

**Processing of backscatter image** We choose four spots from the equivalent plane monitor and label them as 1, 2, 3, and 4 respectively (Figure 4.10). The unsaturated spot 4 was selected and the pixel integral minus the background in the defined area represents the backscatter light B.

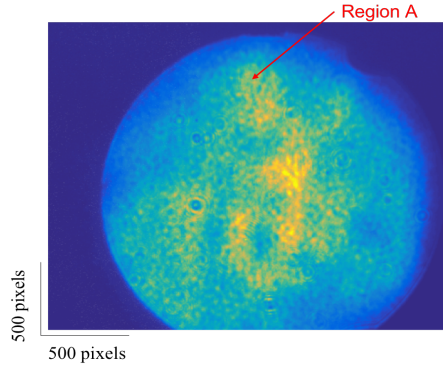


**Figure 4.11:** Near field image obtained behind a telescope.

**Processing of near-field image** As shown in Figure 4.11, we selected Region A and subtract the background before integration. Then, compared to the reference value  $R$  of 5.2 J before the compressor, the laser energy  $E_1$  at a certain shot can be obtained via the following formula,

$$\frac{\sum(\text{Region A})}{R} = \frac{E_1}{5.2J} \quad (4.1)$$

where  $E_1$  can be used as a real-time monitoring tool for laser energy.

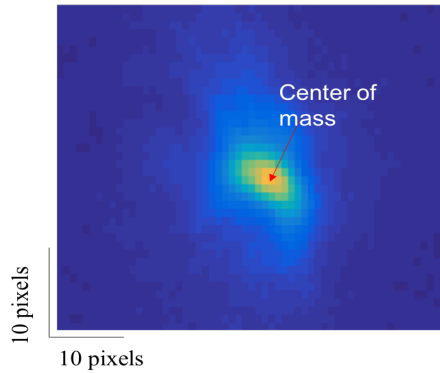


**Figure 4.12:** Far field image obtained from a screen behind a lens.

**Processing of far-field image** Two observables were extracted from the far-field picture, the laser energy and its laser pointing. The method of obtaining laser energy is the same as that of the near-field image, that is, integrating the effective area of the picture without background, and then obtaining the laser energy  $E_2$  by comparing the reference values. For pointing we find the centroid (Figure 4.12). The center of mass of the far-field image represents the pointing position  $P$  and it allows monitoring the shot-to-shot fluctuation of the laser focus position. The correlation of this measure to the on-target lateral focus position was validated prior to experiments at reduced laser power by comparison to the focus image provided by the high magnification microscope.

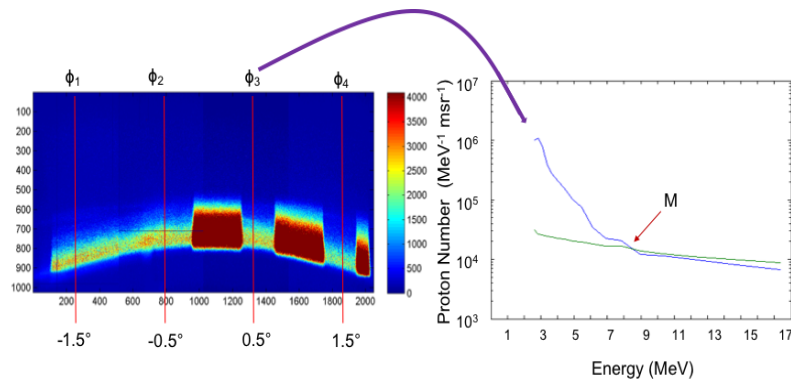


**Figure 4.13:** Proton signal raw data (left) from wide-angle spectrometer and the energy spectrum at a certain angle (right).

**Processing of proton signal** Figure 4.13 shows the raw data of the proton signal obtained via the wide-angle spectrometer (left) and the extracted proton spectrum (blue curve) at the angle  $0.5^\circ$  (right). The intersection of the proton spectrum and the background curve (green curve) was defined as the proton maximum kinetic energy  $M$ . The number of the measured protons per milliradian was defined as  $N$ . The dark red (strong) signals in the raw data (left) are due to wider entrance slits that was chosen for technical reasons in this angular range.

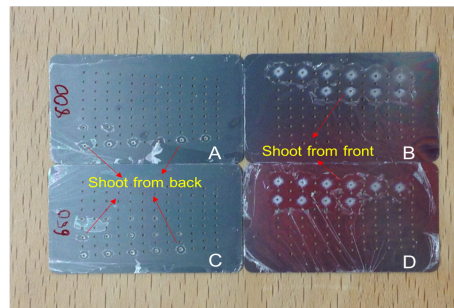


**Figure 4.14:** Pictures of target holder with some targets shot by laser from different side of the holder.

**Target preparation and localization** For high-repetition experiments, target preparation and precise positioning are key. One important precaution is to ensure that adjacent targets were not damaged by a previous shot.

In preparatory experiments, we have identified the problem, that when the foil on the target holder faces towards the incoming laser, neighboring targets are affected (Figure 4.14 B and D), while when facing away from the laser, the neighbor-damage is less (Figure 4.14 A and C). This setting was therefore chosen for the following studies.

Since the target was prepared by the droplet method, the thickness of a whole target varied in different regions by as much as 10% [57]. Therefore, we measured and recorded the target thicknesses  $Th$  for each hole one by one.

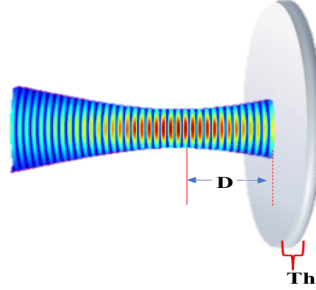


**Figure 4.15:** Schematic of target thickness  $Th$  and defocusing displacement  $D$

### 4.2.3 Experimental results

#### Stability measurement

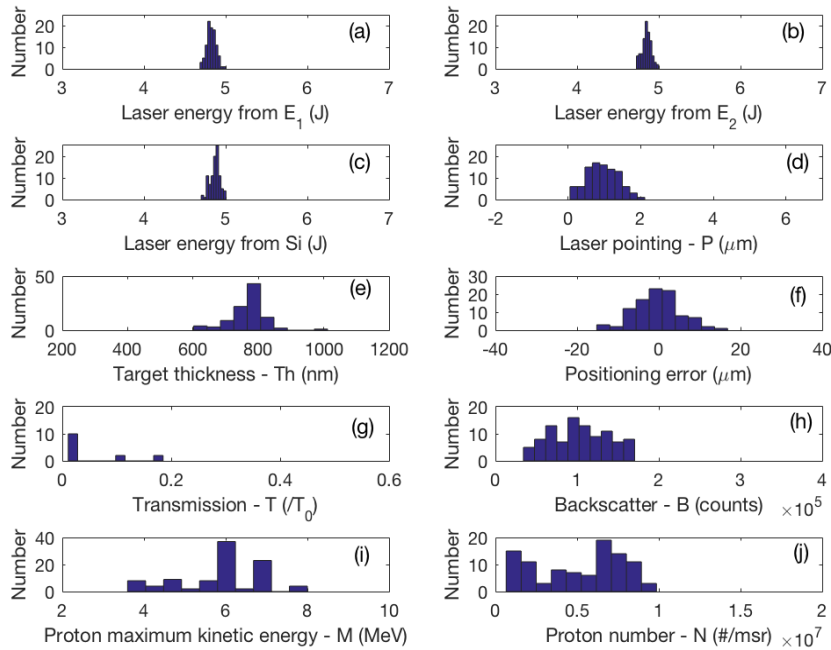


**Figure 4.16:** Histograms of shot to shot performance of non-controllable parameters (a-f) and the corresponding monitoring data (g-j) over 99 shots. The uppercase letters indicate the same meanings as in Figure 4.6

The first set of data comprises shots with full laser energy and 99 targets. The statistic distribution of laser energy extracted from  $E_1$ ,  $E_2$  and  $S_i$ , laser pointing  $P$ , target thickness  $Th$  and

positioning error are shown in Figure 2(a)-(f). The mean incident laser energy  $E_1$  was 4.8 J with a standard deviation of 0.06 J and it was similar to the results extracted from  $E_2$  and  $S_i$  (Figure 4.16(a-c)). Excellent laser pointing was achieved within the data set, with a small deviation of 0-2  $\mu\text{m}$  between the measured pointing position of the laser focus  $P$  and the reference position defined with attenuated pulse energy (Figure 4.16(d)). The plastic film thickness distribution histogram was shown in Figure 4.16(e) reveals a thickness of 780 nm with a standard deviation of 60 nm. The longitudinal position accuracy (or error) of the nFTPS can in principle reach 4  $\mu\text{m}$  [139] but was limited to 4  $\mu\text{m}$  in our case for the first confidence interval (Figure 4.16(f)).

The transmission  $T$  and backscatter light  $B$  in Figure 4.16(g) and Figure 4.16(h) present large fluctuations. Some transmission data was missing due to trigger failures or electromagnetic pulse (EMP) interference. In 60 of the 99 shots, the proton maximum kinetic energy  $M$  was between 6 MeV and 7 MeV and the remaining shots yielded to energies in the range of 3.5-8 MeV (Figure 4.16(i)). The total number of protons per msr  $N$  in energy band 3.5-8 MeV varied within one order of magnitude (Figure 4.16(j)).

The first set of results gives confidence that the parameters such as laser energy and target thickness fluctuate but perform normally. Proton bunch parameters, in particular the maximum kinetic energy and even more the number of protons per msr show strong fluctuations.

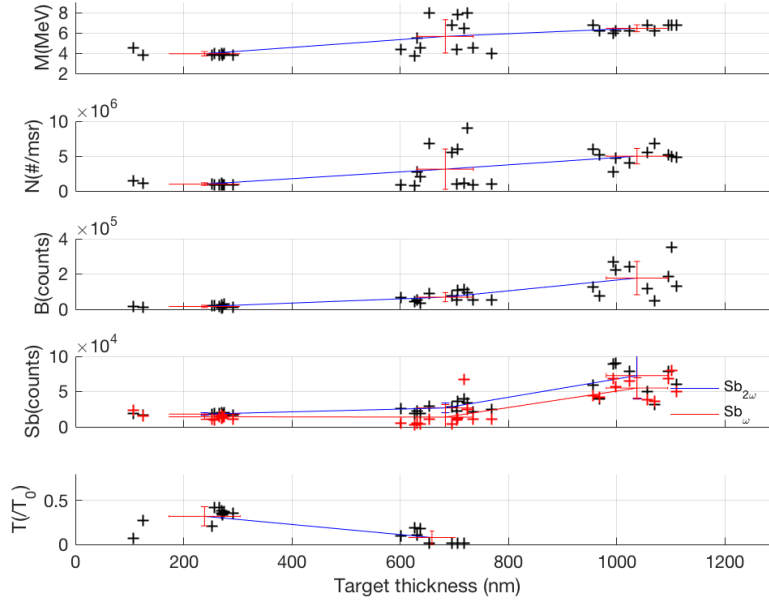


**Figure 4.17:** Other signal trends over thickness variation.  $M$ -Maximum kinetic energy and  $N$ -Proton number per msr measured by the wide-angle spectrometer.  $B$ -Backscatter image pixel integral of an unsaturated spot.  $Sb$ -Backscatter spectra pixel integral ( $Sb_{2\omega}$ : 350-450 nm;  $Sb_{\omega}$ : 800-1000 nm).  $T$ - Transmission image pixel integral divided by that of an empty shot. Some transmission data were missing because of trigger problems or electromagnetic pulse (EMP) interference.

**Target thickness** For influence of the target thickness on the proton source, maximum kinetic energy ( $M$ ), proton number per msr ( $N$ ), the experimental data backscatter image pixel integral

of an unsaturated spot ( $B$ ), backscatter spectra integral  $Sb$  and transmission ( $T$ ) are shown in Figure 4.17. The target thickness was varied from 100 to 1000 nm. The proton number and the maximum proton kinetic energy increases with increasing target thickness. A similar trend was found for the backscattered light (both  $Sb_{2\omega}$  and  $Sb_{\omega}$ ). The transmission  $T$  has an inverse trend and decreases with increasing target thickness. Interestingly, proton energy and number fluctuate strongest at a target thickness of around 700 nm, where the transmission is low.

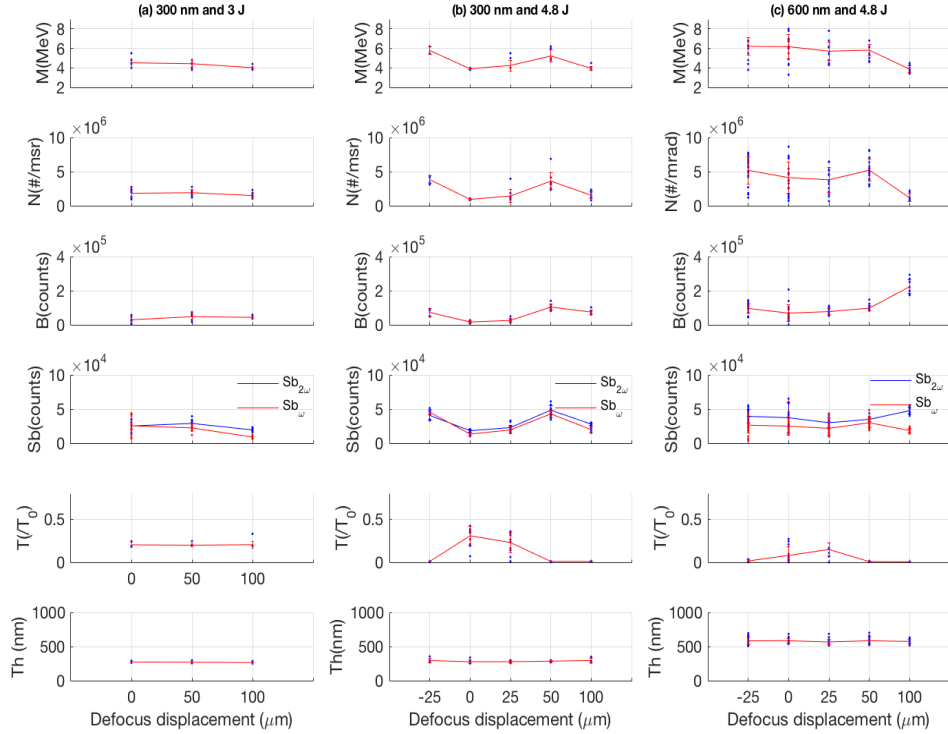


**Figure 4.18:** Defocus displacement variation in three cases. (a) Target thickness  $Th = 300 \text{ nm}$  and laser energy  $E_1 = 3 \text{ J}$ . (b)  $Th = 300 \text{ nm}$  and  $E_1 = 4.8 \text{ J}$ . (c)  $Th = 600 \text{ nm}$  and  $E_1 = 4.8 \text{ J}$ . The symbol  $+/-$  indicates that the target is located upstream/downstream of the laser focal plane. The capital letters  $M$ ,  $N$ ,  $B$ ,  $Sb$ ,  $T$  and  $Th$  represent the same meanings as in Figure 4.6. The target thickness as a function of defocus displacement was intentionally plotted here to exclude its effects.

**Defocus displacement** The three columns in Figure 4.18 show the effects of the active defocus displacement  $D$  on the proton source for three cases, (a)  $Th = 300 \text{ nm}$  and  $E_1 = 3 \text{ J}$  (30 shots) (b)  $Th = 300 \text{ nm}$  and  $E_1 = 4.8 \text{ J}$  (40 shots) (c)  $Th = 600 \text{ nm}$  and  $E_1 = 4.8 \text{ J}$  (90 shots), respectively. For case (a),  $M$ ,  $N$  and  $Sb$  decrease slightly as  $D$  increases from 0 to  $100 \mu\text{m}$ , i.e. from best focus to 4 times the rayleigh length.

For case (b), all data  $M$ ,  $N$ ,  $B$ ,  $Sb$  and  $T$  change nearly symmetrically around the focal plane from  $-25$  to  $25 \mu\text{m}$ . At  $D = 0 \mu\text{m}$ , largest  $T$  and smallest maximum energy  $M$  and particle

number  $N$  are measured. Displacing the target from the focus plane by  $50 \mu m$  maximizes  $M$  and  $N$ .

For case (c),  $M$  and  $N$  are not significantly affected by  $D$  in the range  $-25 - 50 \mu m$ . At  $D = 100 \mu m$ ,  $M$  and  $N$  are drastically reduced, and the corresponding  $Sb_\omega$  is also reduced, while  $Sb_{2\omega}$  is increased. It indicates that the efficiency of converting  $\omega$  light into  $2\omega$  light increases, but the efficiency for accelerating ions decreases. Combining Figure 4.18 (a), (b) and (c), it can be concluded that the effect of defocus distance on the ion bunch is not static but is related to the choice of target thickness and laser energy.

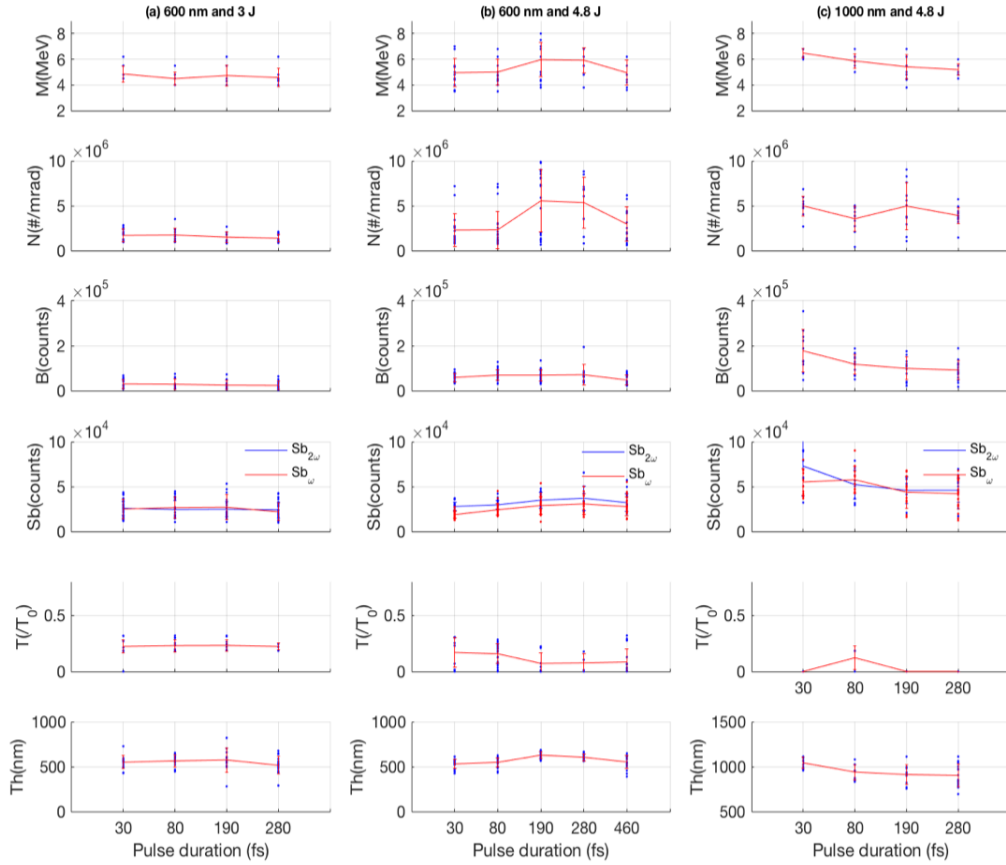


**Figure 4.19:** Variation of laser pulse duration in three cases. (a) Target thickness  $Th = 600 nm$  and laser energy  $E_1 = 3 J$ . (b)  $Th = 600 nm$  and  $E_1 = 4.8 J$ . (c)  $Th = 1000 nm$  and  $E_1 = 4.8 J$ . The capital letters  $M$ ,  $N$ ,  $B$ ,  $Sb$ ,  $T$  and  $Th$  represent the same meanings as in Figure 4.6. In order to avoid misinterpretation of apparent correlations, the target thickness as a function of pulse duration was intentionally plotted here.

**Pulse duration** Figure 4.19 represents the results for different pulse duration values  $\tau = 30, 80, 190, 280$  and  $460$  fs. Again, three cases are presented: (a)  $Th = 600 nm$  and  $E_1 = 3 J$  (b)  $Th = 600 nm$  and  $E_1 = 4.8 J$  (c)  $Th = 1000 nm$  and  $E_1 = 4.8 J$ . The lower row shows the target thickness which, as explained above, could not be kept perfectly constant.

For case (a), pulse duration  $\tau$  does not affect the proton parameters. Case (b) suggests a dependence on  $\tau$  but the trend in  $M$  and  $N$  is also observed in the target thickness, therefore suggesting that their dependence on pulse duration  $\tau$  is also weak in this case. The backscatter light  $B$  and  $Sb$  and transmission  $T$  remain substantially unaffected. A similar observation holds true for case (c). Combining the three situations (a-c), we do not observe a strong dependence of proton yield on laser pulse duration.

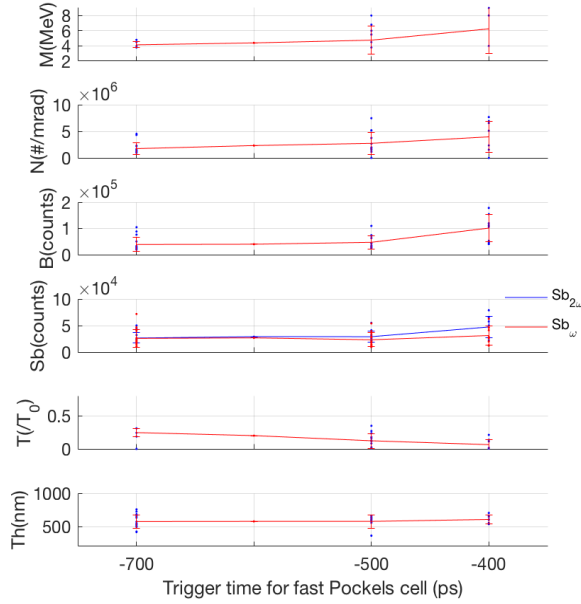


**Figure 4.20:** Variation of trigger time for fast Pockels cell. The capital letters  $M$ ,  $N$ ,  $B$ ,  $Sb$  and  $T$  represent the same meanings as in Figure 4.6. In order to exclude the influence of target thickness, the target thickness  $Th$  as a function of trigger time is plotted.

**ASE plateau duration** Figure 4.20 illustrates the influence of ASE plateau duration on the proton bunch. The trigger time for the fast Pockels cell at -700 ps means that the fast Pockels cell is triggered 700 ps prior to the main laser peak. By reducing the trigger time, the intensity of the ASE plateau (and some pre-pulses that arrive prior to this time) is reduced by around 2 to 3 orders of magnitude and is likely to be responsible for the increased proton energy  $M$  and number  $N$ . The default trigger time for all other measurement was at the minimum possible of -500 ps.

## Discussion

Some fundamental trends can be extracted from the results presented above. We observed that the maximum proton energy  $M$  and number  $N$  have a similar trend regardless of the parameters that were changed. This aspect is underlined by plotting  $N$  versus  $M$  in Figure 4.21. Even though the spread in the data is substantial, the general and expected trend is confirmed. More interesting is the interplay of measures that quantify the laser-energy before interaction and

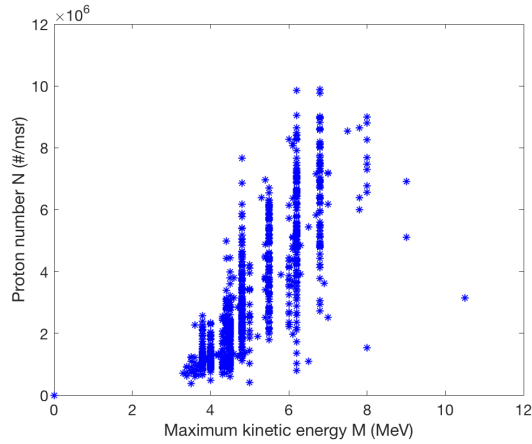


**Figure 4.21:** Proton number per msr  $N$  as a function of Maximum kinetic energy  $M$  in the case where no parameters such as laser, target and positioning are distinguished.

thereafter. In particular, transmission decreases and backscatter signal increases with increasing foil thickness (Figure 4.17) or by moving the target out of focus (Figure 4.18). Reducing the pre-pulse level has the same effect (Figure 4.20). The pulse duration, which was changed from 30 fs up to 460 fs, has little to no effect on the transmission and reflection and is surprising. It suggests that in our case, the pre-pulse interaction determined dominantly the plasma state during the interaction and might explain why in general the performance of the ATLAS-system in LEX-Photonics was not ideal.

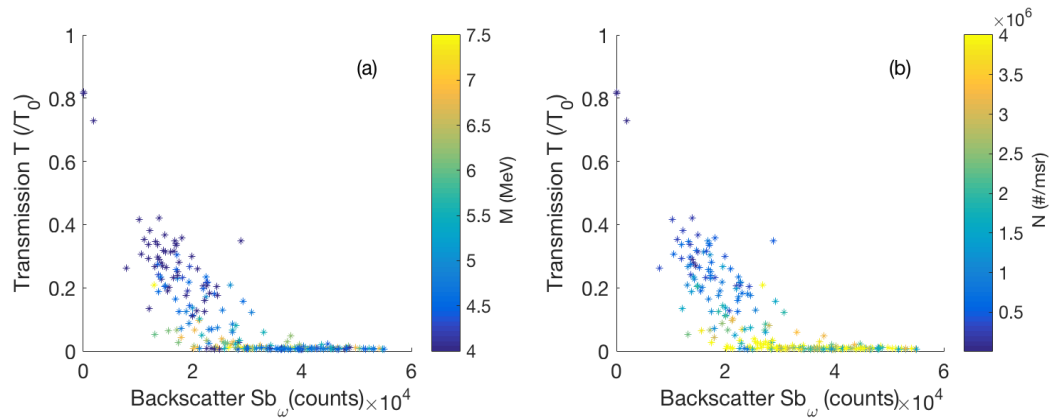


**Figure 4.22:** Transmission  $T$  as a function of backscatter signal  $Sb_\omega$  in the case where no parameters such as laser and target are distinguished. The color denotes the maximum kinetic energy  $M$  and the proton number  $N$  in (a) and (b), respectively.

It is nevertheless interesting to evaluate additional parameters. Through all data, transmission  $T$  and backscatter  $B$  behave inversely. Figure 4.22 supports this by plots all transmission values versus the respective backscatter signal. The color of the points represents the respective maximum kinetic energy  $M$  (a) and the number of protons  $N$  (b). High proton yield is strongly correlated with low transmission. Although the scatter in the data remains substantial in the presented study, it shows that backscattered and transmitted light diagnostics has high potential to serve as a complementary performance monitor for a laser-driven ion source.

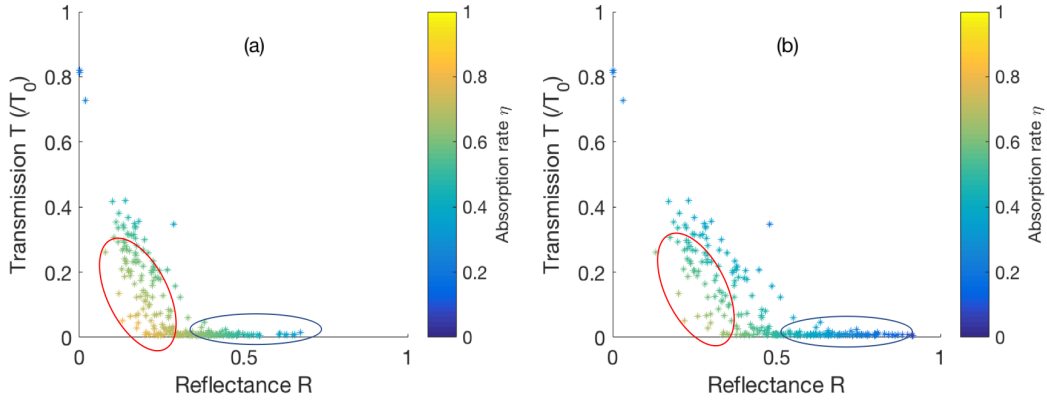


**Figure 4.23:** Absorption rate  $\eta$  (color) derived by Transmittance  $T$  and Reflectance  $R$ .  $R$  is the respective normalized  $Sb_\omega$  by  $Sb_\omega = 10 \times 10^4$  (a) and  $Sb_\omega = 6 \times 10^4$  (b).

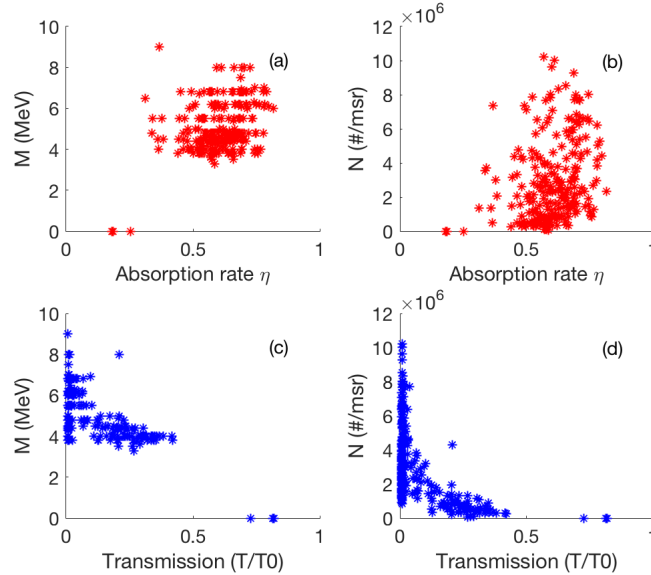


**Figure 4.24:** Maximum kinetic energy  $M$  as a function of Absorption rate (a) and Transmission (c); Proton number  $N$  as a function of Absorption rate (b) and Transmission (d).

**Absorption, Transmission and Reflection** Estimating a measure for energy absorption is instructive, because the efficiency of laser energy to particle energy conversion depends strongly on the amount of absorbed energy [137]. Even though our backscatter energy monitor was not absolutely calibrated, it is worthwhile to define an absorption of the laser light  $\eta = 1 - R - T$ , where  $R$  is now interpreted as the reflectance and  $T$  the measured transmittance. What we need to emphasize is that the back reflection here refers to the back-scattered light after potential redshift, which would lead to an additional reduction of backscattered energy. This effect is ignored here. It is also important to mention that the backscattered light that is not shifted is not observed in our diagnostic, because the special outcoupling mirror has very small transmittance in the region of the original laser spectrum. We rescale the highest observed backscatter signal  $Sb_\omega = 10 \times 10^4$  or  $Sb_\omega = 6 \times 10^4$  to 1 to ensure that  $\eta$  has values between 0

and 1. Regardless of which number is used to normalize the backscatter signal, the maximum value of the absorptivity  $\eta$  represented by the color in Figure 4.23 a and b always appears in the red circle region. Combining the blue circled area of Figure 4.23 with the corresponding area of Figure 4.22, maximizing  $\eta$  is not necessarily leading to the largest proton number. Figure 4.24 is another way to display the trend of maximum proton kinetic energy with absorptivity and transmittance.

The study shows that including complementary diagnostics for monitoring laser-driven ion sources can be meaningful. In our particular case, the instrumentation suite does not yet clarify the origin of fluctuations but hints that the limited temporal contrast of the laser pulse plays a key role and must be improved. Characterizing the transmitted and reflected/backscattered light bares the greatest potential for identifying optimal parameters for ion source operation. Judging by the remaining fluctuations that we observed, those parameters seem to remain disclosed, can vary from shot to shot and do not seem to reveal in standard measurements performed prior to the experiment or through monitoring main parameters such as laser energy and focus position.



## Chapter 5

# A new method of enhancing proton energy

As summarized in Section 1.3, the laser-ion conversion efficiency can be improved by suppressing the pre-pulse and ASE, or by MULTI-pulse coupling, or by target design or a combination. In this Chapter, a new approach based on an all-optical method to enhance proton energy will be demonstrated. It relies on a new concept for transient target miniaturization isolation by a specific additional Laguerre-Gaussian laser pulse. This chapter will explain the Laguerre-Gaussian (LG) beam, including generation methods, characteristics, and applications of this beam mode in section 5.1. Then, I will present an experiment based on a pre-pulse with such a LG-mode in Section 5.2. Simply stated, the pre-pulse is split from the main pulse, and it is modulated into a Laguerre-Gaussian beam as a tool for target pre-processing. Based on this, we proposed the concept of online target isolation. The specific physical image is as follows. At the surface of the target, the pre-pulse with Laguerre-Gaussian mode arrives nanoseconds prior to the main pulse and it interacts with the target first to create a plasma pre-expansion. Since the laser intensity at the center of the ring does not reach the target damage threshold, the pre-expanded annular thin plasma (density, temperature adjustable) separates the small micro solid target (with adjustable size) from the surrounding solid target. This all-optical method is in principle suitable for high repetition rate experiments to achieve online target pre-processing. The setup and experimental result will be presented in detail.

In order to study the expansion process of the low-temperature plasma (up to nanoseconds) after the interaction of the pre-pulse with the target and the subsequent interaction of the main pulse with the composite target, the numerical simulation is divided into two parts. The plasma pre-expansion process lasts for nanoseconds and the laser intensity is between  $10^{12} - 10^{15} \text{ W/cm}^2$ , consistent with the field of fluid dynamics simulation, in which the MULTI program is used to explore the evolution of the low-temperature plasma. This is explained in Section 5.3. In the last Section 5.4, the interaction of the main pulse with the composite target of the plasma cloud surrounding the solid small target is explored by Particle-in Cell (PIC) simulation.

## 5.1 Laguerre-Gaussian beam

Laguerre-Gaussian and Hermite-Gaussian laser beam modes are higher order modes of the Gaussian mode, which can be derived normally by solving the Helmholtz electromagnetic wave equation within the paraxial approximation [141, 142]. One also can use the plane wave representation of the fundamental Gaussian mode as seed function to derive all the other higher-order beam modes. The advantage of this method is that vector effects of the electromagnetic field are included and it can be extended to non-paraxial situations. In the scalar field approximation, any electric field amplitude distribution can be represented as a superposition of plane waves, the so called angular spectrum of plane waves [143],

$$E \propto \iint_{k_x^2 + k_y^2 \leq k^2} \frac{dk_x dk_y}{(2\pi)^2} A(k_x, k_y) \exp(ik_x x + ik_y y + iz \sqrt{k^2 - k_x^2 - k_y^2}), \quad (5.1)$$

where  $\vec{k} = (k_x, k_y, \sqrt{k^2 - k_x^2 - k_y^2})$  is the wave vector and  $A(k_x, k_y)$  is the amplitude of the plane wave. Equation 5.1 obeys the scalar wave equation,

$$\frac{\partial^2 E}{\partial x^2} + \frac{\partial^2 E}{\partial y^2} + \frac{\partial^2 E}{\partial z^2} + k^2 E = 0, \quad (5.2)$$

for the amplitude function  $E$ . The fundamental mode of a laser beam can be derived by minimizing the product of the divergence and the beam diameter, where the former is the spread of the plane wave amplitudes in wave vector space and the latter is the spread of the field intensity perpendicular to the  $z$ -direction and both of them are characteristics of the total energy flux. After mathematical derivation, one can deduce the electric field amplitude as [144],

$$E_0 = \frac{1}{w_0 \sqrt{1 + (z/z_R)^2}} \exp[ikz - \frac{1 - iz/z_R}{w_0^2(1 + (z/z_R)^2)}(x^2 + y^2) - i \text{atan}(z/z_R)], \quad (5.3)$$

which is also called **the fundamental Gaussian mode** due to the corresponding light intensity distribution having a Gaussian profile. Here,  $z_R = \pi w_0^2 / \lambda$  is the Rayleigh length,  $w_0$  is the beam waist and  $\lambda$  is the vacuum wavelength. The Gaussian beam is the mode with minimum uncertainty, which has the minimum dispersion for the same beam size.

By acting with differential operators (modulating the amplitude function  $A(k_x, k_y)$ ) on this fundamental solution, the standard form of **Laguerre-Gaussian modes** (LG modes) can be derived as [144],

$$E_{l,p}^L = \frac{e^{-ip\phi}}{w} \left( \frac{\sqrt{x^2 + y^2}}{w} \right)^2 L_l^p \left( \frac{2(x^2 + y^2)}{w^2} \right) \exp[ikz - \frac{x^2 + y^2}{w_0^2(1 + iz/z_R)} - i\Psi_{p,l}^L], \quad (5.4)$$

where  $w = w_0 \sqrt{1 + (z/z_R)^2}$  is the diameter of the Gaussian beam,  $l, p$  are some integers,  $\phi = \text{atan}(y/x)$  and  $\Psi_{p,l}^L = (p + l + 1) \text{atan}(z/z_R)$  is the Gouy phase. The definition of Laguerre's function is  $L_l^p(r) = \frac{e^r r^{-p}}{l!} \frac{d^l}{dr^l} (e^{-r} r^{p+l})$ . In fact, Laguerre-Gaussian modes are solutions in terms of polar coordinates and the rectangular geometry (or Cartesian coordinates) will lead to **Hermite-Gaussian modes** (HG modes), and the expressions of the two type modes can be

translated from ones to the others [145]. The standard form of the Hermite-Gaussian modes can be represented as,

$$E_{p,l}^H = \frac{1}{w} H_p(\sqrt{2}\frac{x}{w}) H_l(\sqrt{2}\frac{y}{w}) \exp[ikz - \frac{x^2 + y^2}{w_0^2(1 + iz/z_R)} - i\Psi_{p,l}], \quad (5.5)$$

where  $H_p(x)$  and  $H_l(x)$  are Hermite's polynomials that are defined uniformly as,

$$H_p(x) = (-1)^p \exp(x^2) \frac{d^p}{dx^p} \exp(-x^2). \quad (5.6)$$

The other variables are the same as those of LG modes. In order to have a perceptual understanding of these two modes, different modes with different orders are shown in Figure 5.1.

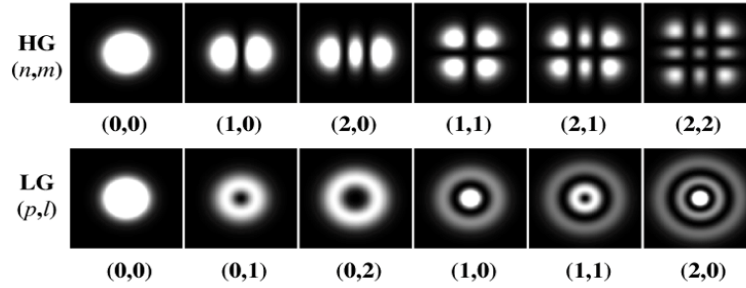


**Figure 5.1:** Hermite-Gaussian modes and Laguerre-Gaussian modes with different orders. [146]

The Laguerre-Gaussian beam can transfer orbital momentum to a particle, induce rotation around the propagation axis. It is also known as an **optical vortex** [147]. The essential feature of an optical vortex is the phase profile, given by  $\phi(r, \theta, z_c) = l\theta$ , where  $(r, \theta, z_c)$  are the cylindrical coordinates,  $r$  is the radial distance to the propagation axis,  $\theta$  is the angle,  $z_c$  is the path of the vortex core, and  $l$  is called "topological charge" which is a signed integer and the sign determines the direction of rotation. When a circle is made around the center, the phase of the electric field changes  $l \times 2\pi$ , so the phase is continuous anywhere except at  $r = 0$ . The phase at the center of the core is an indeterminate singularity, which is physically acceptable since the intensity disappears there.

Some examples of LG modes can be used as modes of pre-pulse for target miniaturization, i.e. modes with order (0,1) or (0,2) having a donut shape pattern, as shown in Figure 5.1. A pre-pulse with certain light intensity (higher than the target damage threshold) and carrying this donut-like LG mode can reduce a large-sized planar target that is much larger than the main pulse focal spot to a size comparable to it or even smaller. After the annular pre-pulse interacts with the target, the target beneath it is ionized. The resulting plasma expands. The density of the plasma is related to the rate of expansion and time. Hence, the intensity of the pre-pulse and the delay of the main pulse can be used to adjust the parameters of the plasma with which the main laser pulse interacts. In addition, the size of the focus ring is related to the order of the LG mode and the initial diameter of the beam.

In practice, the size of the central, ideally undisturbed target can be adjusted by selecting the mode of the LG light and the initial beam size. Changing the laser intensity and delay time can control the density and temperature of the ring-shaped plasma that forms around the central

target region. Using this method, we can obtain a new type of composite micro-suspended target. Its potential advantage is that the lateral hot electrons generated by the main pulse when interacting with the central part remain confined, so that the number and temperature of the hot electrons will increase, thereby increasing the charge separation field at the rear surface of the target [72, 148]. Accordingly, the ion energy and ion number emitted from the target are expected to increase.

### 5.1.1 Generation methods

#### Computer generated hologram (CGH)

A common method of generating optical vortices is a computer generated hologram [149] in which an optical vortex with a particular topological charge is built in a computer and then displayed in real time on a spatial light modulator (SLM). The SLM can spatially control the transparency to modulate the intensity of the beam by computer. It is also possible to produce a device that simultaneously adjusts the phase and intensity. The SLM can be divided into three categories, fixed SLM [150], electrically addressed SLM [151] and optically addressed SLM [152]. In the CGH method, it is desirable to generate the LG mode directly from the basic zero-order Gaussian mode or from the fundamental Hermite-Gaussian laser mode by introducing a Gouy phase shift [153]. Since the SLM allows reprogrammable waveform generation under computer control, it is also widely used in the ultra-short pulse shaping regime [154]. In amplified systems, the programmable pulse shaper can be placed either before [155] or after [156] the amplifier. However, placing it before the amplifier will lead to minimum danger of the damage to the SLM. Furthermore, in the case of saturated amplifier, the output energy does not strongly depend on the changes of the input energy. Therefore, energy losses by the pulse shaping process before the amplifier will not result in lower energies after amplification.

#### Spiral phase plate (SPP)

The spiral phase plate is a unique optical component whose structure consists entirely of spiral or helical phase steps, the purpose of which is to control the phase of the transmitted beam. After an SPP, the laser obtains an output with a screw-type wave-front dislocation and the subsequent far-field beam will exhibit a donut-like pattern. The SPP offers a direct method that allows a direct conversion of a Gaussian beam into a LG beam without changing the beam's propagation direction or requiring an HG laser source [157]. Historically, Nye and Berry introduced the concept of wavefront spirals and edge dislocations for the first time in 1974, initially trying to understand the radio echoes at the bottom of the Antarctic ice sheet and some analogous experiments were carried out with ultrasound waves [158]. Later on, the optical helix/ dislocation/ phase-singularity including bistability and optical switching of spatial patterns [159], the dynamics of optical vortices [160], the creation of topologically stable patterns [161] and the theory of propagation in nonlinear media [162] were studied and helped developing optical vortices further. The use of a spiral phase plate to produce a Laguerre Gaussian beam can be by transmissive or reflective methods. However, it is difficult to directly use the SPP to act on a laser pulse of relativistic light intensity. Recently, an SPP was inserted into the laser beam path in the early

stages of the laser amplification chain to produce a hollow beam with an intensity of  $> 10^{18}$  W/cm<sup>2</sup>.

### Comparison and other methods

Relatively speaking, the spatial-light-modulators allows a straightforward means of the LG beams and are rapidly re-configurable but they are quite expensive with moderate power efficiency and deficient resolution. The SPP has better efficiency and allows direct conversion of Gaussian beams into LG beams without changing the beam propagation direction. Furthermore, the SPP is made of glass material and can withstand high power laser illumination with low failure rate. Especially in explorative laser ion acceleration experiments, a simple and stable Laguerre-Gaussian beam is more valuable than variability.

#### 5.1.2 Characteristics and applications

The important feature of the LG beam or optical vortex is that it carries orbital angular momentum (OAM), whose orbital contribution is related to the spatial distribution of light intensity and phase and not to the polarization. The angular momentum density associated with the transverse electromagnetic field can be calculated by [163]

$$\vec{M} = \epsilon_0 \vec{r} \times (\vec{E} \times \vec{B}) \quad (5.7)$$

and the total angular momentum of the field is

$$\vec{J} = \epsilon_0 \int \vec{r} \times (\vec{E} \times \vec{B}) d\vec{r} = \vec{L} + \vec{S}, \quad (5.8)$$

where  $\vec{L}$  and  $\vec{S}$  represent the orbital angular momentum and spin angular momentum, respectively. Allen et al [164] started from the cylindrically symmetric solution  $u_{pl}(r, \phi, z)$  of the Laguerre-Gaussian beams to describe the distribution of the field amplitude satisfying the wave equation in the paraxial approximation,

$$u_{pl}(r, \phi, z) = \frac{C}{(1+z^2/z_R^2)^{1/2}} \left(\frac{r\sqrt{2}}{w(z)}\right)^l L_p^l\left(\frac{2r^2}{w^2(z)}\right) \times \exp\left(\frac{-r^2}{w^2(z)}\right) \exp\left(\frac{-ikr^2z}{2(z^2+z_R^2)}\right) \exp(-il\phi) \times \exp\left(i(2p+l+1)\text{atan}\frac{z}{z_R}\right), \quad (5.9)$$

where  $z_R$  is the Rayleigh range,  $w(z)$  is the radius of the beam,  $L_p^l$  is the associated Laguerre polynomial,  $C$  is a constant. Then, as the linear momentum density, the time average of the real part of  $\epsilon_0 \vec{E} \times \vec{B}$  given by

$$\frac{\epsilon_0}{2} (\vec{E}^* \times \vec{B} + \vec{E} \times \vec{B}^*) = i\omega \frac{\epsilon_0}{2} (u^* \vec{\nabla} u - u \vec{\nabla} u^*) + \omega k \epsilon_0 |u|^2 \vec{e}_z. \quad (5.10)$$

Substituting the formula 5.9 into the formula 5.10, the momentum density per unit power is obtained,

$$\vec{P} = \frac{1}{c} \left( \frac{rz}{z^2 + z_R^2} |u|^2 \vec{e}_r + \frac{l}{kr} |u|^2 \vec{e}_\phi + |u|^2 \vec{e}_z \right), \quad (5.11)$$

where  $\vec{e}_\phi$ ,  $\vec{e}_r$  and  $\vec{e}_z$  are unit vectors. The  $\vec{e}_r$  and  $\vec{e}_\phi$  components relates to the spread of the beam and the orbital angular momentum, respectively. The  $\vec{e}_z$  component relates to the linear momentum in the propagation direction. Finally, the time averaged angular momentum density,  $\epsilon_0 \vec{r} \times (\vec{E} \times \vec{B})$ , per unit power yields

$$\vec{M} = -\frac{l}{\omega} \frac{z}{r} |u|^2 \vec{e}_r + \frac{r}{c} \left( \frac{z^2}{z^2 + z_R^2} - 1 \right) |u|^2 \vec{e}_\phi + \frac{l}{\omega} |u|^2 \vec{e}_z. \quad (5.12)$$

Due to the symmetry of the radial and azimuthal components about the axis, the integration over the beam profile leaves only the  $\vec{e}_z$  component. Therefore, the Laguerre-Gaussian beam possesses a well-defined orbital angular momentum  $\vec{M}_z$ , which satisfies  $\vec{M}_z / \vec{P}_z = l(\lambda/2\pi)$ .

About the applications, the orbital angular momentum of light can be transferred to the appropriate material particles that are captured, causing them to rotate [165]. This property has important applications in micro-manipulation and micro-mechanical design and operation, e.g. to control the transverse orientation of small transparent isotropic particles in optical tweezers [166]. Light containing optical vortices can also be used to image and detect different kinds of physical and biological properties of matter [167]. This concept also applies to single photons in the quantum world; there, it can be used to encode quantum information carried by the corresponding photon states [168].

In the field of laser electron acceleration, Zhang et al [169] studied the acceleration and evolution of the hollow relativistic electron beam in the laser wake field driven by LG laser pulses. The LG laser pulse with its ring intensity distribution produces a ring-shaped wake field. A portion of the angular momentum of the LG laser is transferred to the injected electrons and the angular momentum will cause the electrons to rotate in the wake field. Brabetz et al [170] achieved a hollow proton beam based on a hollow high-intensity laser beam in the regime of target normal sheath acceleration. Although the power scaling of the maximum proton energy with increasing laser intensity in the LG spot is steeper than that of Gaussian [170], the laser intensity of LG spot is lower than that of Gaussian spot since it has a larger focal area. Therefore, the simple use of the LG laser mode did not enhance the maximum proton energy.

## 5.2 Proton energy enhancement based on LG prepulse

### 5.2.1 Experimental setup

As illustrated in Figure 5.2, in the early stage of the laser amplification chain, the original beam is split by a beam splitter  $S_1$  (with a transmittance to reflectance ratio 9/1) into a pre-pulse and a main pulse, which are then coaxially overlapped by another beam splitter  $S_2$  (with the same ratio as  $S_1$ ) with a temporal delay 1.7 ns determined by the delay distance  $D$ . Before the overlap, the pre-pulse is transmitted continually through several neutral density filters (NDFs) and a spiral phase plate (SPP). The combination of NDFs is to manipulate the pre-pulse energy and the SPP is to introduce a spiral wavefront to the pre-pulse. Applying a SPP to a coherent beam in the near field results in an optical vortex beam in the far field, where exhibits a characteristic donut-shaped transverse profile. An integer number of  $2\pi$  phase accumulation around one turn of the spiral wavefront corresponds to the azimuthal index  $l$  of the Laguerre-Gaussian mode ( $LG_{p,l}$ ),

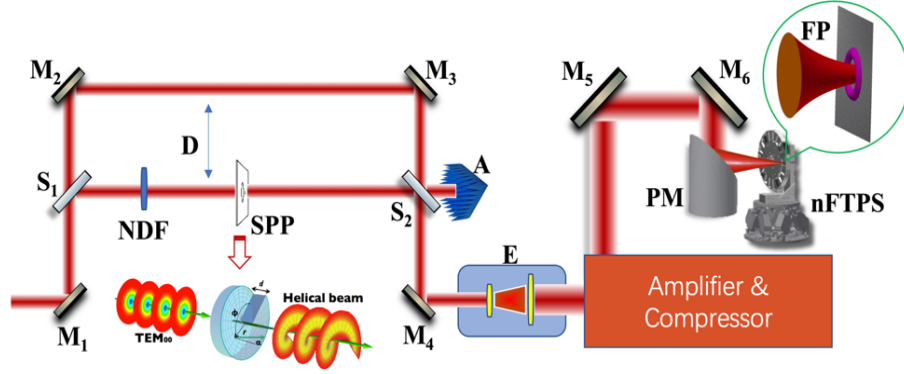


**Figure 5.2:** Schematic of the experimental setup.  $M_1 \sim M_6$  - mirrors.  $S_1, S_2$  - beam splitters ( $T/R = 9/1$ ). NDFs - neutral density filter. SPP - spiral phase plate.  $D$  - delay distance ( $0.25\text{ m}$ ).  $A$  - absorber.  $E$  - beam expander. PM - parabolic mirror ( $f/3.75$ ).  $nFTPS$  - nano foil target positioning system [25].  $FP$  - focal pattern of the pre-pulse (purple) and the main pulse (red) on the target surface (black). Energies of the main pulse and the pre-pulse (without NDFs) after the last amplifier are  $2.8\text{ J}$  and  $0.2\text{ J}$ , respectively.

which also equals to the topological charge of the SPP. With the radial mode index  $p = 0$ ,  $LG_{p=0,l}$  mode is azimuthally symmetric in magnitude and the intensity vanishes at the center due to the phase singularity. In cylindrical coordinates, the spatial laser intensity distribution on target can be described by [80]

$$I_{LG}(r) \propto \left(\frac{\sqrt{2}r}{\omega_0}\right)^{2l} (L_0^l(2\frac{r^2}{\omega_0^2})) \exp(-2\frac{l^2}{\omega_0^2}), \quad (5.13)$$

where  $r$  is the radial distance,  $L_0^l$  is the associated Laguerre polynomial and  $\omega_0$  is the beam waist at position  $z = 0$ . The radius of the maximum intensity,  $r_{max}$  of such mode is then given by

$$r_{max} = \sqrt{\frac{z_R l}{k}} = \omega_0 \sqrt{\frac{l}{2}}, \quad (5.14)$$

where  $z_R$  is the Rayleigh range and  $k$  is the wave number. Therefore, one can easily estimate the ring size of the pre-pulse based on the topological charge of SPP and the beam waist in the case of a monochromatic beam at frequency  $\omega_0$ .

After the overlap of the two pulses, the beam is expanded by two beam expanders (only one is plotted in Figure 5.2), amplified by the last amplifier and then temporally compressed in a grating compressor. Guided by the beamline and focused by the parabolic mirror (PM), an energy-adjustable Laguerre-Gaussian mode pre-pulse reaches the target surface  $1.7\text{ ns}$  prior to the Gaussian main pulse, as shown in the inset plot  $FP$  of Figure 5.2. Consequently, the main pulse interacts with a composite target (a central, nearly undisturbed foil-like target surrounded by a ring shaped plasma that has expanded for  $1.7\text{ ns}$ ).

### 5.2.2 Experimental result and discussion

In the experiment, the main pulse was focused to a spot of FWHM of  $6.2\ \mu\text{m}$ , in  $p$  polarization at  $10^\circ$  angle of incidence resulting in a peak intensity of  $8 \times 10^{19}\text{ W/cm}^2$  on the target surface.

Without NDFs in the beamline, the initial peak intensity of the pre-pulse was  $1.6 \times 10^{18} \text{ W/cm}^2$  on target. The level of the amplified spontaneous emission (ASE) was measured to be  $10^{-10}$  and  $10^{-6}$  of the peak laser intensity at  $100 \text{ ps}$  and  $5 \text{ ps}$  prior to the peak of the pulse, respectively. The targets were planar plastic foils with constant thickness ( $2 \mu\text{m}$ ), positioned and delivered by the *nFTPS* (though the experiment was operated in shot on demand mode and not in high-repetition rate mode). The ion diagnostic was a Thomson parabola spectrometer with a magnetic field of  $0.3 \text{ T}$  over a length of  $48.5 \text{ mm}$ , and an electric field could be varied in the strength from  $400$  to  $7000 \text{ V/mm}$  over a distance of  $250 \text{ mm}$ .

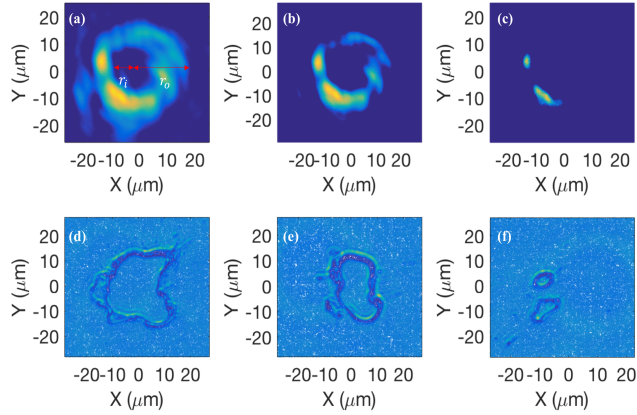


**Figure 5.3:** Focal patterns of pre-pulses with different contour-intensity-backgrounds ( $I_a > 8I_{th}$  (a),  $I_b > 4I_{th}$  (b), and  $I_c > I_{th}$  (c)) and the corresponding hole photos on plastic targets after shot with such pre-pulses. For example, (d) indicates that a roughly  $20 \mu\text{m}$ -radius hole is produced by a donut-shaped pre-pulse in case (a).  $r_i$  is the radius of QIMT at the arrival time of the main pulse and  $r_o$  is outer edge radius of the pre-plasma.

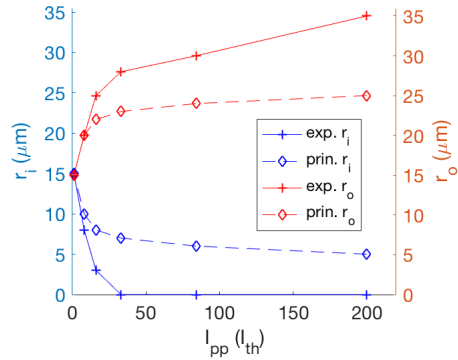


**Figure 5.4:** The size  $r_i$  and  $r_o$  at the arrival time of the main pulse as a function of  $I_{pp}$ . The solid lines show the trends of  $r_i$  (blue) and  $r_o$  (red) estimated from the pre-pulse intensity profile; the dashed lines show the trends of  $r_i$  (blue) and  $r_o$  (red) for an ideal LG-mode pre-pulse.

We created the optical vortex by inserting a 20-mm-diameter 1-mm-thick silica SPP in the pre-pulse beam path. This 64-stair-step SPP was designed to induce a spiral phase with a  $l \times 2\pi$  variation per azimuthal turn at the central laser wavelength of  $800 \text{ nm}$ . Figure 5.3 (d-f) show example images of the hole in the target foil after being single pulse irradiation with only the pre-pulse at varying intensity between  $1.9 \times 10^{14}$ ,  $9.6 \times 10^{13}$  and  $2.4 \times 10^{13} \text{ W/cm}^2$ . When the peak intensity of the pre-pulse  $I_{pp}$  in the ring dropped below  $2.4 \times 10^{13} \text{ W/cm}^2$ , no damage was

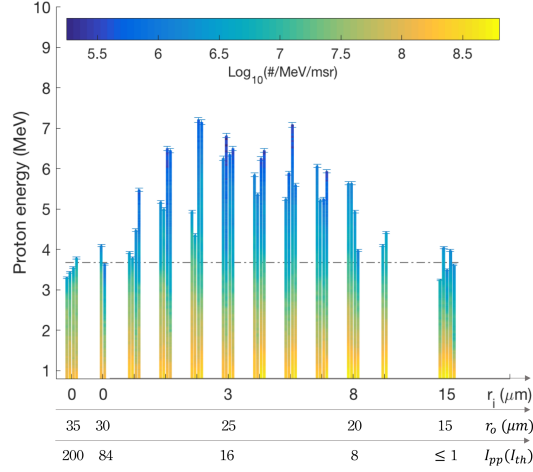


**Figure 5.5:** (a) Experimentally measured proton spectra (logarithmic color coded) as a function of transverse radius  $r_i$  of inner (non-disturbed) target (upper x-label), the radius of ring boundary  $r_o$  (middle x-label) and LG pre-pulse intensity  $I_{pp}$  (lower x-label). The dashed dotted line represents maximum energy without LG pre-pulse.

observed. We define it as the damage threshold intensity  $I_{th}$ . The other two example intensities can then be expressed as  $8I_{th}$  and  $4I_{th}$ . By comparing these three subfigures (d-f), it can be seen that as the intensity of the pre-pulse increases, the size of the hole left on the target becomes larger. This is well understood because the target will be ionized if the laser intensity is above its damage threshold. As we mentioned in case of femtosecond pulses, all regions throughout the laser beam profile with sufficient intensity for multiphoton ionization will be removed resulting in extremely fine control of the position of material removal. Although we only observe the outer boundary of the whole, the clear edge and close resemblance of the shape to the related intensity distributions that are shown in Figure 5.3 (a-c) is obvious. We therefore argue that for a short time, the central part of the foil remains largely intact and forms a quasi-isolated micro-target (QIMT). The radius  $r_i$  of QIMT at the arrival time of the main pulse can be estimated by measuring the representative transverse size of the two contour lines where the experimentally measured LG-mode, when scaled to maximum intensity,  $I_{pp}$ , crosses the threshold intensity  $I_{th}$ . The sizes  $r_i$  and  $r_o$  associate with  $I_{pp}$  and the trends are shown in Figure 5.4. The solid lines were extracted from the measured LG-mode intensity profile and dashed lines were derived from an ideal LG-mode. Due to the uneven distribution of the intensity of the pre-pulse, the pre-pulse with an intensity of just above  $I_{th}$  will not generate a QIMT, as shown in Figure 5.3(c) and Figure 5.3(f). When the intensity of the pre-pulse is bigger than  $30I_{th}$ , the size  $r_i$  becomes zero (solid blue line in Figure 5.4), which was due to the small spatial contrast in the measured LG-mode.

The proton spectra, i.e. number of protons per MeV and msr (logarithmically color-coded) as a function of kinetic energy (vertical axis) are presented in Figure 5.5. The main pulse intensity was kept constant within a typical shot to shot fluctuation (7%). The LG pre-pulse intensity was varied via pre-pulse energy and is represented on the lower horizontal axis. The estimated  $r_i$  and  $r_o$  from the intensity contour lines corresponding to the pre-pulse intensity are marked in the upper and middle x-labels.

As expected, at pre-pulse intensities below the plasma formation threshold we do not see the

influence of the pre-pulse intensity on proton spectra. When the pre-pulse intensity rises significantly above the threshold, both maximum proton energy and spectral amplitude increase. Proton emission is stronger and more energetic for a rather wide range of  $I_{pp}$  between 8 and  $20I_{th}$ . At pre-pulse intensities beyond  $30I_{th}$  ( $7.2 \times 10^{14} \text{ W/cm}^2$ ), proton energy and number drop significantly, in particular, proton number becomes lower than without pre-plasma. This is likely because of a pre-plasma that is excited in the central area due to the imperfect LG-mode that is not truly zero in the center. In other words,  $r_i(> 30I_{th}) = 0$ . Because the plasma in the center is excited 1.7 ns before the main pulse arrives, the reduced density gradients at the target surfaces result in reduced proton acceleration performance [61].

It is worthwhile to recall the physical image of the target normal sheath acceleration (TNSA) mechanism here. After ionization of the target, some hot electrons are transported in the longitudinal direction and reach the back side of the target where they set up a strong field that accelerates ions but also reflects the majority of electrons back into the target. The hot electrons can also move along the vacuum-target surface and this way their kinetic energy spreads over a wide region ( $> 100 \mu\text{m}$ ), resulting in the attenuation of the electric field [171, 172]. Therefore, reducing the lateral dimension of the target, i.e., achieving a mass-limited target, can effectively prevent the transfer of energy from the hot electrons to a distant location because the hot electrons remain macroscopically bound to the center of the target [70]. Theoretical and experimental studies have reached a consensus that the optimal result of laser-accelerated ions occurs when the size of the target is comparable to or smaller than the size of the laser focal spot, which also depends on the pulse duration and target shape [72, 70, 173]. The QIMT provided by the donut-shape pre-pulse seems to indicate such an enhancement that is expected from this simple picture. The difference is that the QIMT is surrounded by a thin plasma cloud. The size of the QIMT can be estimated, but the density distribution of the plasma cloud around it at the time when the main pulse arrives is inaccessible. Therefore, we carried out fluid dynamics simulation with the software MULTI-1D and MULTI-2D to study the evolution of the plasma expansion that is triggered by the interaction of the LG-pre-pulse.

In brief, the LG-pre-pulse can enhance the ion energy and number. However, the understanding of the underlying physics requires the support of the following simulations and modeling.

## 5.3 The interaction between LG prepulse and target

### 5.3.1 Introduction of MULTI program

The MULTI simulation program is a series of calculation programs based on the radiation hydrodynamics method developed by R. Ramis et al. It solves the evolution of plasma by solving fluid mechanics equations and radiative transport equations to describe the state of the plasma by macroscopic physical quantities such as particle temperature, density, pressure, and ionization rate. According to different needs, the MULTI program is now available in different versions such as 1D, 2D [174], 3D, MULTI-fs [175], and MULTI-IFE [176]. The user writes the main program for a specific problem and calls various subroutines integrated into the library, such as fluid mechanic's subroutine, energy deposition subroutine, radiation transport subroutine, etc., to complete the solution process. The program uses mass coordinates and assigns an ionic ar-

tificial viscosity to eliminate singularities. In terms of plasma models, electrons and ions have the same velocity, and their number density always keeps the plasma electrically neutral. The heat transfer model uses the electronically thermally conductive Spitzer formula to calculate the heat transfer coefficient and limits the maximum heat flux through the free-streaming limit. In terms of radiative transport, frequency and direction, grouping methods are used for the discrete equation. The laser energy deposition uses an inverse bremsstrahlung absorption model.

In this section, 1D and 2D simulations are described which were performed by Shirui Xu (from Peking University) through MULTI-IFE and MULTI-2D, respectively. The main reason is that the MULTI-IFE code is more elaborate, using two-fluid equations to distinguish between electrons and ions. The MULTI-2D code does not distinguish between electrons and ions, and is relatively rough, but can make up for the shortcomings of one-dimensional simulation, that is, the spatial information of the plasma cannot be given. Therefore, when the results of the two simulations are combined, reasonable information about the distribution and temperature of the plasma around the QIMT and the size of the QIMT can be given.

### 5.3.2 1D simulation with MULTI-IFE

One-dimensional simulation refers to considering only the expansion process of the plasma in the laser direction, ignoring the information in the lateral direction. The lateral evolution of the QIMT, which is estimated by the two-dimensional simulation in Section 5.3.3.

**Target parameters** The target material is polystyrene with average atomic weight  $A = 6.510$  and average nuclear charge  $Z=5.280$ . The initial density is  $\rho_0 = 1.2 \text{ g/cm}^3$  and the initial thickness is  $d_0 = 2 \text{ }\mu\text{m}$ . The critical number density of electrons for a certain wavelength  $\lambda_L$  can be calculated as  $n_c = 1.1 \times 10^{21}/(\lambda_L(\mu\text{m}))^2/\text{cm}^3$  and the initial electron number density of polystyrene at full ionization is

$$n_e \approx 227n_c. \quad (5.15)$$

**Laser parameters** The central wavelength of the laser is  $\lambda_L = 800\text{nm}$  and the pulse duration is  $\tau = 30\text{fs}$ . The time profile of the intensity is represented by the  $\sin^2$  function,  $I(t) = I_0 \sin^2(-\frac{\pi t}{2\tau})$ , because the Gaussian function is not included in MULTI-IFE.

In the experiment, we used different LG intensities to generate ring-shaped plasmas of different sizes and densities. The specific intensity parameters are shown in Table 5.1. Among them, the second column is the relative light intensity in units of  $I_{th} = 2.4 \times 10^{13} \text{ W/cm}^2$ , which is the coarse damage threshold of the target material of polyvinyl alcohol. Since the data of polyvinyl alcohol is not included in MULTI-IFE, it is replaced by the material of polystyrene in the simulation.

**The control parameters** Initial time-step is  $dt_{initial} = 1\text{fs}$ , the maximum time step is  $dt_{max} = 10\text{ps}$ . The whole area is split into 400 grid cells evenly.

Case	Intensity ( $I_0/(I_{th})$ )	Intensity $I_0/(W/cm^2)$
1	0.1	2.4e+12
2	1	2.4e+13
3	3	7.2e+13
4	5	1.2e+14
5	6	1.44e+14
6	8	1.92e+14
7	13	3.12e+14
8	16	3.84e+14
9	28	6.72e+14
10	33	7.92e+14
11	84	2.02e+15
12	100	2.4e+15
13	150	3.6e+15
14	200	4.8e+15
15	250	6.0e+15
16	300	7.2e+15

**Table 5.1:** The intensities of LG pre-pulses for scanning

The evolution of plasma expansion in longitudinal direction

Taking light intensity  $I = 9.27 \times 10^{15} W/cm^2$  as an example, we take the density curve of the target in the longitudinal direction to study the plasma expansion process, as shown in Figure 5.6. As can be seen from Figure 5.6 (a-i), the laser and target interaction process can be divided into three stages: 1, laser energy deposition process(a-b); 2, density peak wave propagation stage (c-e); 3, plasma expansion stage with the density distribution shape solidified (f-i). In the first stage, there is no significant change in the density distribution of the target during the laser incidence. At around 30 fs, the front surface of the target is slightly inflated (b)). In the second stage, after about 2 ps, a density spike appears on the front surface of the target because the target front surface plasma compresses the target as it expands forward, resulting in an increase in density (c)). At the same time, the back surface of the target has begun to expand (see (c-d)). The density spike propagates like a wave until it reaches the back surface of the target (d-e)). At about 50 ps, the target is fully ionized and the density at the back surface is higher than that of the front surface (e)). In the third stage, from about 100 ps to 5 ns, the plasma density distribution shape has stabilized, but as time goes on, the plasma expands to both sides and the corresponding density peak expands to a flat top (f-i)). We can see that at 2 ns, the plasma density flat top is  $> 10 mg/cm^3$ , which is 3 times the critical density value  $\rho_0 = 3.6 mg/cm^3$ . At this point, the length of the plasma with a density  $> 10 mg/cm^3$  is already close to  $150 \mu m$  (h)). At 5 ns, the plasma density peak is further reduced to  $\sim 10 mg/cm^3$ , while the longitudinal length is already  $> 300 \mu m$  (i).

In fact, this density spike can be explained by shock waves. In 2007, Lundh et al. [177] studied the influence of shock waves driven by amplified spontaneous emission (ASE) with a 3 ns long pedestal. The intrinsic ASE ionizes the target and heats the plasma formed on the front side of the foil. As the plasma expands into the vacuum, it also exerts a huge pressure on the

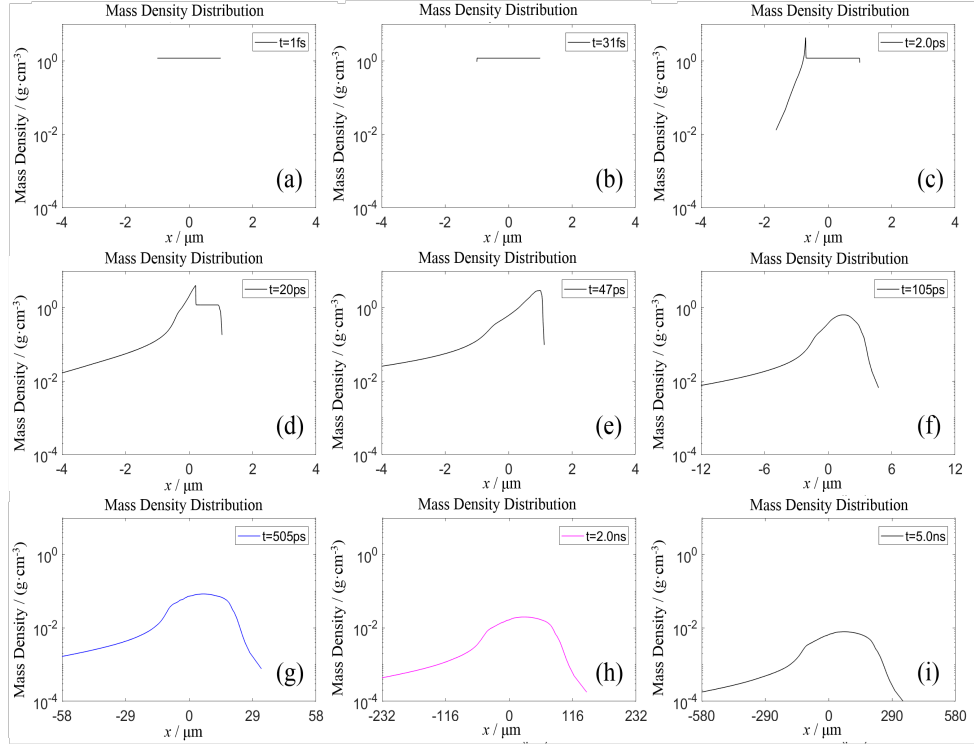


**Figure 5.6:** The evolution of plasma density in case of intensity of  $9.27 \times 10^{15} \text{ W/cm}^2$

remaining target. Along with this pressure effect, a shock wave is generated and propagates into the target at a constant speed. According to the mass and momentum conservation laws and an experimentally validated linear relationship, the shock and particle velocities  $v_{shock}$ ,  $v_{particle}$  can be solved [177],

$$v_{shock} = \frac{c_s}{2} \left( \sqrt{1 + \frac{\alpha}{\rho_0 c_s^2} P} + 1 \right), \quad (5.16)$$

$$v_{particle} = \frac{c_s}{2\alpha} \left( \sqrt{1 + \frac{\alpha}{\rho_0 c_s^2} P} - 1 \right), \quad (5.17)$$

where  $c_s$  is the sound velocity in the material,  $\alpha$  is an experimental material constant.  $P = \kappa I^{2/3}$  is the pressure in Pa,  $I$  is the intensity in  $\text{W/m}^2$  and  $\kappa$  is a material specific constant related to the wavelength of the laser. We plotted the movement speed of the density peak relative to the light intensity, as shown in Figure 5.7. The speed of the density peak (black dot) matches the scaling law of the shock wave as a function of the laser intensity, as the red dashed line shows, which is a fitting curve. Assuming that  $\kappa = 1$ , then the other parameters  $c_s = 3.3 \text{ } \mu\text{m/ns}$ ,  $\alpha = 1.69$  can be obtained, which are close to the plastic parameters in the reference [177]. For comparison, the scaling law of ion acoustic wave velocity as a function of light intensity  $v_{acoustic} \propto \sqrt{\frac{T_h}{m_i}} \propto I_0^{1/6}$  is indicated by a dashed blue line in Figure 5.7, in which  $m_i$  is the ion mass and the hot electron energy  $T_h \propto I_0^{1/3}$  is due to the dominant resonant absorption [178]. It can be seen that although we used a pulse with a short duration of 30fs, the density peak generated by the pressure can be explained well by the shock wave model.

When the shock wave reaches the target rear it will be reflected, causing the shock wave to break.

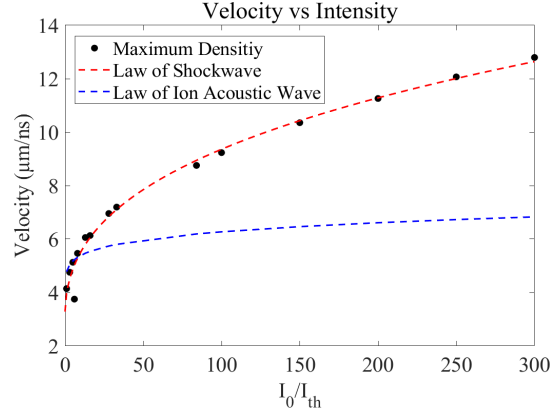


**Figure 5.7:** The scaling laws of density peak (shock) velocity against the laser intensity.

Then, the whole target (plasma) starts to expand to both sides at a certain velocity. Here, we define the plasma expansion velocity  $v_{exp} = \frac{d_{FWHM}}{dt}$  as time-varying rate of full width at half maximum (FWHM) of the mass density curve, which is plotted in blue dashed line in Figure 5.8. We see that the plasma expansion velocity does not change much in the intensity range  $0.1I_{th} \sim 3I_{th}$ , where it is lower than the thermal velocity that arises because MULTI treats the solid target as a fluid even if it is not ionized. In case of higher intensity ( $> 3I_{th}$ ), the expansion speed and the intensity satisfy the following functional relationship [179],

$$v_{exp} = A\sqrt{I_0/I_{th}} + B, \quad (5.18)$$

where the unit of velocity is  $\mu m/ns$ , and the constants are  $A = 3.0 \mu m/ns$  and  $B = -4.4 \mu m/ns$ , respectively. This simple model allows one to estimate the density and longitudinal (i.e. in laser propagation direction) extend of the the ring plasma at a certain delay time.

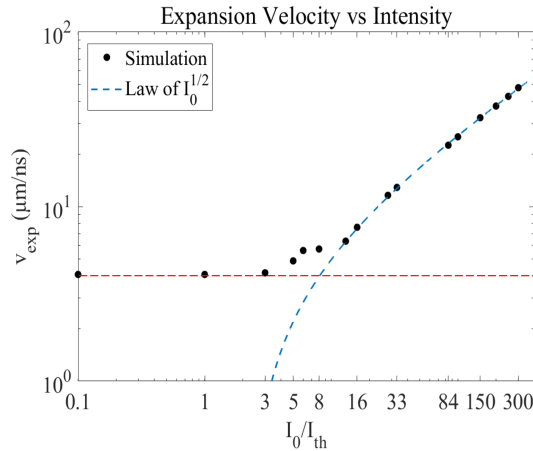


**Figure 5.8:** The scaling law of expansion velocity against the laser intensity.

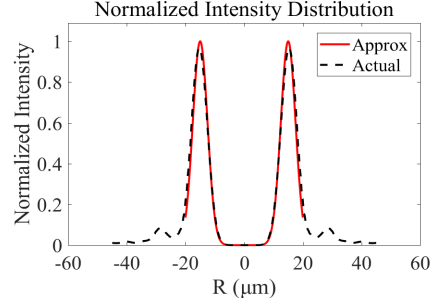


**Figure 5.9:** The real Laguerre-Gaussian mode with higher order rings (black dashed line) and the mode used for simplification in the simulation (red line)

### 5.3.3 2D simulation with MULTI-2D

Through one-dimensional simulation, we understand the expansion process of the plasma generated by the laser with a pulse width of 30fs and the laser intensity in the range of  $I_{th} \sim 300I_{th}$ . Based on the analytical or empirical model, we can infer the plasma density distribution in longitudinal direction at a specific time. However, because the 1D simulation cannot give the lateral density distribution and the specific size of the QIMT and the longitudinal extend is larger (100  $\mu m$ ) than the expected transverse size ( $\sim 10 \mu m$ ), we performed the following simulation with the MULTI-2D program in the cylindrical coordinate system.

**Target parameters** The target material is polystyrene with average atomic weight  $A = 6.510$ , average nuclear charge  $Z=5.280$ . The initial density is  $\rho_0 = 1.2 g/cm^3$  and the initial thickness is  $d_0 = 2 \mu m$ . The critical mass density is  $\rho_0 = 3.6 mg/cm^3$  as function 5.15. The lateral dimension for calculation is set as 2 cm.

**Laser parameters** The central wavelength of the laser is  $\lambda = 800 nm$  and the pulse duration is  $\tau = 30 fs$ . For the real  $LG_{p=0,l}$  mode, the strong ring is its first order ring, and in addition, there are second and higher order rings with decreasing strength, as the black dashed curve shows in Figure 5.9. For simplification, the mode was replaced by the red curve, whose intensity distribution satisfies,

$$\frac{I(r, t)}{I_0(t)} = \exp\left[-\frac{2(r - r_3)^2}{\omega^2}\right], \quad (5.19)$$

where  $r \in [r_1, r_2]$  is the radial coordinate,  $r_1 = 20 \mu m$  is the outer radius and  $r_2 = 10 \mu m$  is the inner radius.  $r_3 = (r_1 + r_2)/2 = 15 \mu m$  and  $\omega = (r_2 - r_1)/2 = 5 \mu m$  are the intermediate radius of the ring and the half-width of the ring, respectively.

As mentioned in Section 5.3.2, we used the same  $\sin^2$  function as the time profile curve,

$$P(t) = P_0 \sin^2\left(\frac{\pi t}{2\tau}\right), \quad (5.20)$$

where  $P_0 = I_0 A = I_0 \pi (r_2^2 - r_1^2)$  is the input peak power and A is the area of the focus. In the 2D simulation, the intensities are the same as those in the one-dimensional simulation, and the corresponding powers are shown in Table 5.1.

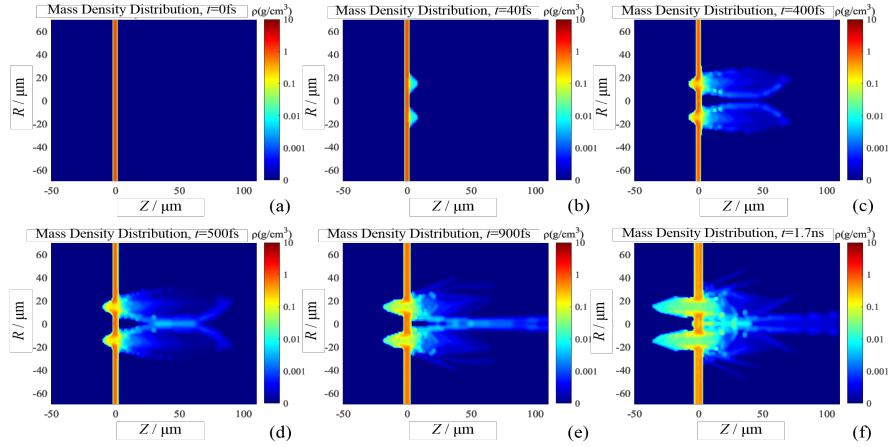


**Figure 5.10:** The evolution of plasma density in case of  $25I_{th}$ . (a)-(f) are the mass density distributions at 0, 40 ps, 400 ps, 500 ps, 900 ps and 1.7 ns, respectively. Laser impinges from the right.

**The control parameters** Initial time-step is  $dt_{initial} = 1 fs$ , the maximum time step is  $dt_{max} = 10 ps$ . Only the upper part of the symmetry axis is considered. In the R direction, the region  $0 - 70 \mu m$  is divided into 30 grid cells, and the region  $70 \mu m - 2 cm$  is divided into 10 grid cells to get a result with a high resolution in the center region. In total, the grid number is 1200.

**The evolution of plasma expansion in 2 dimensions** Figure 5.10 shows the density distribution of the plasma at different times in case of intensity  $I = 6 \times 10^{14} W/cm^2$  ( $25I_{th}$ , the case that is most relevant for the comparison of the enhancement observed in experiments in section 5.2.2). At 40 ps, a plasma of approximately  $10 \mu m$  was observed in front of the target and the target back remained unchanged. At 400 ps, the plasma in front of the target expands to about  $70 \mu m$  towards the laser, and the plasma at the back surface is about  $10 \mu m$  long. It can be seen that the longitudinal expansion speed is faster than the lateral expansion speed. Over time, the toroidal plasma (here showing the two plasma bunches in 2D) interplayed outside of 50 microns, resulting in a plasma column on the axis (Figure 5.10(d-e)). At 1.7 ns, a small undisturbed region with a diameter of about  $20 \mu m$  (the QIMT) is surrounded by a toroidal plasma with a low-density. In addition, a plasma cloud has formed on the axis.

At  $R = 0 - 2 \mu m$  and along Z-axis, averaging the mass density leads to a 1D distribution of the plasma and the plasma state in front of QIMT which is shown in Figure 5.11. As time goes by, the plasma density in front of QIMT increases because of the transverse expansion of the ring plasma towards the laser. At 1.7 ns, the slight reduction of the mass density at  $Z=0$  is due to the thermal expansion mentioned before. In reality, the area below the damage threshold should not be affected. The effect of a plasma cloud in front of QIMT that is apparent in Figure 5.11 with PIC simulation. The near critical plasma leads to self-focusing of the main laser and yields slightly higher proton energies, but cannot explain the drastic increase that was observed in experiments. that the proton energies were slightly increased, mainly due to self-focusing. Therefore and to simplify treatment, we consider the effect of the toroidal donut plasma separately which we describe with a simple model in the following sections.

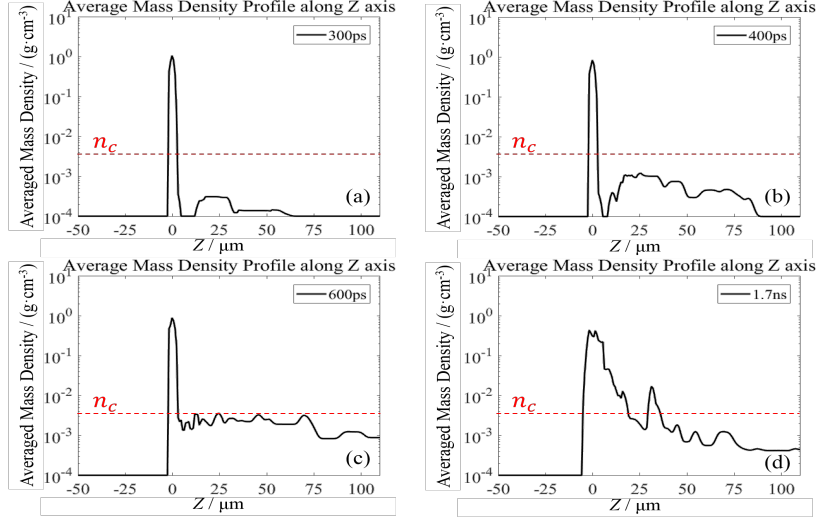


**Figure 5.11:** The evolution of average plasma density at Z-axis in case of  $30I_{th}$ . (a)-(d) are the mass density distributions at 300 ps, 400ps, 600 ps and 1.7 ns, respectively

Before we move on, Figure 5.12 shows for completeness the density distributions at 1.7 ns for 16 different laser intensities (the same cases in Table 5.1). From (a)-(g), the transverse expansion velocity is so small that the plasma does not reach the axis. From (h)-(o), an obvious plasma column is formed in front of the QIMT and around it a ring plasma cloud with a small density was observed, which separated the QIMT from the whole foil and the diameter of the QIMT depends on the intensity profile of the LG mode. The plasma state around the QIMT can be controlled via delay between the main-pulse and the pre-pulse. Combined with the expansion velocity as a function of laser intensity, one can coarsely predict the plasma density distribution at a certain time and, importantly, estimate the diameter of the QIMT.

### 5.3.4 Comparison of 1D and 2D MULTI results

Here, we compare the simulation results of MULTI-IFE with the results obtained by MULTI-2D. As shown in Figure 5.13, the plasma density distribution curve obtained by 1D simulation of MULTI-IFE (red curve) and the 1D density distribution curve extracted from MULTI-2D result at the maximum intensity (i.e.  $\frac{r_i+r_o}{2} = 15 \mu\text{m}$ ) are plotted in the same figures at three time instants. It can be seen that both the two-dimensional and one-dimensional results can capture the shock wave (Figure 5.13(a)). In general, the two-dimensional simulation results show a more intense and faster expansion and the density decreases more quickly than that of the 1D results. This is because there is one more degree of freedom. But the processes and trends obtained in the two cases are similar.

In brief, the interaction between LG prepulse and target was studied by 1D and 2D MULTI simulations. The shock wave was observed in the early stage (1D simulation) and after it broke up the plasma expanded to both sides at a certain expansion velocity that depended on the laser intensity. The shock wave velocity, and more importantly for the timescales of interest to us, the expansion velocity can be approximately as a function of the laser intensity. The size of the inner

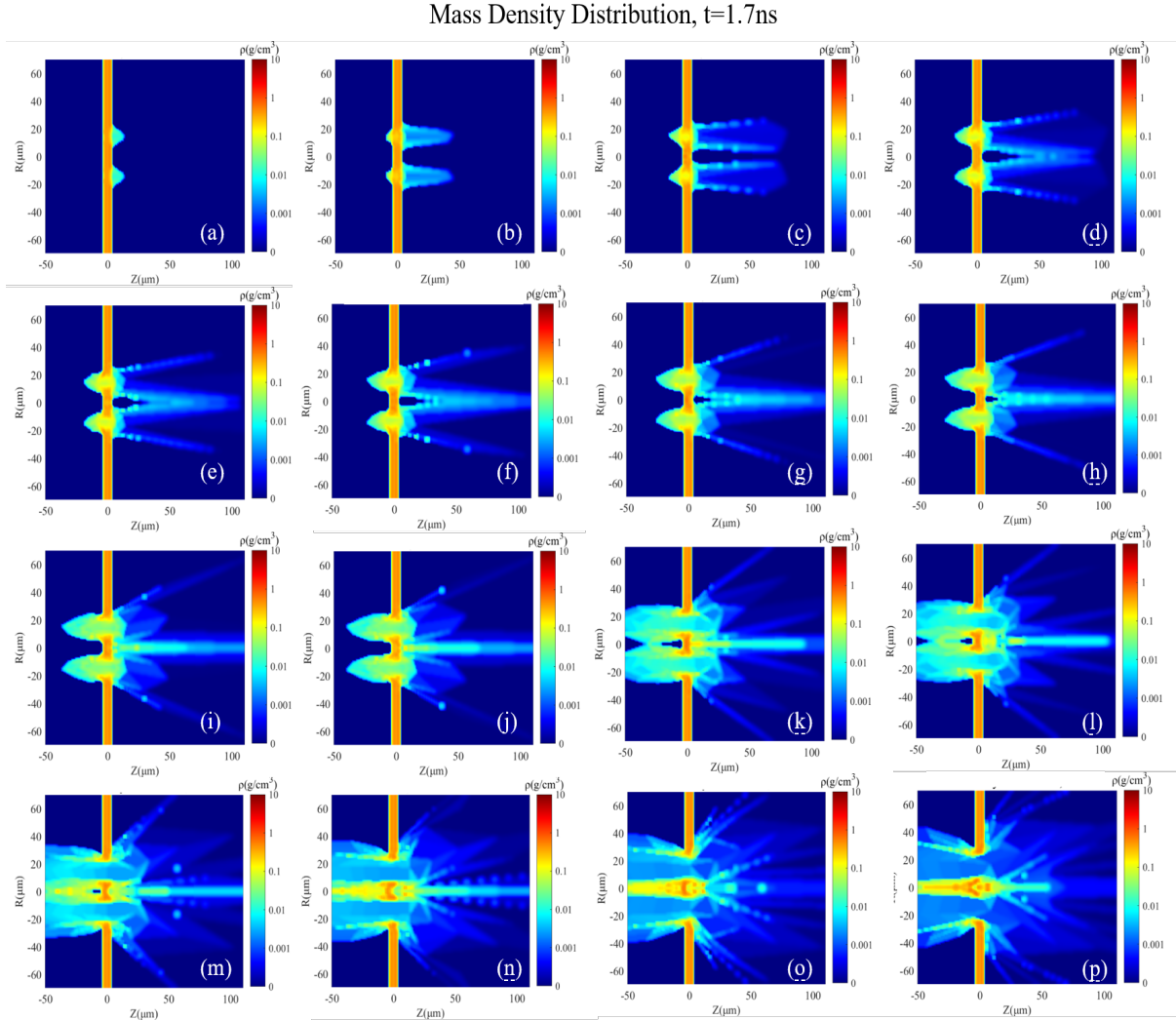


**Figure 5.12:** Mass density distribution of the donut plasma at 1.7 ns in case of different LG pre-pulse intensities. The cases (a) to (p) correspond to the 16 cases in Table 5.1. The case (a) shows the background expansion due to the intrinsic processing mechanism of MULTI that the solid target is treated as a fluid even if it is not ionized. The x-axis represents the position in the laser direction. The y-axis denotes the radial distance in the cylindrical coordinate system.

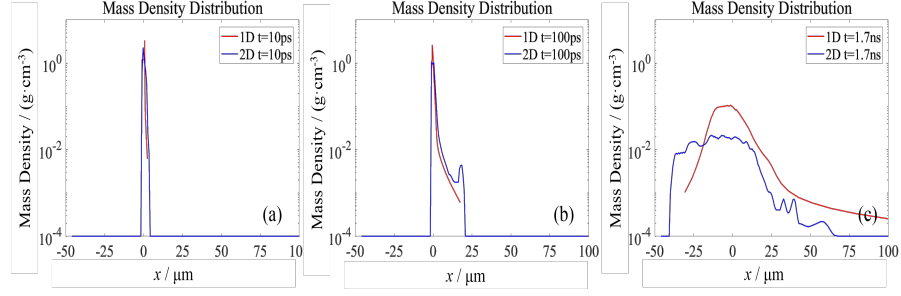


**Figure 5.13:** The comparison of mass density distribution for 1D and 2D simulation in case of  $I=30I_{th}$ . (a-c) are at 10 ps, 100 ps and 1.7 ns, respectively

target depends on the intensity contour of the LG prepulse, more precisely, where the intensity crosses the ionization threshold. Therefore, we can model the plasma state at the arrival time of the main pulse based on a simple model with only two parameters: the radius of the inner target  $r_i$ , the radius of outer boundary of the ring  $r_o$  and the intensity-dependent expansion velocity. This model will be explained in the following section as a prerequisite to study the interaction of the main laser pulse via PIC simulations.

## 5.4 The interaction between the main pulse and the target

### 5.4.1 Modeling of the initial plasma density distribution

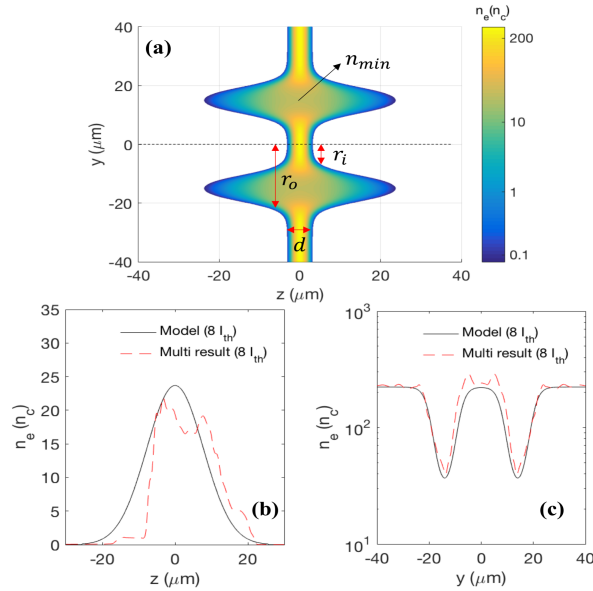


**Figure 5.14:** (a) The electron density distribution model explaining the parameters  $r_i$ ,  $r_o$ ,  $n_{min}$  and  $d$ . (b) Longitudinal density distribution at  $y = \frac{r_i+r_o}{2}$  from our model with  $n_{min} = 0.1n_0$  (solid black line) compared to the MULTI simulation result (dashed red line). (c) Transverse density distribution  $n_e(z=0, y)$  from our model with the same  $n_{min}$  (solid black line) and the MULTI simulation result (dashed red line).

As an input for the PIC simulations, we require the density distribution at the time of main pulse interaction, i.e. 1.7 ns after the pre-pulse impacted the foil. One could export the plasma density distribution obtained in the MULTI-simulations at that time. But it is more instructive to simplify the description. Starting from the part where the pre-pulse intensity is higher than  $I_{th}$ , the ring plasma will expand mainly orthogonal to the target surface with a radial expansion velocity distribution that depends on the intensity of the LG pre-pulse. We propose a simple formula for the initial distribution of electron density due to the LG pre-pulse

$$n(z, y) = n(y) \exp\left(-\frac{\pi(n(y)(z - z_0))^2}{(n_0 d)^2}\right), \quad (5.21)$$

where  $n_0$  and  $d$  are the initial electron density and thickness of the foil target before pre-expansion started, respectively. The transverse distribution

$$n(y) = n_{min} + \frac{n_0 - n_{min}}{2} \left[ 2 + \tanh\left(\frac{r_i + y}{4\lambda_L}\right) + \tanh\left(\frac{r_i - y}{4\lambda_L}\right) - \tanh\left(\frac{r_o + y}{4\lambda_L}\right) - \tanh\left(\frac{r_o - y}{4\lambda_L}\right) \right], \quad (5.22)$$

where  $n_{min}$  denotes the density in the middle of the ring at  $(z, y) = (0, \frac{r_i + r_o}{2})$  and  $\lambda_L$  is the laser wavelength. A typical example with  $r_i = 8 \mu m$  and  $r_o = 20 \mu m$  (extracted from intensity contour for  $I_{pp} = 8I_{th}$ ) is shown in Figure 5.14a.

In the model 5.21 and 5.22, the parameters  $r_i$ ,  $r_o$  and  $n_{min}$  can be estimated from the intensity contour of the LG prepulse and adjusted to match the MULTI simulations. Figure 5.14b and c compares the longitudinal density distribution at  $y = \frac{r_i + r_o}{2}$  and transverse density distribution at  $z = 0$  from our model for  $I_{pp} = 8I_{th}$  with adjusted  $n_{min} = 0.1n_0$  to the MULTI simulation results. It is obvious that the simple model for the pre-plasma density distribution does not account for transverse expansion effects. At increasing pre-pulse intensities, the MULTI results in Figure 5.12 evidence a more complicated structure. In particular, the density pinches in the center in front of the target. This plasma can affect the propagation and interaction of the main laser pulse with the target. We have studied the influence of this pre-plasma with PIC simulations for otherwise non-disturbed targets. Although the laser-plasma interaction is indeed affected, the effect on proton acceleration was not very pronounced, except that proton energies were slightly increased (upmost 25% enhancement), mainly due to self-focusing. Therefore, we consider only the effect of the donut-shaped plasma which we use as input for PIC simulations that are described in the following.

#### 5.4.2 PIC simulation results

The density distribution from our model serves to define the starting condition for the two-dimensional PIC simulations, where the input parameters  $r_i$ ,  $r_o$  are estimated from the intensity contour and  $n_{min}$  is adjusted to the pre-pulse intensity  $I_{pp}$  based on MULTI simulation results. We employed the plasma simulation code (PSC) [21] and each simulation was defined in a 2D box of  $50 \times 50 \mu m^2$  with  $5000 \times 5000$  mesh cells. A linear polarized laser pulse with a Gaussian profile  $I = I_0 \exp(-y^2/r^2) \exp(-(t - t_0)^2/\tau^2)$  was incident, where  $I_0 = 8 \times 10^{19} W/cm^2$ ,  $r = 3.1 \mu m$ ,  $t_0 = 66 fs$  and  $\tau = 33 fs$ . The plastic target was assumed to be composed of hydrogen and carbon atoms with a number ratio of 1:1. The target was fully ionized initially. The PIC simulations were performed by Bin Liu from Helmholtz-Institut Jena.

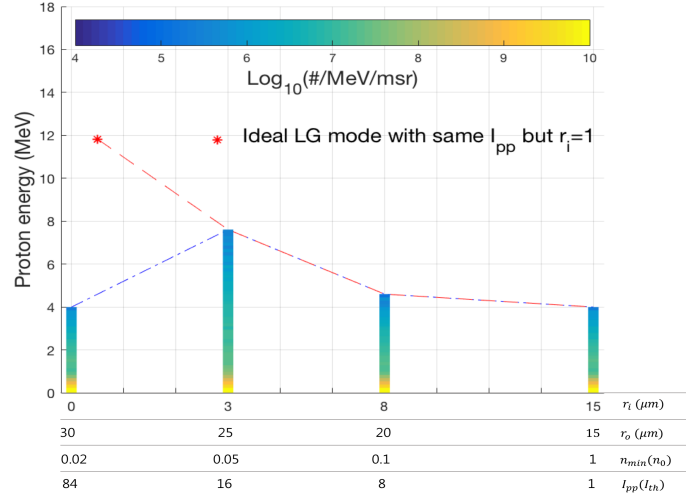


**Figure 5.15:** PIC simulation results using our model with parameters  $r_i$  and  $r_o$  extracted from intensity contour and  $n_{min}$  adjusted by MULTI simulation. The proton spectra (logarithmically color-coded) corresponding to 4 pre-pulse intensities of  $I_{pp}$  used in the experiment. The blue dash-dotted line shows the trend of maximum proton energy depending on  $I_{pp}$  in our model and the red star point denotes the potential of maximum proton energy with an ideal LG mode of the same  $I_{pp}$  but non-zero  $r_i$ .

We performed the PIC simulations with parameters  $r_i$  and  $r_o$  extracted from intensity contour and  $n_{min}$  adjusted by MULTI simulation for 4 pre-pulse intensities used in the experiment. Increasing  $I_{pp}$  from  $I_{th}$  to  $84I_{th}$  leads to an enhancement of proton acceleration, well in line with the experimental observation.

When  $r_i$  is comparable to the laser focal spot radius (in Figure 5.15 at  $r_i = 3 \mu m$ ), the maximum proton energy reaches its peak. However, with further increasing pre-pulse intensity  $I_{pp}$ , the size of the inner target  $r_i$  drops to zero (e.g. at  $84I_{th}$ ), which causes pre-expansion also in the center. This result in a pronounced density gradient and hence in reduced sheath fields. The negative effect of the pre-expanded plasma on proton acceleration has been studied and confirmed in many studies, e.g. [61]. The reason that we chose  $r_i = 0$  for  $I_{pp} = 84I_{th}$  lies in the imperfection of the LG-mode and its limited spatial contrast that is approximately 30. This means, that the pre-pulse intensity in the centre, that would ideally be zero, overcomes the ionization threshold and causes pre-expansion. An ideal LG mode with a small azimuthal index  $m=1$ , would allow for a non-zero  $r_i$ , for example,  $r_i = 1 \mu m$  with the same  $I_{pp} = 84I_{th}$ . In this case, the simulation predicts a much higher maximum proton energy (red star in Figure 5.15). We conclude that the increase of proton energy observed in our experiments is related to the donut-shaped pre-plasma that surrounds a central, largely undisturbed target platelet.

### 5.4.3 Physical explanation

In order to explore the physical origin of the increase in proton energy from  $I_{th}$  to  $16I_{th}$  (Figure 5.16a black and red curves), we examined the temporal evolution of the maximum proton forward momentum component,  $Pz_{max}$  in Figure 5.16d. The slope  $\Delta Pz_{max}/\Delta t$  represents the acceleration field  $E_z$ . Comparing the two curves, the slope ( $E_z$ ) for  $I_{th}$  is the same as that for

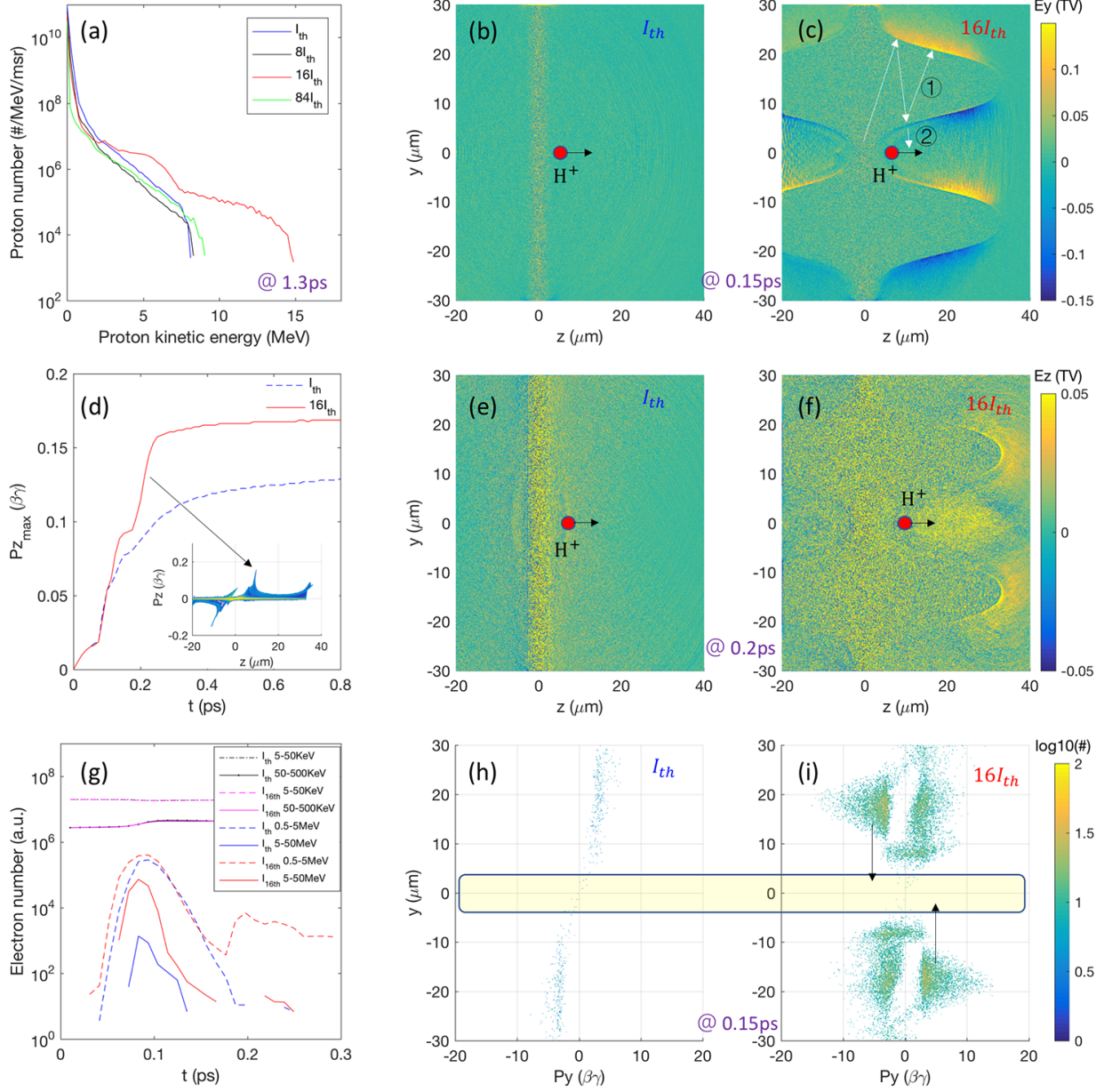


**Figure 5.16:** Proton spectra at 1.3 ps extracted from the 2D PIC simulation. b, c, e, f) The distribution of the longitudinal and transverse field  $E_z$  and  $E_y$  at 0.2 ps and 0.15 ps for the two cases, respectively. The white lines in f) show possible paths of electrons. The red points show the position of the fastest proton at the times 0.2 and 0.15 ps. d) The evolution of the maximum longitudinal momentum  $P_z$  of protons over time and the inset shows a phase-space diagram at 0.2 ps. g) The variation of electron number in space  $-3 \mu\text{m} < y < 3 \mu\text{m}$  in the specified kinetic energy ranges over time for two cases, respectively. h, i) The transverse phase-space diagram of electrons with kinetic energies in 0.5-5MeV at 0.15 ps. The black arrows show the movement direction of some electrons.

$16I_{th}$  before 0.1 ps and then the former appears to asymptotically approach zero. However, the latter changes the decreasing trend at about 0.18 ps with an inflection point and appears constant until 0.23 ps, meaning that the fastest protons are accelerated by a second strong longitudinal field. After  $\sim 0.23$  ps this field also asymptotically approaches zero as with the  $I_{th}$  case. The distribution of such a strong field  $E_z$  behind the central target at 0.2 ps is shown in Figure 5.16c and the position of the fastest protons is marked by a red point. In contrast, the field  $E_z$  acting on the fastest protons for  $I_{th}$  is much weaker now (Figure 5.16b). To understand the formation of this electric field staging in this place during this time, we studied the variation of the electron number in space  $-3 \mu m < y < 3 \mu m$  over time, grouped by different mean kinetic energy ranges (Figure 5.16g). The number of electrons with low kinetic energies ( $< 0.5$  MeV) for  $16I_{th}$  is the same as that for  $I_{th}$ , while the number with high kinetic energies ( $> 5$  MeV) is enhanced by about two orders of magnitude at 0.08 ps. Importantly, the number of electrons with kinetic energies in 0.5-5 MeV for  $16I_{th}$  starts to increase sharply from 0.18 ps, which is also the time which corresponds to the  $E_z$  inflection point displayed in Figure 5.16d. This is because a transient electron oscillation cavity is formed by the strong transverse charge-separation electric field  $E_y$  at the outer edge of the expanded annular plasma (Figure 5.16f). Hot electrons are reflected there as confirmed by the electrons transverse phase-space diagram (Figure 5.16i). In Figure 5.16f, the white arrows show possible paths of electrons with a certain exit angle. Considering a distance of the path 2 as  $50 \mu m$  and a total time 0.18 ps, the average velocity of the electrons is about  $2.8 \times 10^8$  m/s ( $\sim 1$  MeV), which is in the range of 0.5-5 MeV and evidences the rationality of this movement trajectory picture. We conclude that the expanded annular plasma generated an electron oscillation cavity. A fraction of hot electrons bounces back towards the center and overtakes the protons in the z-direction thereby participate in further acceleration by enhancing the field  $E_z$ .

#### 5.4.4 Predictions

As demonstrated in the previous sections, the enhancement of proton acceleration depends on the radius  $r_i$ , the radius of donut plasma  $r_o$  (more specifically, the gap distance  $\Delta r = r_o - r_i$ ), and the density  $n_{min}$  at ( $z = 0, y = (r_i + r_o)/2$ ). Those parameters can be controlled experimentally by changing the delay time, topological charge  $l$  of SPP and the intensity of the LG prepulse  $I_{pp}$ . Intuitively, small  $r_i$ , large  $\Delta r$  and a small  $n_{min}$  will increase the isolation of central platelet which could lead to stronger confinement of hot electrons and therefore enhanced acceleration. We therefore performed a systematic parameter scan on the basis of the PIC simulations to explore the potential of the LG-prepulse for proton acceleration enhancement.

We first studied the influence of the parameter  $n_{min}$ , where the radius  $r_i = 3 \mu m$  and the plasma gap size  $\Delta r = 5 \mu m$  were kept fixed (Figure. 5.17). The maximum proton energy rises up monotonically with the decrease of the plasma density  $n_{min}$ . The case  $n_{min} = n_0$  denotes the situation without a pre-pulse. The enhancement effect starts to be apparent from  $n_{min} < 0.3n_0$ . The red star in Figure 5.17 (a) is the best experimental result with the same  $r_i$  and  $n_{min}$ . The simulation results suggest that further improvement is possible if  $n_{min}$  can be reduced further. Experimentally, this could be achieved by increasing the delay time between pre-pulse and main pulse. For the case  $n_{min} = 0$  and  $r_i = 3 \mu m$ , the effect of the plasma gap distance  $\Delta r$  on the proton acceleration is shown in Figure 5.17(b). The maximum proton energy is sensitive to  $\Delta r$  up to  $\Delta r > 7 \mu m$ .

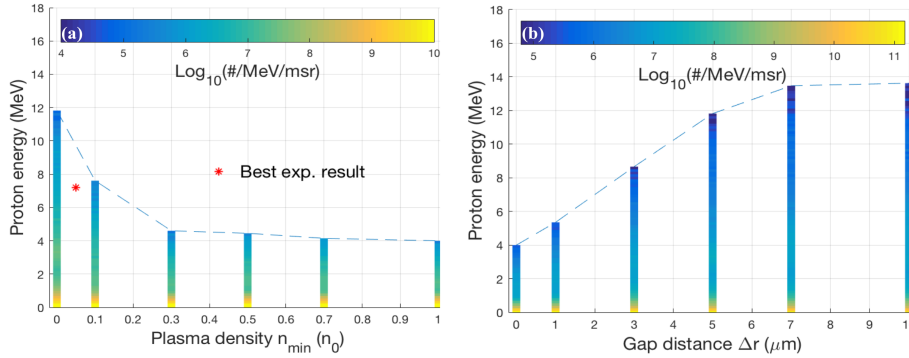


**Figure 5.17:** The proton spectra and maximum proton energy as functions of the plasma density  $n_{min}$  (a) and the distance of plasma gap  $\Delta r$  (b). The spectra and the maximum proton energies were obtained from the PIC simulation of the interaction between the main pulse and the composite target after 533 fs. In Figure (a), the radius of QIMT was fixed at  $3 \mu m$  and  $\Delta r = 5 \mu m$ . In Figure (b), the plasma density was chosen to be the best case  $n_{min} = 0$ . The radius of QIMT  $r_i$  was fixed at  $3 \mu m$ .

Finally, we studied the effect of  $r_i$  by keeping the outer radius  $r_o = 10 \mu m$  and the plasma density  $n_{min} = 0$  constant. For this situation, it is important to note that the pulse duration of the main laser pulse is an important parameter as well, because when the pulse duration is very long, laser energy cannot be coupled into a very small target due to inherent expansion during the interaction. Therefore, we studied the dependence on laser pulse duration as well.

IMPORTANT: When varying the laser pulse duration, we kept the laser energy constant, i.e., longer pulses have lower intensity in our simulation.

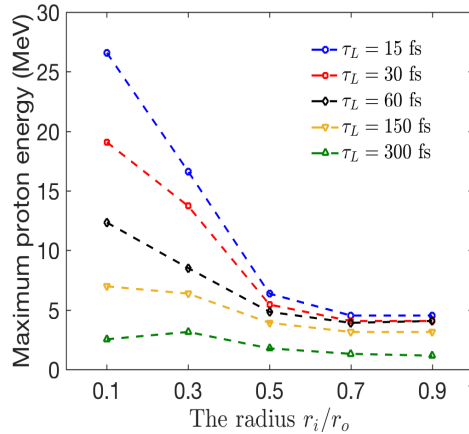


**Figure 5.18:** Maximum proton energy as a function of the radius  $r_i$  of QIMT for different pulse duration  $\tau_L$ . The radius of outer boundary  $r_o = 10 \mu m$  and the plasma density  $n_{min} = 0$  are kept fixed. The laser energy is fixed at 2.8J.

**Trends over radius  $r_i/r_o$**  It can be seen in Figure 5.18 that in the range  $0.5 \leq r_i/r_o \leq 0.9$ , the maximum proton energy does not change much. When  $r_i/r_o < 0.5$ , the proton acceleration is significantly enhanced, in particular, with short pulse duration (blue, red and black curves). Because the laser energy is fixed, with increasing the pulse duration, the laser intensity reduces in the simulated case from  $8 \times 10^{18} \text{ W/cm}^2$  to  $1.6 \times 10^{18} \text{ W/cm}^2$  but the enhancement for proton acceleration can still occur in case of  $r_i/r_o < 0.5$  (yellow and green curves).

## 5.5 Conclusions

The studies revealed a significant enhancement of proton acceleration by manipulating plain foil targets with LG-pre-pulse. The experimental results can be described by PIC-simulations with a simple model for the density distribution of the pre-plasma that was adapted to fluid simulations. PIC-simulations revealed also, that the parameters were not yet optimized in the performed experiments. Simple measures can be prolonging delays between pre- and the main pulse to decrease the annular pre-plasma density. The most dramatic effect though is achieved when matching the inner size of the platelet ( $r_i$ ) to the appropriate laser focal spot radius and pulse duration.



# Chapter 6

## Summary and outlook

### 6.1 Summary

In this work, a high repetition-rate proton source based on laser-driven ion acceleration, i.e. Target Normal Sheath Acceleration mechanism, and a new all-optical method of proton acceleration enhancement which is compatible with the high repetition-rate experiments are covered. We studied the stability and sensitivity of the high repetition-rate proton source using the ATLAS-300 laser system. We performed a first experiment with the CLAPA 200TW laser system at Peking University on optical manipulation of the target. A transiently isolated micro-plasma was achieved. We modeled the evolution of plasma expansion and studied the effect with PIC simulations and confirmed that a transiently quasi-isolated micro-plasma has a similar function as a Mass-Limited-Target, i.e., hot electrons are confined and subsequently increases the transfer efficiency from laser energy to proton energy.

Laser ion acceleration combines ultra-intense ultra-short pulse laser technology, target preparation and control technology. Only when all the technical parameters are stable and controllable a truly quantifiable and controllable ion source can be realized. Among the parameters, the laser intensity is an important one, which determines the physics process of the laser-matter interaction. When the peak intensity  $I_{peak}$  is higher than  $4.6 \times 10^{24} W/cm^2$ , the laser can interact with the protons directly. Until then, proton acceleration is mediated via charge separation fields set up by hot electrons energized by the laser [106]. Based on the typical target damage threshold of  $I_{th} \approx 10^{13} W/cm^2$ , the intensity ratio of pre-pulses should be smaller than  $I_{th}/I_{peak}$ . Otherwise, the target is ionized by the pre-pulse before the main pulse arrives and the reduced density gradient eventually leads to a degradation of ion acceleration [61]. Therefore, the temporal contrast ratio is a decisively important parameter.

When temporal contrast is under control, laser energy and pulse duration are key parameters for optimizing ion acceleration. In particular, for small targets (mass-limited or like in our case, transiently isolated ones), the transit time  $\tau_t$  that electrons spread from the center to the edges and back should be taken into consideration. At  $\tau_t \leq \tau_L$ , confining hot electrons generates a time-averaged denser, hotter, and more homogeneous electron population, which results in increased maximum proton energies and increased laser-to-ion conversion efficiency [70]. Therefore, the

pulse duration will need to be controlled in a certain range and adjusted to the target size. In addition to laser parameters, important target parameters include thickness and positioning accuracy.

Therefore, the prerequisite for high repetition rate laser ion sources to achieve stable output is that each parameter needs to be kept within a tight range. Under the existing experimental conditions, we were not yet able to stabilize the ion source based on the ATLAS-300TW laser as was described in Chapter 4.

By changing the target parameters or structuring a special target, the efficiency of laser-to-ion energy conversion can be greatly improved. Among the many possibilities, the mass-limited-target (that is, the target's lateral size is comparable to the size of the laser focal spot) can increase the ion energy and number by confining thermal electrons. This is experimentally challenging for high repetition rate experiments mainly due to difficulties in fast and precise positioning. This inspired me to take the approach of optically reshaping or shearing the target in situ. Specifically, a large flat target is pretreated by an LG pre-pulse. The target beneath the LG pre-pulse is ionized and expanded, causing the small target at the center to be separated from the large target and become quasi-isolated. Since the center small target has negligible displacement under the action of gravity in such a short period of time (nanoseconds), the main pulse can be aimed at the center of the LG pre-pulse. In this way, the problem of quickly locating MLT is effectively solved. As for how much the ion energy can be increased by this method, how to control the size of the small central target, the choice of time delay, and how to reconstruct its physical image through simulation, were covered in Chapter 5.

## 6.2 Outlook

Throughout this work, the temporal contrast remained the decisive parameter in laser-ion acceleration. It is important to note that what is actually desired is knowledge about the temporal intensity distribution of the laser pulse in the focal plane, in particular the contrast there. At focus, this contrast may be affected by the spatial intensity or phase modulation in the near-field. Based on the numerical simulating with a large numerical aperture in Section 2.2, one can use the simulation algorithm of time and space focusing shown in Figure 6.1 to derive the temporal contrast for different, practically relevant cases. Here, the operator  $P_{space}$  represents the focusing calculation with coordinate transform mentioned in Section 2.2.  $F_{time}$  and  $F_{time}^{-1}$  are Fourier transform and inverse Fourier transform, respectively.

In order to discuss the influence of the spatial intensity or phase modulation in the near field on the temporal contrast at focus, and to guide future developments, an ideal Gaussian temporal contrast curve before focusing was assumed. Through a Fourier transform  $F_{time}$ , one obtained the phase for each wavelength. When propagating the laser into the focal plane using the operator  $P_{space}$ . Intensity modulation or phase modulation can be added artificially. The temporal contrast curve at focus is obtained by using an inverse Fourier transform  $F_{time}^{-1}$ . We show the time contrast curve without any modulation (blue), with intensity modulation (cyan, black), and with phase mode (magenta,green) in Figure 6.2. The spatial intensity modulations (blue, cyan, black curves) do not influence the temporal contrast but only the fill factor 0.8-0.6 describes the

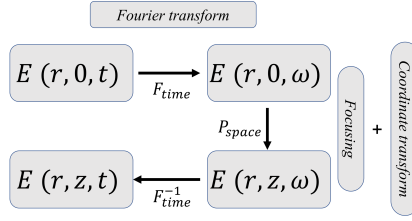


**Figure 6.1:** The simulation algorithm of time and space focusing. Adopted from [78]

uniformity of the modulated near-field intensity. 1D periodic random phase modulation (magenta) and spiral phase modulation (green) both lead to deterioration of the temporal contrast in focus, which give us inspiration that a perfect plane spatial phase results in the best temporal contrast ratio. This is important to keep in mind when planning experiments that rely on spatial phase modulation of the highly intense laser pulse.

In the future, it would be beneficial if one can additionally measure the phase for each wavelength in advance and measure the spatial phase modulation for real time via wave-front sensor as one could construct the temporal contrast curve at focus for each shot, which may give key insights to the laser-ion acceleration process.

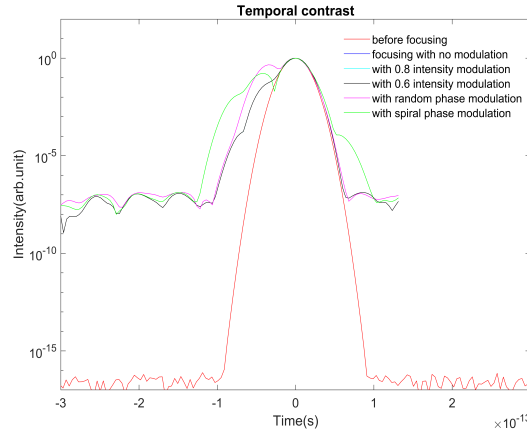


**Figure 6.2:** Temporal contrast curves in different cases, as the legend shows

Regarding the transient micro-plasma generated by LG pre-pulse, we have shown great potential to enhance laser ion acceleration. However, there is still much interesting work to be done. For example, the time delay between the LG pre-pulse and the main pulse can be extended to microseconds. At this time, the effect of gravity can still be ignored, but the central micro-plasma will be further isolated, and simulations predict further enhancing the proton acceleration. The time evolution of the LG-pulse triggered plasma was studied through fluid dynamics simulations. It would be interesting to explore this pre-expansion process through pump-probe experiments to give more direct evidence of the existence and shape of the micro-target. It might also be advisable to build an additional beamline for the LG pre-pulse so that it can be generated and

manipulated independently. The main pulse could be reflected by plasma mirrors to improve the temporal contrast which would enable the use of very thin (nm) micro-size targets to study Radiation Pressure Acceleration. This separate pre-pulse beamline would also allow for spatially cleaning the LG prepulse for obtaining higher spatial contrast, which will be beneficial to obtain a miniature target with a higher isolation degree and smaller transverse size.

# Bibliography

- [1] D. Strickland, G. Mourou, Compression of amplified chirped optical pulses, *Optics Commun.* 55 (6) (1985) 447.
- [2] A. J. Mackinnon, P. K. Patel, M. Borghesi, R. C. Clarke, R. R. Freeman, H. Habara, S. P. Hatchett, D. Hey, D. G. Hicks, S. Kar, M. H. Key, J. A. King, K. Lancaster, D. Neely, A. Nikkro, P. A. Norreys, M. M. Notley, T. W. Phillips, L. Romagnani, R. A. Snavely, R. B. Stephens, R. P. J. Town, Proton radiography of a laser-driven implosion, *Phys. Rev. Lett.* 97 (2006) 045001.
- [3] P. K. Patel, A. J. Mackinnon, M. H. Key, T. E. Cowan, M. E. Foord, M. Allen, D. F. Price, H. Ruhl, P. T. Springer, R. Stephens, Isochoric heating of solid-density matter with an ultrafast proton beam, *Phys. Rev. Lett.* 91 (2003) 125004.
- [4] B. Dromey, M. Coughlan, L. Senje, M. Taylor, S. Kuschel, B. Villagomez-Bernabe, R. Stefanuik, G. Nersisyan, L. Stella, J. Kohanoff, M. Borghesi, F. Currell, D. Riley, D. Jung, C. G. Wahlström, C. L. Lewis, M. Zepf, Picosecond metrology of laser-driven proton bursts, *Nat. Commun.* 7 (10642) (2016) 3–8.
- [5] U. Linz, J. Alonso, What will it take for laser driven proton accelerators to be applied to tumor therapy?, *Phys. Rev. Spec. Top. - Accel. Beams* 10 (9) (2007) 1–8.
- [6] M. Roth, T. E. Cowan, M. H. Key, S. P. Hatchett, C. Brown, W. Fountain, J. Johnson, D. M. Pennington, R. A. Snavely, S. C. Wilks, K. Yasuike, H. Ruhl, F. Pegoraro, S. V. Bulanov, E. M. Campbell, M. D. Perry, H. Powell, Fast ignition by intense laser-accelerated proton beams, *Phys. Rev. Lett.* 86 (3) (2001) 436–439.
- [7] J. Nuckolls, J. Wood, A. Thiessen, G. Zimmerman, Laser compression of matter to super-high densities: Thermonuclear (ctr) applications, *Nature* 239 (1972) 139.
- [8] J. E. Crow, P. L. Auer, J. E. Allen, The expansion of a plasma into a vacuum, *Journal of Plasma Physics* 14 (1) (1975) 65.
- [9] F. Mako, T. Tajima, Collective ion acceleration by a reflexing electron beam: Model and scaling, *The Physics of Fluids* 27 (7) (1984) 1815.
- [10] N. Sarukura, Y. Ishida, H. Nakano, Generation of 50-fsec pulses from a pulse-compressed, cw, passively mode-locked ti:sapphire laser, *Opt. Lett.* 16 (3) (1991) 153.
- [11] F. Pegoraro, T. Esirkepov, S. Bulanov, Special relativity in action in laser produced plasmas, *Physics Letters A* 347 (1) (2005) 133–142.

- [12] A. P. Fews, P. A. Norreys, F. N. Beg, A. R. Bell, A. E. Dangor, C. N. Danson, P. Lee, S. J. Rose, Plasma ion emission from high intensity picosecond laser pulse interactions with solid targets, *Phys. Rev. Lett.* 73 (1994) 1801–1804.
- [13] A. Maksimchuk, S. Gu, K. Flippo, D. Umstadter, V. Y. Bychenkov, Forward ion acceleration in thin films driven by a high-intensity laser, *Phys. Rev. Lett.* 84 (2000) 4108–4111.
- [14] E. L. Clark, K. Krushelnick, J. R. Davies, M. Zepf, M. Tatarakis, F. N. Beg, A. Machacek, P. A. Norreys, M. I. K. Santala, I. Watts, A. E. Dangor, Measurements of energetic proton transport through magnetized plasma from intense laser interactions with solids, *Phys. Rev. Lett.* 84 (2000) 670–673.
- [15] R. A. Snavely, M. H. Key, S. P. Hatchett, T. E. Cowan, M. Roth, T. W. Phillips, M. A. Stoyer, E. A. Henry, T. C. Sangster, M. S. Singh, S. C. Wilks, A. MacKinnon, A. Offenberger, D. M. Pennington, K. Yasuike, A. B. Langdon, B. F. Lasinski, J. Johnson, M. D. Perry, E. M. Campbell, Intense high-energy proton beams from petawatt-laser irradiation of solids, *Phys. Rev. Lett.* 85 (2000) 2945–2948.
- [16] J. Davies, Proton acceleration by fast electrons in lasersolid interactions, *Laser and Particle Beams* 20 (2) (2002) 243–253.
- [17] X. Q. Yan, C. Lin, Z. M. Sheng, Z. Y. Guo, B. C. Liu, Generating High-Current Monoenergetic Proton Beams by a Circularly Polarized Laser Pulse in the Phase-Stable Acceleration Regime, *Phys. Rev. Lett.* 100 (135003) (2008) 1–4.
- [18] M. Zepf, E. L. Clark, F. N. Beg, R. J. Clarke, A. E. Dangor, A. Gopal, K. Krushelnick, P. A. Norreys, M. Tatarakis, U. Wagner, M. S. Wei, Proton acceleration from high-intensity laser interactions with thin foil targets, *Phys. Rev. Lett.* 90 (064801) (2003) 1–4.
- [19] I. Spencer, K. W. D. Ledingham, P. McKenna, T. McCanny, R. P. Singhal, P. S. Foster, D. Neely, A. J. Langley, E. J. Divall, C. J. Hooker, R. J. Clarke, P. A. Norreys, E. L. Clark, K. Krushelnick, J. R. Davies, Experimental study of proton emission from 60-fs, 200-mj high-repetition-rate tabletop-laser pulses interacting with solid targets, *Phys. Rev. E* 67 (4) (2003) 046402–046406.
- [20] M. Roth, A. Blazevic, M. Geissel, T. Schlegel, T. E. Cowan, M. Allen, et al., Energetic ions generated by laser pulses: A detailed study on target properties, *Phys. Rev. Spec. Top. - Accel. Beams* 5 (061301) (2002) 1–8.
- [21] A. J. Mackinnon, M. Borghesi, S. Hatchett, M. H. Key, P. K. Patel, H. Campbell, A. Schiavi, R. Snavely, S. C. Wilks, O. Willi, Effect of plasma scale length on multi-mev proton production by intense laser pulses, *Phys. Rev. Lett.* 86 (9) (2001) 1769–1772.
- [22] Y. Oishi, T. Nayuki, T. Fujii, Y. Takizawa, X. Wang, T. Yamazaki, K. Nemoto, T. Kayoiji, T. Sekiya, K. Horioka, Y. Okano, Y. Hironaka, K. G. Nakamura, K. Kondo, A. A. Andreev, Dependence on laser intensity and pulse duration in proton acceleration by irradiation of ultrashort laser pulses on a cu foil target, *Phys. Plasmas* 12 (7) (2005) 073102.
- [23] J. Fuchs, P. Antici, E. Dhumieres, E. Lefebvre, M. Borghesi, E. Brambrink, et al., Laser-driven proton scaling laws and new paths towards energy increase, *Nat. Phys.* 2 (2006) 48–54.

- [24] H. Schworer, S. Pfoth, O. Jäckel, K. U. Amthor, B. Liesfeld, W. Ziegler, R. Sauerbrey, K. W. Ledingham, T. Esirkepov, Laser-plasma acceleration of quasi-monoenergetic protons from microstructured targets, *Nature* 439 (7075) (2006) 445–448.
- [25] B. M. Hegelich, B. J. Albright, J. Cobble, K. Flippo, S. Letzring, M. Paffett, H. Ruhl, J. Schreiber, R. K. Schulze, J. C. Fernandez, Laser acceleration of quasi-monoenergetic mev ion beams, *Nature* 439 (2006) 441–444.
- [26] E. Brambrink, J. Schreiber, T. Schlegel, P. Audebert, J. Cobble, J. Fuchs, M. Hegelich, M. Roth, Transverse characteristics of short-pulse laser-produced ion beams: A study of the acceleration dynamics, *Phys. Rev. Lett.* 96 (154801) (2006) 1–4.
- [27] L. Robson, P. T. Simpson, R. J. Clarke, K. W. Ledingham, F. Lindau, O. Lundh, T. McCanny, P. Mora, D. Neely, C. G. Wahlström, M. Zepf, P. McKenna, Scaling of proton acceleration driven by petawatt-laser-plasma interactions, *Nat. Phys.* 3 (1) (2007) 58–62.
- [28] M. Alien, Y. Sentoku, P. Audebert, A. Blazevic, T. Cowan, J. Fuchs, J. C. Gauthier, M. Geissel, M. Hegelich, S. Karsch, E. Morse, P. K. Patel, M. Roth, Proton spectra from ultraintense laser-plasma interaction with thin foils: Experiments, theory, and simulation, *Phys. Plasmas* 10 (8) (2003) 3283–3289.
- [29] T. Esirkepov, M. Yamagiwa, T. Tajima, Laser ion-acceleration scaling laws seen in multi-parametric particle-in-cell simulations, *Phys. Rev. Lett.* 96 (10) (2006) 1–4.
- [30] P. Mora, Plasma Expansion into a Vacuum, *Phys. Rev. Lett.* 90 (18) (2003) 4.
- [31] E. Fourkal, I. Velchev, C. M. Ma, Coulomb explosion effect and the maximum energy of protons accelerated by high-power lasers, *Phys. Rev. E - Stat. Nonlinear, Soft Matter Phys.* 71 (3) (2005) 1–11.
- [32] J. Schreiber, F. Bell, F. Grüner, U. Schramm, M. Geissler, M. Schnürer, S. Ter-Avetisyan, B. M. Hegelich, J. Cobble, E. Brambrink, J. Fuchs, P. Audebert, D. Habs, Analytical model for ion acceleration by high-intensity laser pulses, *Phys. Rev. Lett.* 97 (4) (2006) 1–4.
- [33] S. A. Gaillard, T. Kluge, K. A. Flippo, M. Bussmann, B. Gall, T. Lockard, M. Geissel, D. T. Offermann, M. Schollmeier, Y. Sentoku, T. E. Cowan, Increased laser-accelerated proton energies via direct laser-light-pressure acceleration of electrons in microcone targets, *Phys. Plasmas* 18 (5) (2011) 1–11.
- [34] F. Wagner, O. Deppert, C. Brabetz, P. Fiala, A. Kleinschmidt, P. Poth, V. A. Schanz, A. Tebartz, B. Zielbauer, M. Roth, T. Stöhlker, V. Bagnoud, Maximum Proton Energy above 85 MeV from the Relativistic Interaction of Laser Pulses with Micrometer Thick CH<sub>2</sub> Targets, *Phys. Rev. Lett.* 116 (20) (2016) 1–5.
- [35] A. Higginson, R. J. Gray, M. King, R. J. Dance, S. D. Williamson, N. M. Butler, R. Wilson, R. Capdessus, C. Armstrong, J. S. Green, S. J. Hawkes, P. Martin, W. Q. Wei, S. R. Mirfayzi, X. H. Yuan, S. Kar, M. Borghesi, R. J. Clarke, D. Neely, P. McKenna, Near-100 MeV protons via a laser-driven transparency-enhanced hybrid acceleration scheme, *Nat. Commun.* 9 (1) (2018) 1–9.

- [36] D. E. Bonnett, A. Kacpersek, M. A. Sheen, R. Goodall, T. E. Saxton, The 62 MeV proton beam for the treatment of ocular melanoma at Clatterbridge, *Br. J. Radiol.* 66 (790) (1993) 907–914.
- [37] V. Malka, J. Faure, J. R. Marquès, F. Amiranoff, J. P. Rousseau, S. Ranc, J. P. Chambaret, Z. Najmudin, B. Walton, P. Mora, A. Solodov, Characterization of electron beams produced by ultrashort (30 fs) laser pulses, *Phys. Plasmas* 8 (6) (2001) 2605–2608.
- [38] S. M. Hooker, Developments in laser-driven plasma accelerators, *Nat. Photonics* 7 (10) (2013) 775–782.
- [39] A. Rousse, K. Ta Phuoc, R. Shah, A. Pukhov, E. Lefebvre, V. Malka, S. Kiselev, F. Burgy, J. P. Rousseau, D. Umstadter, D. Hulin, Production of a keV X-ray beam from synchrotron radiation in relativistic laser-plasma interaction, *Phys. Rev. Lett.* 93 (13) (2004) 1–4.
- [40] K. Krushelnick, E. L. Clark, Z. Najmudin, M. Salvati, M. I. Santala, M. Tatarakis, A. E. Dangor, V. Malka, D. Neely, R. Allott, C. Danson, Multi-MeV ion production from high-intensity laser interactions with underdense plasmas, *Phys. Rev. Lett.* 83 (4) (1999) 737–740.
- [41] F. Sylla, M. Veltcheva, S. Kahaly, A. Flacco, V. Malka, Development and characterization of very dense submillimetric gas jets for laser-plasma interaction, *Rev. Sci. Instrum.* 83 (3) (2012) 033507.
- [42] L. Rymell, L. Malmqvist, M. Berglund, H. M. Hertz, Liquid-jet target laser-plasma sources for EUV and X-ray lithography, *Microelectron. Eng.* 46 (1) (1999) 453–455.
- [43] S. Düsterer, H. Schwoerer, W. Ziegler, C. Ziener, R. Sauerbrey, Optimization of EUV radiation yield from laser-produced plasma, *Appl. Phys. B Lasers Opt.* 73 (7) (2001) 693–698.
- [44] S. Karsch, S. Düsterer, H. Schwoerer, F. Ewald, D. Habs, M. Hegelich, G. Pretzler, A. Pukhov, K. Witte, R. Sauerbrey, High-Intensity Laser Induced Ion Acceleration from Heavy-Water Droplets, *Phys. Rev. Lett.* 91 (1) (2003) 2–5.
- [45] S. Ter-Avestisyan, M. Schnürer, H. Stiel, P. V. Nickles, A high-density sub-micron liquid spray for laser driven radiation sources, *J. Phys. D. Appl. Phys.* 36 (36) (2003) 2421–2426.
- [46] P. L. Poole, C. Willis, G. E. Cochran, R. T. Hanna, C. D. Andereck, D. W. Schumacher, Moderate repetition rate ultra-intense laser targets and optics using variable thickness liquid crystal films, *Appl. Phys. Lett.* 109 (15) (2016) 1–4.
- [47] P. L. Poole, C. D. Andereck, D. W. Schumacher, R. L. Daskalova, S. Feister, K. M. George, C. Willis, K. U. Akli, E. A. Chowdhury, Liquid crystal films as on-demand, variable thickness (50-5000nm) targets for intense lasers, *Phys. Plasmas* 21 (6) (2014) 1–5.
- [48] I. Prencipe, J. Fuchs, S. Pascarelli, D. W. Schumacher, R. B. Stephens, N. B. Alexander, R. Briggs, M. Bscher, M. O. Cernaianu, A. Choukourov, et al., Targets for high repetition rate laser facilities: needs, challenges and perspectives, *High Power Laser Sci. Eng.* 5 (2017) e17.

- [49] L. Obst, S. Göde, M. Rehwald, F. E. Brack, J. Branco, S. Bock, M. Bussmann, T. E. Cowan, C. B. Curry, F. Fiuza, M. Gauthier, R. Gebhardt, U. Helbig, A. Huebl, U. Hübner, A. Irman, L. Kazak, J. B. Kim, T. Kluge, S. Kraft, M. Loeser, J. Metzkes, R. Mishra, C. Rödel, H. P. Schlenvoigt, M. Siebold, J. Tiggesbäumker, S. Wolter, T. Ziegler, U. Schramm, S. H. Glenzer, K. Zeil, Efficient laser-driven proton acceleration from cylindrical and planar cryogenic hydrogen jets, *Sci. Rep.* 7 (1) (2017) 1–9.
- [50] J. Badziak, E. Woryna, P. Parys, K. Y. Platonov, S. Jabłoński, L. Ryć, A. B. Vankov, J. Wolowski, Fast proton generation from ultrashort laser pulse interaction with double-layer foil targets, *Phys. Rev. Lett.* 87 (21) (2001) 1–4.
- [51] J. H. Bin, W. J. Ma, H. Y. Wang, M. J. Streeter, C. Kreuzer, D. Kiefer, M. Yeung, S. Cousens, P. S. Foster, B. Dromey, X. Q. Yan, R. Ramis, J. Meyer-ter Vehn, M. Zepf, J. Schreiber, Ion Acceleration Using Relativistic Pulse Shaping in Near-Critical-Density Plasmas, *Phys. Rev. Lett.* 115 (6) (2015) 1–5.
- [52] S. C. Wilks, A. B. Langdon, T. E. Cowan, M. Roth, M. Singh, S. Hatchett, M. H. Key, D. Pennington, A. MacKinnon, R. A. Snavely, Energetic proton generation in ultra-intense laser-solid interactions, *Phys. Plasmas* 8 (2) (2001) 542–549.
- [53] D. Neely, P. Foster, A. Robinson, F. Lindau, O. Lundh, A. Persson, C. G. Wahlström, P. McKenna, Enhanced proton beams from ultrathin targets driven by high contrast laser pulses, *Appl. Phys. Lett.* 89 (2) (2006) 1–4.
- [54] T. Ceccotti, A. Lévy, H. Popescu, F. Réau, P. D’Oliveira, P. Monot, J. P. Geindre, E. Lefebvre, P. Martin, Proton acceleration with high-intensity ultrahigh-contrast laser pulses, *Phys. Rev. Lett.* 99 (18) (2007) 1–4.
- [55] S. Kar, K. F. Kakolee, B. Qiao, A. MacChi, M. Cerchez, D. Doria, M. Geissler, P. McKenna, D. Neely, J. Osterholz, R. Prasad, K. Quinn, B. Ramakrishna, G. Sarri, O. Willi, X. Y. Yuan, M. Zepf, M. Borghesi, Ion acceleration in multispecies targets driven by intense laser radiation pressure, *Phys. Rev. Lett.* 109 (18) (2012) 1–5.
- [56] A. Henig, D. Kiefer, K. Markey, D. C. Gautier, K. A. Flippo, S. Letzring, R. P. Johnson, T. Shimada, L. Yin, B. J. Albright, K. J. Bowers, J. C. Fernández, S. G. Rykovanov, H. C. Wu, M. Zepf, D. Jung, V. K. Liechtenstein, J. Schreiber, D. Habs, B. M. Hegelich, Enhanced laser-driven ion acceleration in the relativistic transparency regime, *Phys. Rev. Lett.* 103 (4) (2009) 1–4.
- [57] S. Seuferling, M. A. O. Haug, P. Hinz, D. Haffa, C. Kreuzer, J. Schreiber, Efficient offline production of freestanding thin plastic foils for laser-driven ion sources, *High Power Laser Sci. Eng.* 5 (e8) (2017) 1–5.
- [58] E. Hecht, A. Zajac, *Optics*, Addison - Wiley, 1974.
- [59] Eucall deliverable 6.1, <https://www.eucall.eu/organisation/deliverables/>.
- [60] A. Yogo, K. Mima, N. Iwata, S. Tosaki, A. Morace, Y. Arikawa, S. Fujioka, T. Johzaki, Y. Sentoku, H. Nishimura, A. Sagisaka, K. Matsuo, N. Kamitsukasa, S. Kojima, H. Nagatomo, M. Nakai, H. Shiraga, M. Murakami, S. Tokita, J. Kawanaka, N. Miyanaga, K. Yamanoi, T. Norimatsu, H. Sakagami, S. V. Bulanov, K. Kondo, H. Azechi, Boosting laser-ion acceleration with multi-picosecond pulses, *Sci. Rep.* 7 (42451) (2017) 1–10.

- [61] M. Kaluza, J. Schreiber, M. I. K. Santala, G. D. Tsakiris, K. Eidmann, J. Meyer-ter Vehn, K. J. Witte, Influence of the laser prepulse on proton acceleration in thin-foil experiments, *Phys. Rev. Lett.* 93 (2004) 1–4.
- [62] P. Antici, J. Fuchs, E. D’Humières, E. Lefebvre, M. Borghesi, E. Brambrink, C. A. Cecchetti, S. Gaillard, L. Romagnani, Y. Sentoku, T. Toncian, O. Willi, P. Audebert, H. Pépin, Energetic protons generated by ultrahigh contrast laser pulses interacting with ultrathin targets, *Phys. Plasmas* 14 (030701) (2007) 1–4.
- [63] F. Lindau, O. Lundh, A. Persson, P. McKenna, K. Osvay, D. Batani, C. G. Wahlström, Laser-accelerated protons with energy-dependent beam direction, *Phys. Rev. Lett.* 95 (17) (2005) 1–4.
- [64] G. Doumy, F. Quéré, O. Gobert, M. Perdrix, P. Martin, P. Audebert, J. C. Gauthier, J.-P. Geindre, T. Wittmann, Complete characterization of a plasma mirror for the production of high-contrast ultraintense laser pulses, *Phys. Rev. E* 69 (2004) 026402.
- [65] C. M. Brenner, A. P. Robinson, K. Markey, R. H. Scott, R. J. Gray, M. Rosinski, O. Depert, J. Badziak, D. Batani, J. R. Davies, S. M. Hassan, K. L. Lancaster, K. Li, I. O. Musgrave, P. A. Norreys, J. Pasley, M. Roth, H. P. Schlenvoigt, C. Spindloe, M. Tatarakis, T. Winstone, J. Wolowski, D. Wyatt, P. McKenna, D. Neely, High energy conversion efficiency in laser-proton acceleration by controlling laser-energy deposition onto thin foil targets, *Appl. Phys. Lett.* 104 (2014) 8.
- [66] P. McKenna, D. C. Carroll, O. Lundh, F. Nürnberg, K. Markey, S. Bandyopadhyay, D. Batani, R. G. Evans, R. Jafer, S. Kar, D. Neely, D. Pepler, M. N. Quinn, R. Redaelli, M. Roth, C. G. Wahlström, X. H. Yuan, M. Zepf, Effects of front surface plasma expansion on proton acceleration in ultraintense laser irradiation of foil targets, *Laser Part. Beams* 26 (4) (2008) 591–596.
- [67] K. Markey, P. McKenna, C. M. Brenner, D. C. Carroll, M. M. Günther, K. Harres, S. Kar, K. Lancaster, F. Nürnberg, M. N. Quinn, A. P. L. Robinson, M. Roth, M. Zepf, D. Neely, Spectral enhancement in the double pulse regime of laser proton acceleration, *Phys. Rev. Lett.* 105 (2010) 195008.
- [68] F. Dollar, T. Matsuoka, G. M. Petrov, A. G. Thomas, S. S. Bulanov, V. Chvykov, J. Davis, G. Kalinchenko, C. McGuffey, L. Willingale, V. Yanovsky, A. Maksimchuk, K. Krushelnick, Control of energy spread and dark current in proton and ion beams generated in high-contrast laser solid interactions, *Phys. Rev. Lett.* 107 (6) (2011) 1–5.
- [69] K. A. Flippo, E. D’Humières, S. A. Gaillard, J. Rassuchine, D. C. Gautier, M. Schollmeier, F. Nürnberg, J. L. Kline, J. Adams, B. Albright, M. Bakeman, K. Harres, R. P. Johnson, G. Korgan, S. Letzring, S. Malekos, N. Renard-Legalloudec, Y. Sentoku, T. Shimada, M. Roth, T. E. Cowan, J. C. Fernández, B. M. Hegelich, Increased efficiency of short-pulse laser-generated proton beams from novel flat-top cone targets, *Phys. Plasmas* 15 (2008) 056709.
- [70] S. Buffechoux, J. Psikal, M. Nakatsutsumi, L. Romagnani, A. Andreev, K. Zeil, M. Amin, P. Antici, T. Burris-Mog, A. Compant-La-Fontaine, E. D’Humières, S. Fourmaux, S. Gaillard, F. Gobet, F. Hannachi, S. Kraft, A. Mancic, C. Plaisir, G. Sarri, M. Tarisien,

- T. Toncian, U. Schramm, M. Tampo, P. Audebert, O. Willi, T. E. Cowan, H. Pépin, V. Tikhonchuk, M. Borghesi, J. Fuchs, Hot electrons transverse refluxing in ultraintense laser-solid interactions, *Phys. Rev. Lett.* 105 (1) (2010) 1–5.
- [71] O. Tresca, D. C. Carroll, X. H. Yuan, B. Aurand, V. Bagnoud, C. M. Brenner, M. Coury, J. Fils, R. J. Gray, T. Kühl, C. Li, Y. T. Li, X. X. Lin, M. N. Quinn, R. G. Evans, B. Zielbauer, M. Roth, D. Neely, P. McKenna, Controlling the properties of ultraintense laser-proton sources using transverse refluxing of hot electrons in shaped mass-limited targets, *Plasma Phys. Control. Fusion* 53 (2011) 10.
- [72] T. Kluge, W. Enghardt, S. D. Kraft, U. Schramm, K. Zeil, T. E. Cowan, M. Bussmann, Enhanced laser ion acceleration from mass-limited foils, *Phys. Plasmas* 17 (2010) 12.
- [73] W. Kruer, *The physics of laser plasma interactions*, *Frontiers in physics*, Addison-Wesley, 1988.
- [74] P. Gibbon, *Short Pulse interactions with matter*, Imperial College Press, 2008.
- [75] A. M. Weiner, *Ultrafast Optics*, John Wiley and Sons, 2008.
- [76] J.-C. Diels, W. Rudolph, *Ultrashort Laser Pulse Phenomena*, Second Edition, Academic Press, Amsterdam, 2006.
- [77] C. Rulliere, *Femtosecond Laser Pulses: Principles and Experiments*, Second Edition, Springer, New York, 2003.
- [78] P. Zhu, X. Xie, X. Ouyang, J. Zhu, Output temporal contrast simulation of a large aperture high power short pulse laser system, *High Power Laser Sci. Eng.* 2 (2014) e42.
- [79] V. Bagini, R. Borghi, F. Gori, A. M. Pacileo, M. Santarsiero, Propagation of axially symmetric flattened Gaussian beams, *Journal of the Optical Society of America* 13 (7) (1996) 1385–1394.
- [80] M. J. Padgett, L. Allen, The Poynting vector in Laguerre-Gaussian laser modes, *Optics Commun.* 121 (1995) 36–40.
- [81] S. yuan Chen, A. Maksimchuk, D. Umstadter, Experimental observation of relativistic nonlinear thomson scattering, *Nature* 396 (December) (1998) 653–655.
- [82] T. M. Boyd, J. J. Sanderson, *The Physics of Plasma*, Cambridge, New York, 2003.
- [83] T. Tajima, J. M. Dawson, Laser Electron Accelerator, *Phys. Rev. Lett.* 4 (4) (1979) 267–270.
- [84] W. L. Kruer, *The Physics of laser plasma interaction*, Addison-Wesley, New York, 1988.
- [85] P. Mulser, D. Bauer, *High power laser-matter interactions*, Springer, Berlin, 2010.
- [86] R. P. Godwin, Optical Mechanism for Enhanced Absorption of Laser Energy Incident on Solid Targets, *Phys. Rev. Lett.* 4 (2) (1972) 1–3.
- [87] D. W. Forslund, J. M. Kindel, K. Lee, E. L. Lindman, R. L. Morse, Theory and simulation of resonant absorption in a hot plasma, *Phys. Rev. Lett.* 11 (1975) 679–683.

- [88] J. P. Freidberg, R. W. Mitchell, R. L. Morse, L. I. Rudinski, Resonant Absorption of Laser Light by Plasma Targets, *Phys. Rev. Lett.* 28 (13) (1972) 795–799.
- [89] P. Koch, J. Albritton, Electron and ion Heating Through Resonant Plasma Oscillations, *Phys. Rev. Lett.* 32 (2) (1974) 1420–1423.
- [90] D. R. Bach, D. E. Casperson, S. J. Gitomer, P. D. Goldstone, A. Hauer, R. Kristal, G. A. Kyrala, Intensity-Dependent Absorption in 10.6-um Laser-Illuminated Spheres, *Phys. Rev. Lett.* 50 (1983) 2082–2085.
- [91] F. Brunel, Not-so-resonant, resonant absorption, *Phys. Rev. Lett.* 59 (1987) 52–55.
- [92] W. L. Kruer, K. Estabrook, Not-So-Resonant, Resonant Absorption, *Phys. Fluids* 1 (28) (1985) 430–432.
- [93] S. C. Wilks, W. L. Kruer, M. Tabak, A. B. Langdon, Absorption of ultra-intense laser pulses, *Phys. Rev. Lett.* 69 (9) (1992) 1383–1386.
- [94] P. Mora, P. R., Self-similar expansion of a plasma into a vacuum, *Phys. Fluids* 22 (12) (2003) 2300–2304.
- [95] P. Mora, Thin-foil expansion into a vacuum, *Phys. Rev. E* 72 (056401) (2005) 1–5.
- [96] Y. Sentoku, T. E. Cowan, A. Kemp, H. Ruh, High energy proton acceleration in interaction of short laser pulse with dense plasma target, *Phys. Plasma* 10 (5) (2003) 2009–2015.
- [97] M. Passoni, M. Lontano, Theory of Light-Ion Acceleration Driven by a Strong Charge Separation, *Phys. Rev. Lett.* 101 (115001) (2008) 1–4.
- [98] A. J. Mackinnon, Y. Sentoku, P. K. Patel, D. W. Price, S. Hatchett, M. H. Key, C. Andersen, R. Snavely, R. R. Freeman, Enhancement of proton acceleration by hot-electron recirculation in thin foils irradiated by ultraintense laser pulses, *Phys. Rev. Lett.* 88 (2002) 215006.
- [99] Y. Sentoku, V. Bychenkov, K. Flippo, A. Maksimchuk, K. Mima, G. Mourou, Z. Sheng, D. Umstadter, High-energy ion generation in interaction of short laser pulse with high-density plasma, *Appl. Phys. B* 74 (2002) 207–215.
- [100] A. Macchi, F. Cattani, T. V. Liseykina, F. Cornolti, Laser Acceleration of Ion Bunches at the Front Surface of Overdense Plasmas, *Phys. Rev. Lett.* 94 (165003) (2005) 2–5.
- [101] T. V. Liseykina, A. Macchi, Features of ion acceleration by circularly polarized laser pulses, *Appl. Phys. Lett.* 91 (171502) (2007) 1–3.
- [102] A. P. L. Robinson, R. M. G. M. Trines, N. P. Dover, Z. Najmudin, Hole-boring radiation pressure acceleration as a basis for producing high-energy proton bunches, *Plasma Phys. Control. Fusion* 54 (115001) (2012) 1–7.
- [103] A. Macchi, S. Veghini, F. Pegoraro, Light Sail Acceleration Reexamined, *Phys. Rev. Lett.* 103 (085003) (2009) 1–4.

- [104] F. Pegoraro, S. V. Bulanov, Photon Bubbles and Ion Acceleration in a Plasma Dominated by the Radiation Pressure of an Electromagnetic Pulse, *Phys. Rev. Lett.* 99 (065002) (2007) 1–4.
- [105] A. P. L. Robinson, M. Zepf, S. Kar, R. G. Evans, C. Bellei, Radiation pressure acceleration of thin foils with circularly polarized laser pulses, *New J. Phys.* 10 (013021) (2008) 1–13.
- [106] T. Esirkepov, M. Borghesi, S. V. Bulanov, G. Mourou, T. Tajima, Highly Efficient Relativistic-Ion Generation in the Laser-Piston Regime, *Phys. Rev. Lett.* 92 (17) (2004) 2–5.
- [107] A. Machhi, *A Superintense Laser Plasma Interaction Theory Primer*, Springer, 2013.
- [108] O. Klimo, J. Psikal, J. Limpouch, Monoenergetic ion beams from ultrathin foils irradiated by ultrahigh-contrast circularly polarized laser pulses, *Physical Review Special Topics - Accelerators and Beams* 11 (031301) (2008) 1–14.
- [109] T. Schlegel, N. Naumova, V. T. Tikhonchuk, C. Labaune, I. V. Sokolov, G. Mourou, Relativistic laser piston model : Ponderomotive ion acceleration in dense plasmas using ultraintense laser pulses Relativistic laser piston model : Ponderomotive ion acceleration in dense plasmas using ultraintense laser pulses, *Phys. Plasmas* 16 (083103).
- [110] R. Deny, *Plasma physics: An introductory course*, Cambridge university press, 1993.
- [111] L. E. Hargrove, R. L. Fork, M. A. Pollack, Locking of He-Ne Laser modes induced by synchronous intracavity modulation, *Appl. Phys. Lett.* 5 (1) (1964) 4–5.
- [112] J. Kluge, D. Wiechert, Fluctuations in synchronously mode-locked dye lasers, *Opt. Commun.* 51 (4) (1984) 271–277.
- [113] R. Szipocs, K. Ferencz, Chirped multilayer coatings for broadband dispersion control in femtosecond lasers, *Opt. Lett.* 19 (3) (1994) 201–203.
- [114] I. D. Jung, F. X. Kärtner, N. Matuschek, D. H. Sutter, Z. Shi, V. Scheuer, M. Tilsch, T. Tschudi, Invited paper Semiconductor saturable absorber mirrors supporting sub- 10 - fs pulses, *Appl. Phys. B* 150 (1997) 137–150.
- [115] M. Hentschel, R. Kienberger, C. Spielmann, G. A. Reider, N. Milosevic, T. Brabec, P. Corkum, U. Heinzmann, M. Drescher, F. Krausz, Attosecond metrology, *Nature* 414 (2001) 50913.
- [116] A. Couairon, A. Mysyrowicz, Femtosecond filamentation in transparent media, *Phys. Rep.* 441 (2007) 47–189.
- [117] P. Hilz, T. M. Ostermayr, A. Huebl, V. Bagnoud, B. Borm, M. Bussmann, M. Gallei, J. Gebhard, D. Haffa, J. Hartmann, T. Kluge, F. H. Lindner, P. Neumayr, C. G. Schaefer, U. Schramm, P. G. Thirolf, T. F. Rösch, F. Wagner, B. Zielbauer, J. Schreiber, Isolated proton bunch acceleration by a petawatt laser pulse, *Nat. Commun.* 9 (423) (2018) 1–9.
- [118] T. Brabec, C. Spielmann, P. F. Curley, F. Krausz, Kerr lens mode locking, *Opt. Lett.* 17 (18) (1992) 1292–1294.

- [119] P. Tournois, compensation of group delay time dispersion in laser systems, *Optics Commun.* 140 (1997) 245–249.
- [120] M. E. Fermann, V. Silva, D. A. Smith, Y. Silberberg, A. M. Weinee, Shaping of ultrashort optical pulses by using an integrated acousto-optic tunable filter, *Opt. Lett.* 18 (18) (1993) 1505–1507.
- [121] A. Trisorio, P. M. Paul, F. Ple, C. Ruchert, C. Vicario, C. P. Hauri, Ultrabroadband TW-class Ti : sapphire laser system with adjustable central wavelength , bandwidth and multi-color operation, *Opt. Express* 19 (21) (2011) 264–269.
- [122] R. Li, H. Lu, Y. Geng, Q. Liao, Y. Shou, S. Gao, J. Liu, Y. Zhu, Y. Zhao, J. Chen, X. Yan, Compact laser plasma accelerator at Peking, *Proceedings of IPAC 11* (2016) 2569–2571.
- [123] B. G. Cartwright, E. K. Shirk, P. B. Price, A nuclear-track-recording polymer of unique sensitivity and resolution, *Rev. Sci. Instrum.* 153 (1978) 457–460.
- [124] F. Nürnberg, M. Schollmeier, E. Brambrink, A. Bla, D. C. Carroll, K. Flippo, D. C. Gautier, M. Geißel, K. Harres, B. M. Hegelich, O. Lundh, K. Markey, P. Mckenna, D. Neely, J. Schreiber, M. Roth, Radiochromic film imaging spectroscopy of laser-accelerated proton beams, *Rev. Sci. Instrum.* 80 (2009) 1–13.
- [125] J. Miyahara, K. Takahashi, Y. Amemiya, N. Kamiya, Y. Satow, A new type of X-ray area detector utilizing laser stimulated luminescence, *Nuclear Instruments and Methods in Physics Research A* 246 (1986) 572–578.
- [126] J. S. Green, M. Borghesi, C. M. Brenner, D. C. Carroll, N. P. Dover, P. S. Foster, Scintillator-based ion beam profiler for diagnosing laser-accelerated ion beams, *Proc. SPIE Int. Soc. Opt. Eng.* 8079 (2011) 1–8.
- [127] R. Prasad, D. Doria, S. Ter-avetisyan, P. S. Foster, K. E. Quinn, L. Romagnani, C. M. Brenner, J. S. Green, P. Gallegos, M. J. V. Streeter, D. C. Carroll, O. Tresca, N. Dover, C. A. J. Palmer, J. Schreiber, D. Neely, Z. Najmudin, P. Mckenna, M. Zepf, M. Borghesi, *Nuclear Instruments and Methods in Physics Research A Calibration of Thomson parabola MCP assembly for multi-MeV ion spectroscopy*, *Nucl. Inst. Methods Phys. Res. A* 623 (2) (2010) 712–715.
- [128] S. Reinhardt, Detection of laser-accelerated protons, Ph.D. thesis, Ludwig Maximilians Universität München (2012).
- [129] F. Lindner, Online diagnostics for laser accelerated ions and electrons, Master’s thesis, Ludwig Maximilians Universität München (2015).
- [130] Metrolab Technology SA, Three-axis Magnetometers THM1176 and TFM1186. Users Manual. Version 1.3 (Revision 1.2) (2014).
- [131] M. Noaman-ul haq, T. Sokollik, H. Ahmed, J. Braenzel, L. Ehrentraut, M. Mirzaie, L. Yu, Z.M.Sheng, L.M.Chen, M.Schnrer, J.Zhang, Controlling laser driven proton acceleration using a deformable mirror at a high repetition rate, *Nucl. Inst. Methods Phys. Res. A* 883 (2018) 1–7.

- [132] Y. Gao, Target positioning system for high-repetition-rate laser shooting experiments, Master's thesis, Technische Universität München (2015).
- [133] J. Hartmann, D. Haffa, M. Speicher, J. Bin, P. Hilz, C. Kreuzer, T. Ostermayr, S. Lehrack, J. Schreiber, The spatial contrast challenge for intense laser-plasma experiments, IOP Conf. Series: Journal of Physics: Conf. Series 1079 (2018) 1–6.
- [134] F. H. Lindner, J. H. Bin, F. Englbrecht, D. Ha, P. R. Bolton, Y. Gao, J. Hartmann, P. Hilz, C. Kreuzer, T. M. Ostermayr, T. F. Rösch, M. Speicher, K. Parodi, P. G. Thirolf, J. Schreiber, A novel approach to electron data background treatment in an online wide-angle spectrometer for laser-accelerated ion and electron bunches, Rev. Sci. Instrum. 013301 (1) (2018) 1–5.
- [135] S. Reinhardt, W. Draxinger, J. Schreiber, W. Assmann, A pixel detector system for laser-accelerated ion detection, Journal of Instruments 8 (2013) 03.
- [136] J. H. Bin, W. J. Ma, K. Allinger, H. Y. Wang, D. Kiefer, S. Reinhardt, P. Hilz, K. Khrennikov, S. Karsch, X. Q. Yan, F. Krausz, T. Tajima, D. Habs, On the small divergence of laser-driven ion beams from nanometer thick foils, Phys. Plasmas 073113 (2013) 1–5.
- [137] J. H. Bin, K. Allinger, K. Khrennikov, S. Karsch, P. R. Bolton, J. Schreiber, Dynamics of laser-driven proton acceleration exhibited by measured laser absorptivity and reflectivity, Sci. Rep. 7 (43548) (2017) 1–6.
- [138] F. Verluise, V. Laude, Z. Cheng, C. Spielmann, P. Tournois, Amplitude and phase control of ultrashort pulses by use of an acousto-optic programmable dispersive filter: pulse compression and shaping, Opt. Lett. 25 (8) (2000) 575–577.
- [139] Y. Gao, J. Bin, D. Haffa, C. Kreuzer, J. Hartmann, M. Speicher, F. H. Lindner, T. M. Ostermayr, P. Hilz, T. F. Rösch, S. Lehrack, F. Englbrecht, S. Seufferling, M. Gilljohann, H. Ding, W. Ma, K. Parodi, J. Schreiber, An automated, 0.5 Hz nano-foil target positioning system for intense laser plasma experiments, High Power Laser Sci. Eng. 5 (2017) e12.
- [140] M. Speicher, D. Haffa, M. A. O. Haug, J. Bin, Y. Gao, J. Hartmann, P. Hilz, C. Kreuzer, F. H. Lindner, M. O. Tobias, T. F. Rösch, R. Yang, J. Schreiber, Integrated double-plasma-mirror targets for contrast enhancement in laser ion acceleration, J. Phys.: Conf. Ser. 1079 (012002) (2018) 1–7.
- [141] R. Menzel, Photonics, Springer, 2001.
- [142] K. Shimoda, Introduction to laser physics, Springer, 1991.
- [143] W. H. Carter, Electromagnetic beam fields, J. Mod. Opt. 21 (1974) 871.
- [144] P. F. E. J, Gaussian, HermiteGaussian, and LaguerreGaussian beams: a primer, Preprint physics (2004) 0410021.
- [145] I. Kimel, L. R. Elias, Gaussian, HermiteGaussian, and LaguerreGaussian beams: a primer, IEEE Journal of quantum electronics 29 (9) (1993) 2562.
- [146] C. Maurer, A. Jesacher, S. Fürhapter, S. Bernet, M. Ritsch-Marte, Tailoring of arbitrary optical vector beams, New J. Phys. 9 (2007) 0–20.

- [147] G. S. K.T. Gahagan, Optical vortex trapping of particles, *Opt. Lett.* 21 (11) (1996) 827–829.
- [148] J. Psikal, V. T. Tikhonchuk, J. Limpouch, A. A. Andreev, A. V. Brantov, Ion acceleration by femtosecond laser pulses in small multispecies targets, *Phys. Plasmas* 15 (053102) (2008) 1–8.
- [149] N. R. Heckenberg, R. McDuff, C. P. Smith, A. G. White, Generation of optical phase singularities by computer-generated holograms, *Opt. Lett.* 17 (3) (1992) 221.
- [150] M. C. Nuss, R. L. Morrison, Time-domain images, *Opt. Lett.* 20 (740) (1995) 740–742.
- [151] D. A. Jared, R. Turner, K. M. Johnson, Electrically addressed spatial light modulator that uses a dynamic memory, *Opt. Lett.* 16 (22) (1991) 1785–1787.
- [152] P. C. Sun, Y. T. Mazurenko, W. S. C. Chang, P. K. L. Yu, Y. Fainman, All-optical parallel-to-serial conversion by holographic spatial-to-temporal frequency encoding, *Opt. Lett.* 20 (16) (1991) 1728–1730.
- [153] M. W. Beijersbergen, L. Allen, H. E. L. O. Van Der Veen, J. P. Woerdman, Astigmatic laser mode converters and transfer of orbital angular momentum, *Optics Commun.* 103 (442) (1993) 123–132.
- [154] A. M. Weiner, Femtosecond pulse shaping using spatial light modulators, *Rev. Sci. Instrum.* 71 (5) (2000) 1929–1960.
- [155] M. A. Dugan, J. X. Tull, W. S. Warren, High-resolution acousto-optic shaping of unamplified and amplified femtosecond laser pulses, *J. Opt. Soc. Am. B* 14 (9) (1997) 2348–2358.
- [156] T. Baumert, T. Brixner, V. Seyfried, M. Strehle, G. Gerber, Femtosecond pulse shaping by an evolutionary algorithm with feedback, *Appl. Phys. B: Lasers Opt.* 65 (1997) 779–782.
- [157] M. J. Padgett, L. Allen, Orbital angular momentum exchange in cylindrical-lens mode converters, *J. Opt. B: Quantum Semiclass. Opt.* 4 (2002) S17S19.
- [158] J. F. Nye, M. V. Berry, Dislocations in wave trains, *Proc. R. Soc. Lond. A* 336 (1974) 165.
- [159] C. Tamm, C. O. Weiss, Bistability and optical switching of spatial patterns in a laser, *Journal of the Optical Society of America B* 7 (6) (1990) 1034–1038.
- [160] D. Hennequin, C. Lepers, E. Louvergneaux, D. Dangoisse, P. Glorieux, Spatio-temporal dynamics of a weakly multimode CO<sub>2</sub> laser, *Optics Commun.* 93 (5) (1992) 318–322.
- [161] L. Gil, K. Emilsson, G.-L. Oppo, Dynamics of spiral waves in a spatially inhomogeneous Hopf bifurcation, *Phys. Rev. A* 45 (2) (1992) R567–R570.
- [162] V. Kruglov, Y. Logvin, V. Volkov, The Theory of Spiral Laser Beams in Nonlinear Media, *Phys. Rev. A* 39 (11) (1992) 2277–2291.
- [163] J. D. Jackson, *Classical electrodynamics*, Wiley, 1962.
- [164] L. Allen, M. W. Beijersbergen, R. J. C. Spreeuw, J. P. Woerdman, Orbital angular momentum of light and the transformation of Laguerre-Gaussian laser modes, *Phys. Rev. A* 45 (11) (1992) 8185–8189.

- [165] S. Tao, X. Yuan, J. Lin, P. X., H. Niu, Fractional optical vortex beam induced rotation of particles, *Opt. Express* 13 (20) (2005) 7726–7731.
- [166] E. Santamato, A. Sasso, B. Piccirillo, A. Vella, Optical angular momentum transfer to transparent isotropic particles using laser beam carrying zero average angular momentum, *Opt. Express* 10 (17) (2002) 871–878.
- [167] S. Bernet, A. Jesacher, S. Furhapter, C. Maurer, M. Ritsch-Marte, Quantitative imaging of complex samples by spiral phase contrast microscopy, *Opt. Express* 14 (9) (2006) 3792–3805.
- [168] R. Inoue, N. Kanai, T. Yonehara, Y. Miyamoto, M. Koashi, M. Kozuma, Entanglement of orbital angular momentum states between an ensemble of cold atoms and a photon, *Phys. Rev. A* 74 (053809) (2006) 1–5.
- [169] G.-B. Zhang, M. Chen, C. B. Schroeder, J. Luo, M. Zeng, F.-Y. Li, L.-L. Yu, S.-M. Weng, Y.-Y. Ma, T.-P. Yu, Z.-M. Sheng, E. Esarey, Acceleration and evolution of a hollow electron beam in wakefields driven by a Laguerre-Gaussian laser pulse, *Phys. Plasmas* 23 (033114) (2016) 1–7.
- [170] C. Brabetz, S. Busold, T. Cowan, O. Deppert, D. Jahn, O. Kester, M. Roth, D. Schumacher, V. Bagnoud, Laser-driven ion acceleration with hollow laser beams, *Phys. Plasmas* 22 (013105) (2015) 1–6.
- [171] P. McKenna, D. C. Carroll, R. J. Clarke, R. G. Evans, K. D. Ledingham, F. Lindau, O. Lundh, T. McCanny, D. Neely, A. P. L. Robinson, L. Robson, P. T. Simpson, C.-G. Wahlström, M. Zepf, Lateral Electron Transport in High-Intensity Laser-Irradiated Foils Diagnosed by Ion Emission, *Phys. Rev. Lett.* 98 (145001) (2007) 1–4.
- [172] J. Schreiber, M. Kaluza, F. Gruñer, U. Schramm, B. Hegelich, J. Cobble, M. Geissler, E. Brambrink, J. Fuchs, P. Audebert, D. Habs, K. Witte, Source-size measurements and charge distributions of ions accelerated from thin foils irradiated by high-intensity laser pulses, *Appl. Phys. B* 79 (2004) 1041–1045.
- [173] J. Limpouch, J. Psikal, A. A. Andreev, K. Y. Platonov, S. Kawata, Enhanced laser ion acceleration from mass-limited targets, *Laser and Particle Beams* 26 (2008) 225–234.
- [174] R. Ramis, J. M. ter Vehn, J. Ramirez, MULTI2D a computer code for two-dimensional radiation hydrodynamics, *Computer Physics Communications* 180 (2009) 977994.
- [175] R. Ramis, K. Eidmann, J. ter Vehn, S. Hüller, MULTI-fs A computer code for laserplasma interaction in the femtosecond regime, *Computer Physics Communications* 183 (3) (2012) 637–655.
- [176] R. Ramis, J. M. ter Vehn, MULTI-IFEA one-dimensional computer code for Inertial Fusion Energy (IFE) target simulations, *Computer Physics Communications* 203 (2016) 226–237.
- [177] O. Lundh, F. Lindau, A. Persson, C.-G. Wahlström, P. McKenna, D. Batani, Influence of shock waves on laser-driven proton acceleration, *Phys. Rev. E* 76 (026404) (2007) 1–8.
- [178] D. W. Forslund, J. M. kindle, K. Lee, Theory of hot electron spectra at high laser intensity, *Phys. Rev. Lett.* 39 (5) (1977) 284–288.

- [179] M. L. Zhou, J. H. Bin, D. Haffa, X. Q. Yan, J. Schreiber, The impact of femtosecond pre-pulses on nanometer thin foils for laser-ion acceleration, *Plasma Phys. Control. Fusion* 59 (055020) (2017) 1–5.

# Publications and upcoming publications

1. **Ying Gao**, Pengjie Wang, Bin Liu, Shirui Xu, Yinren Shou, Jianbo Liu, Zhusong Mei, Zhengxuan Cao, Yanying Zhao, Fuyuan Wu, Xueqing Yan, Matt Zepf, Rafael Ramis, Paul R. Bolton, Wenjun Ma and Jörg Schreiber, *Cascaded Laser-driven Proton Acceleration Due to Hot Electron Oscillation in a Transient Micro-plasma cavity*. Ready for submission
2. **Ying Gao**, Jianhui Bin, Daniel Haffa, Jens Hartmann, Thomas F. Rösch, Florian H. Lindner, Martin Speicher, Rong Yang, Tobias M. Ostermayr, Franz S. Englbrecht, Peter Hilz, Christian Kreuzer, Sebastian Lehrack, Johannes Gebhard, Enrico Ridente, Hao Ding, Max Gilljohann, Stefan Karsch, Paul R. Bolton, Katia Parodi and Jörg Schreiber. *On the stability and sensitivity measurement of a 0.5 Hz laser-driven proton source*. Ready for submission
3. **Ying Gao**, Jianhui Bin, Daniel Haffa, Christian Kreuzer, Jens Hartmann, Martin Speicher, Florian H Lindner, Tobias M Ostermayr, Peter Hilz, Thomas F Rösch, Sebastian Lehrack, Franz Englbrecht, Sebastian Seufferling, Max Gilljohann, Hao Ding, Wenjun Ma, Katia Parodi and Jörg Schreiber. *An automated, 0.5 Hz nano-foil target positioning system for intense laser-plasma experiments*. High Power Laser Science and Engineering, 5, e12 (2017)
4. F. H. Lindner, J. H. Bin, F. Englbrecht, D. Haffa, P. R. Bolton, **Y. Gao**, J. Hartmann, P. Hilz, C. Kreuzer, T. M. Ostermayr, T. F. Rösch, M. Speicher, K. Parodi, P. G. Thirolf, and J. Schreiber, *A novel approach to electron data background treatment in an online wide- angle spectrometer for laser-accelerated ion and electron bunches*, Review of Scientific Instruments 89, 013301 (2018)
5. Thomas F. Rösch, Peter Hilz, Jianhui Bin, Franz Englbrecht, **Ying Gao**, Daniel Haffa, Jens Hartmann, Sebastian Herr, Florian H. Lindner, Martin Speicher, Matthias Würfl, Katia Parodi, Jörg Schreiber. *Considerations on employing a PMQ-doublet for narrow and broad proton energy distributions*, Current Directions in Biomedical Engineering 3 (2), 339-342 (2017)
6. FH Lindner, D Haffa, JH Bin, F Englbrecht, **Y Gao**, J Gebhard, J Hartmann, P Hilz, C Kreuzer, S Lehrack, TM Ostermayr, TF Rösch, M Speicher, Matthias Würfl, Katia Parodi, Jörg Schreiber, PG Thirolf *Towards swift ion bunch acceleration by high-power laser pulses at the Centre for Advanced Laser Applications (CALA)*, Nuclear Instruments and Methods in Physics Research Section B: Beam 402, 354-357 (2017)

7. M Speicher, D Haffa, MAO Haug, J Bin, **Y Gao**, J Hartmann, P Hilz, et al., *Integrated double-plasma-mirror targets for contrast enhancement in laser ion acceleration*, Journal of Physics: Conference Series 1079 (1), 012002 (2018)
8. TF Rösch, D Haffa, JH Bin, F Englbrecht, **Y Gao**, V Gisbert, J Gebhard, et al., *Laser-driven ION (LION) acceleration at the centre for advanced laser applications (CALA)*, *The European Conference on Lasers and Electro-Optics*, JSIII P 2, (2017)
9. Haffa D, Yang R, Bin J, Lehrack S, Brack FE, Ding H, Englbrecht FS, **Gao Y**, Gebhard J, Gilljohann M, Götzfried J, Hartmann J, Herr S, Hilz P, et al., *I-BEAT: Ultrasonic method for online measurement of the energy distribution of a single ion bunch*. Sci Rep. 9(1):6714 (2019)
10. C. Jenke, S. Kibler, **Y. Gao**, A. Hollot, T. Neuhann, B. Kirchhof, B. Montag, M. Geiger, J. Neitzel, C. Kutter, M. Richter, *Optimization of a Piezoelectric Micropump Actuator for Medical Application in Glaucoma and Phthisis Therapy*, International Conference and Exhibition on New Actuators and Drive Systems, Bremen, Germany 23-25 June (2014)
11. **Y. Gao**, Y.-P. Zhang and H.-Y. Zhang, *Design of multichannel electronic wave filters with each channel energy and bandwidth adjustable independently* The Euro. Phys. J. Appl. Phys. 59 30402 (2012)
12. Zhang Yu-ping, **Gao Ying** and Zhang Hui-yun, *Independent modulation of defect modes in fractal potential patterned graphene superlattices with multiple defect layers* J. Phys. D: Appl. Phys. 45 055101(2012)
13. Zhang Hui-yun, **Gao Ying**, Zhang Yu-ping, Xu Shi-lin, and Wang Shi-fan, *A tunable electron wave filter based on graphene superlattices with periodic potential patterns* Appl. Phys. Lett. 99, 072108 (2011)
14. Zhang Hui-Yun, **Gao Ying**, Zhang Yu-Ping, Wang Shi-Fan. *Independently tunable multi-channel terahertz filters* Chin. Phys. B, 20(9): 94101 (2011)
15. Hui-Yun Zhang, Yu-Ping Zhang, **Ying Gao**, Yi-Heng Yin, *Independently Tunable Multi-channel Filters Based on Graphene Superlattices with Fractal Potential Patterns*. Chin. Phys. Lett., 29, 12, (2012)
16. Zhang Yu-Ping, Zhang Hong-Yan, Yin Yi-Heng Liu Ling-Yu, Zhang Xiao, **Gao Ying**, Zhang Hui-Yun. *Theory research of negative dynamic conductivity in electrically pumped multiple graphene layer structures with split gates*, Acta Phys. Sin., 61(4): 047803 (2012)
17. H.Y. Zhang, Y. P. Zhang, L.H. Meng, **Y. Gao**, S.F. Wang, *Enlargement of Zero Average Index Gaps Frequency Range of Multiple-Channeled Filters by the Use of Heterostructures Containing Negative-Index Materials* Proceedings of International Conference 2011. Wuhan: IEEE Photonics and Optoelectronics (SOPO)2011.5780677
18. Y. P. Zhang, P. Zhang, H.Y. Zhang, L.H. Meng, **Y. Gao**, L.Y. Zhang, *Theoretical Research of KTP Crystal Used as Both Intracavity Voltage-Increased Electro-Optic Q-Switch and Optical Parametric Generator* Proceedings of International Conference 2011. Wuhan: IEEE Photonics and Optoelectronics (SOPO)2011.5780676

19. Xiao Zhang, **Ying Gao**, Min Li, Bochong Tang, Jiaojiao Wang, Huiyun Zhang, Zhongqing Wei, *Photo-illumination based micro-patterning for assembling of nanomaterials* Conference of China-Japan-Korea Symposium on Analytical Chemistry, 2-23 65 (2012)
20. Bochong Tang, Min Li, Xiao Zhang, **Ying Gao**, and Zhongqing Wei, *Watching alpha-fetal protein captured by its monoclonal antibody* Conference of China- Japan-Korea Symposium on Analytical Chemistry, 2-24 67 (2012)
21. Jiaojiao Wang, Min Li, Bochong Tang, Xiao Zhang, **Ying Gao**, Yuliang Zhao, Zhongbo Hu, Zhongqing Wei, *Controllable assemble of gold nanorods at the nanometer scale*, Conference of China-Japan-Korea Symposium on Analytical Chemistry, 3-27 66 (2012)



# Acknowledgements

At the end of this thesis, I would like to take this opportunity to thank all the mentors, colleagues and relatives who accompanied me through the process.

First of all, I would like to thank **Prof. Jörg Schreiber** for giving me this opportunity to do the master's thesis and doctoral dissertation in this group. I appreciate your patience and encouragement when I am confused. Thank you for your generous support and experimental advice when I proposed a new research project. Thank you for giving me the most study freedom no matter what I was interested in.

I would like to thank **Prof. Wenjun Ma** for your guidance and help during my master's thesis. Thank you for your trust and for not only providing the three-week-beam time in Peking University but also launching your entire group to help me complete the experiment.

I want to thank **Prof. Matthias Kling** for agreeing to be the second supervisor of my PhD thesis.

I want to thank **Prof. Paul Bolton** for your wonderful course and sharing your interesting stories. Thank you whenever I talked to you, you would put down your work at hand to answer my doubts and give suggestions.

I would like to thank **Prof. Katia Parodi** and **PD Dr. Peter Thiolf** for creating a harmonious and enterprising good scientific research environment for our entire group, especially for providing us opportunities to learn and exchange at the annual group meeting and the weekly seminar.

I want to thank to **Prof. Stefan Karsch** and his group for the contribution to the laser facility running. Special thanks to **Hao Ding, Max Gilljohann** et al. who answered me a lot of questions.

I want to thank **Prof. Xueqing Yan** for his support during my experiment in Peking University.

Many thanks go to all my current and former colleagues. I want to thank **Dr. Jianhui Bin**, thank you for introducing me into this field and for a lot of help in technical and theoretical problems. Many thanks to **Dr. Daniel Haffa** for leading the LION experiments in LEX. Thank you, **Thomas Rösch** for helping me translate the abstract into German. Many thanks to **Florian Lindner, Jens Hartmann, Leonard Doyle, Martin Speicher, Rong Yang, Dr. Meilin Zhou, Johannes Gebhard, Dr. Tobias Ostermayr, Dr. Christian Kreuzer, Peter**

**Hilz, Franz Engelbrecht, Sebastian Seuferling, Dr. Matthias Wuerl, Dr. Sebastian Lehrack, Enrico Ridente** et al. for the great time together. I always enjoyed working with you. I hope you enjoy your life and have a successful future!

Special thanks to the experimental collaborators in Peking University. I want to thank **Pengjie Wang**, who gave me great support in experimental design and problem-solving. Many thanks to **Dr. Yinren Shou, Jianbo Liu, Zhusong Mei, Zhengxuan Cao** for your hard work and great support. Without your help, I couldn't finish the experiment anyway. Although we had been working together only for three weeks, I really enjoyed working with you. I wish you a successful career and a prosperous future!

Thank you very much, **Shirui Xu**. You devoted yourself to the MULTI simulation work, started from the very beginning but quickly became an expert in this field. Without your work, I could not complete my doctoral dissertation. And thanks a lot to **Dr. Fuyuan Wu, Prof. Rafael Ramis** and **Dr. Dahui Wang** for your support when we encountered problems of MULTI simulations.

Thank you very much, **Dr. Bin Liu**. From the early days when I designed the Beijing experiment, you helped me with PIC simulations to predict the experimental results. Later, the experiment was finished, then you helped me do countless PIC simulations again to explain the experimental results. After numerous phone discussions, the physical image gradually became clear, and I learned a lot from you. Thank you so much for always taking time to answer my doubts.

Special thanks to my two best friends **Sabrina Krautter** and **Dr. Christoph Jenke** for having a great time together and telling me a lot about German culture.

Many thanks to my parents and my sister, for their love and care for me.

Finally, I would like to thank my wife **Guifang Jiang** very much. Without you, I would not be able to complete my doctoral dissertation anyway! Thank you for the sacrifice you made for me! Also thank my son (**Junpeng Gao**) and daughter (**Xinyi Gao**) for the joy and happiness they bring me!